Development of an Off-Road EV Research Platform

by

Garry Bistyak

A Thesis submitted to the Faculty of Graduate Studies of

The University of Manitoba

in partial fulfilment of the requirements of the degree of

MASTER OF SCIENCE

Department of Electrical and Computer Engineering

University of Manitoba

Winnipeg

Abstract

This thesis describes the design and construction of an off-road battery electric research vehicle. The vehicle is based on a one motor per wheel drivetrain topology. It has a flexible and powerful vehicle control module based on a field programmable gate array (FPGA). Vehicle performance and implementation requirements that form the basis of the vehicle design are presented. A model of the vehicle dynamics is developed, which is then used to simulate the vehicle behavior and validate that important performance specifications are met. The details of design and construction are described and illustrated. Vehicle performance results are presented and discussed. Finally a summary of the completed work is presented.

To family, friends and the pursuit of knowledge

"If you're going through hell, keep going."

— Winston Churchill

Acknowledgements

I would like to thank my advisor, Dr. Shaahin Filizadeh, for his patience and support throughout the pursuit of my degree. I would also like to thank my examining committee for evaluating my work and providing valuable feedback.

This work would not have been possible without the guidance of my advisor and examining committee members. I am also indebted to those members of the support staff of the ECE department who helped me navigate the numerous technical and administrative hurdles which I faced.

I would like to thank RTDS Technologies Inc. for their financial support and Polaris Industries for the donated Polaris Ranger 500 off-road utility vehicle. I am indebted to Sevcon USA Inc. and Price Electronics a division of Price Industries Ltd. Sevcon provided prompt technical support at a critical point in the project. Price Electronics populated the surface mount technology printed circuit board used in the vehicle control module.

My family and friends are owed the deepest debt of gratitude; when I really thought I couldn't, they convinced me I could. Thank you for your support and encouragement.

Contents

List of Figures

List of Tables

List of Acronyms

ADC	analogue to digital converter
BEV	battery electric vehicle
CAN	controller area network
CVT	continuously variable transmission
DARPA	defense advanced research projects agency
DCO	digitally controlled oscillator
EMI	electromagnetic interference
EV	electric vehicle
FNR	forward neutral reverse
FPGA	field programmable gate array
FPU	floating point unit
GPIO	general purpose input output (digital)
GPS	global positioning system
GPSSS	GPS based speed sensor
GSS	ground speed sensor (radar)
I2C	inter-integrated circuit
ICE	internal combustion engine
IMU	inertial measurement unit
I/F	interface
I/O	input or output
LCS	left current sensor

LFMD	left front motor drive
LP	low pass
LRMD	left rear motor drive
LSSW	low side switch
MAC	media access control
MD	motor drive
MFC	Microsoft foundation classes
MISO	master in slave out
MOSI	master out slave in
OLED	organic light emitting diode
ORSIS	off road systems interactive simulator
PCB	printed circuit board
PHY	physical interface
PKT	packet
PMAC	permanent magnet alternating current
PWM	pulse width modulation
RCS	right current sensor
RCVR	receiver
RFMD	right front motor drive
RRMD	right rear motor drive
SCL	I2C clock
SDA	I2C data
SMT	surface mount technology
SPI	serial peripheral interface
SPS	steering position sensor
SSRLY	solid-state relay

SUV	sport utility vehicle
SW	switch
TPS	throttle position sensor
UTV	utility terrain vehicle
VCM	vehicle control module
VDDS	vehicle debug and data logging software
VMCS	vehicle management and control software
WSS	wheel speed sensor

Chapter 1

Introduction

Early motor vehicles were powered by steam engines, electric motors or gasoline engines. From 1880 to 1905, the electric vehicle dominated in North America. Steam powered vehicles also enjoyed a brief period of success in the late 1800's. The acceptance of electric vehicles was hindered by the lack of charging infrastructure, limited range and high cost. Steamers, although capable of fantastic performance, were hindered by the need to frequently take on water and the inconvenience of a prolonged warm-up period. They were also perceived as dirty and dangerous. The gasoline powered vehicle could be driven after a brief starting procedure and made use of the established kerosene distribution network for refueling.

The gasoline powered vehicle continues to dominate the current market (circa 2018) but is losing market share to the electric vehicle. Six countries had electric vehicle market shares above 1.5% with Norway topping out at 29% [1]. One study predicts that electric vehicles will have upwards of 80% market share by 2030 [2].

Off-road vehicle technology is heavily dependent upon technologies developed for on-road vehicles and will out of necessity track on-road technology developments. An electric drivetrain is well suited to off-road applications. The electric drivetrain runs quieter and cooler than an internal combustion engine based drivetrain. This makes the electric off-road vehicle stealthier and safer to operate in dry forest conditions. The electric drivetrain simplifies the implementation of traction management systems [3]. The torque response is much faster and is more directly controlled than with an internal combustion engine vehicle.

To support the development of future off-road vehicles and off-road vehicle drivetrains in particular, an off-road battery electric vehicle (BEV) was designed and built. It has a high performance drivetrain topology combined with comprehensive monitoring instrumentation and a flexible and powerful FPGA based vehicle control module.

1.1 Background: Electric Vehicles

1.1.1 The Early Years

By the 1840's the steam powered locomotive was well established. Around this time, early inventors adapted the steam engine to produce the first motor vehicles. The first commutated DC motor appeared in the early 1830's. The lead-acid battery first appeared around 1860 and was much improved by the late 1880's. Practical electric cars started to appear in numbers in the 1880's, the first electrics had appeared decades earlier but were impractical because of poor battery performance. The gasoline powered motor vehicle appeared last, spurred by the invention of the Otto 4-cycle engine in the late 1870's. By the late 1890's gasoline powered vehicles started to appear in numbers.

Electric vehicle manufacture peaked in 1902, with steamers peaking a decade earlier. By 1902, electric vehicles constituted 62% of motor vehicles in America [4]. Ransom Eli Olds started the mass production of the gasoline powered vehicle in 1901. Henry Ford started production of the Model T in 1908. By 1909 electrics accounted for only 4.4% of vehicles produced [5]. A drastic decline in market share for the electric vehicle in a very short period.

In 1913 with the implementation of the first moving production line, the gasoline powered vehicle began to be produced at a rate and cost of assembly that was not previously possible. By 1920 the gasoline powered motor vehicle had all but replaced the competition. The electric truck was the last vehicle to succumb to the gasoline powered vehicle. It enjoyed a longer period of success from the early 1900's into and past 1920 as a fleet vehicle.

1.1.2 The Decline of the Electric Vehicle

Early motor vehicles of all types were curiosities; barely practical. As the vehicle technologies matured people saw the practicality of the motor vehicle and manufacturing companies appeared. A significant reason for the demise of the electrics and steamers was the lack of entrepreneurship and over attention to the non-practical aspects of the vehicles. The electric and steam vehicles were not designed for the masses. They were not commodity items. Electric and steam powered vehicles were expensive, well-appointed and targeted at wealthy members of society. Electrics also developed the stigma of being a ladies vehicle. It was not uncommon for electric vehicle ads to target women. For a product to be widely adopted it needs to have mass appeal and be affordable.

The motor vehicle began to be associated with the ideas of freedom, adventure and exploration. Henry Ford ran ad campaigns encouraging people to go on camping trips with the knowledge that his gasoline powered vehicle had a large advantage in such an adventure. This idea of traveling long distances and having an adventure appealed to the frontier spirit of the American people. The gasoline powered vehicle could provide high speed and maintain a useful range of travel. Electrics were capable of high speeds but range was severely impacted. This rendered them all but useless for long out of town trips. Steamers could compete with the gasoline powered vehicles on longer trips but were not affordable by the masses.

Around the same time that the motor vehicle appeared some American cities were becoming large enough that transport of goods via horse drawn vehicles was becoming impractical [6]. The cities were literally drowning in manure. The manure was a form of pollution that posed a health hazard to people. A less polluting alternative was needed. The electric truck would fill this need for about two decades. It was a competitive technology that eventually lost out to the economies of scale that the support infrastructure and production of gasoline powered vehicles enjoyed.

The two world wars demonstrated the capability of the gasoline powered vehicle in the long range transport of goods. Shipping of war materiel strained the capacity of the rail systems, local shortages occurred because of a lack of capacity to transport goods. This prompted interest in using motor vehicles for the long range distribution of goods. The gasoline powered motor vehicle was uncontested in this application. The farming community quickly recognized the advantages of motor vehicles. Isolation was largely alleviated by the advent of the motor vehicle, more specifically the gasoline powered motor vehicle. The vehicle technology was also adapted to farming yielding the first tractors. Suddenly something the size of two horses had the power of thirty.

The steamer, electric and gasoline vehicle were major improvements over horse drawn locomotion. The steamer required water and fuel. It also suffered from a prolonged start-up period. A steamer could not be used until a sufficient head of steam was built up. This could take upwards of an hour. The gasoline powered vehicle could be ready to go in a matter of seconds, the electric vehicle practically instantly. The electric vehicle had the complication of battery life-cycle management and a lack of charging stations. The charging situation was further aggravated by the lack of standards for battery connections and voltages. The gasoline vehicle required only fuel that was made readily available through the existing kerosene distribution network [7]. As an additional bonus gasoline was a waste by-product of kerosene production.

A gasoline powered vehicle could be refueled in minutes whereas a battery took hours to charge. Battery swapping could ameliorate this but would require expensive infrastructure investments. The bulky batteries could not compete with gasoline. A notable exception appeared in the form of fleets of electric vehicles serviced by a centralized battery exchange and charging facility. This was practical for fleets of several hundred vehicles; examples include an early electric taxi service and a fleet of electric utility trucks. Both electric vehicles and gasoline powered vehicles were perceived as non-polluting (in comparison to the horse drawn carriage). The gasoline based vehicle more so than the electric; the electric came with the headache of recycling or disposing of spent batteries. The wind carried off the exhaust that the gasoline powered vehicle produced.

Another blow to the success of the electric vehicle was the production of gasoline powered vehicles on a massive scale using the newly invented moving production line. World War I, the Great Depression and World War II were the telling blows to the electric vehicle. The range of the gasoline powered vehicle, especially over rough terrain, could not be matched by the electrics. The logistics of fielding the gasoline powered vehicle were also much simpler. Gasoline vehicle manufacturers captured even greater market share by having sufficient financial resources to offer financing for the purchase of vehicles.

1.1.3 Absence

From about 1945 to 1966 the gasoline powered vehicle enjoyed unhindered success. The market for the gasoline powered motor vehicle grew at an astonishing rate fuelled by the post-war health of the American economy. Following World War II America took on the role of helping rebuild a devastated Europe and Japan. Soldiers returned home and established families growing the American economy even more. The suburbs were born during this period, further fueling the demand for the gasoline powered vehicle. Factories that had produced war materiel could now inexpensively be converted to the production of motor vehicles.

By the mid 1960's smog had become a major problem in large cities [5]. In 1967 the US government enacted emissions standards. The two main exhaust components that contributed to the smog problem were nitrogen oxides and unburned fuel. Air was pumped into the exhaust stream to burn off the unburned fuel (with the aid of a catalytic converter) and exhaust gases were recirculated into the fuel/air mixture to lower combustion temperatures. The lower combustion temperature lowered production of nitrogen oxides. Later, in the 1980's, electronic ignition and fuel injection further reduced the problem of unburned fuel and had the added benefit of improving the fuel efficiency of the vehicle.

Attention to vehicle aerodynamics and rolling resistance (radial tires) led to further improvements in efficiency. Improvements in the vehicle drivetrain also led to improved vehicle efficiency. Front-wheel drive improved the efficiency of power transfer from engine to wheels and reduced the weight of motor vehicles. Increasing the number of available gear ratios in the transmission kept the engine operating efficiently during a higher percentage of the driving cycle.

The 1970's saw renewed hope for the electric vehicle due to concerns of foreign oil supply stability as demonstrated by the Arab Oil embargo in 1973. This problem was addressed by improving domestic supply (offshore oil and the Tar Sands) and by asserting American influence in oil producing regions of the world. The electric vehicle remained on the side-lines.

1.1.4 Return of the Electrics

The Electronic Age has given the masses a familiarity with electronic technology and the technology that powers it; the rechargeable battery and its charger. Rechargeable battery technology has been accepted and today blends into the everyday fabric of life. Today people are more comfortable with electrical/electronic devices than mechanical devices.

The 1980's and 1990's saw a rise in interest in stewardship of the Earth's resources. The push to recycle was born. At the same time scientists started to warn of global warming. California enacted tough legislation that mandated zero emissions vehicles. This led once again to renewed interest in electric vehicles and in the mid 1990's GM introduced the EV-1. The vehicle was well received by the public. It was perhaps the first practical electric vehicle. It had a useable range and excellent performance. It was inexplicably cancelled by GM in 2002. Hybrid electric vehicles also started to appear in the early 2000's. The Toyota Prius being the most successful example. Today (circa 2018) gasoline prices in Canada are at or above $1.20 CDN per litre making electrics competitive [8]. Pollution has again become a problem in the form of greenhouse gases contributing to global warming. Possibly the alignment of all of these effects will tip the balance in favour of the electric vehicle.

1.1.5 The Future

The future motor vehicle will have an electric drivetrain. The gasoline engine only operates efficiently at certain operating load-speed points. To keep the engine operating at an efficient point requires matching engine speed to wheel speed. The more gear ratio selections available in the transmission the more accurately this can be accomplished, the ultimate solution being an infinitely variable transmission. Modern transmissions have become overly complex and expensive. The electric motor and associated drive electronics can be built to be remarkably efficient over a huge load-speed range negating the need for a mechanical transmission. The hundreds of moving parts in an internal combustion engine (ICE) engine equipped vehicle are replaced by a handful of moving parts in the electric vehicle.

More recently electric drive-trains are starting to appear in higher performance off-road vehicles. Until now electric drivetrains were found mostly in electric golf carts and grounds maintenance vehicles. These low performance off-road vehicles helped lay the foundation for adoption of electric drivetrains into the higher performance off-road vehicles. The future high performance off-road vehicle will naturally migrate toward an all electric drivetrain.

An electric drivetrain is well suited to off-road applications. The electric drive-train runs quieter and cooler than an internal combustion engine based drivetrain. This makes the electric off-road vehicle stealthier and safer to operate in dry forest conditions. The electric drivetrain simplifies the implementation of traction management systems [3]. The torque response is much faster and is more directly controlled than with an internal combustion engine vehicle.

1.1.6 Off-road Electrics

One of the earliest examples of a widely adopted off-road electric vehicle is the electric golf cart. It became popular in the 1950's and is still widely used today. The electric golf cart has one electric motor driving the rear wheels through a gear reduction and differential (Figure 1.1a). It is intended for very light duty off-road use (golf course, parks). Typically the single electric motor is rated less than 4 hp and vehicle top-speed is less than 25 km/h.

Utility terrain vehicles (UTV's) first appeared in 1988 with the introduction of the Kawasaki MULE. These vehicles typically find use as grounds and facilities maintenance vehicles. They are still mainly gas and diesel engine powered but versions with electric drivetrains are starting to appear on the market. These vehicles typically have a payload bed at the back and are rated to tow trailers. Additionally these vehicles have a more robust suspension that allows them to perform in rougher off-road conditions (farms, construction sites).

More recently, in the last ten years, electric versions have begun to appear. An example of a current electric UTV is shown in Figure 1.1b. The drivetrain for these vehicles consists of an electric motor driving the rear wheels through a gear reduction and a differential. Typically the single electric motor is rated at under 10 hp and vehicle top-speed is approximately 40 km/h.

(a) Club Car golf cart (© Club Car) (b) Gem UTV (© Polaris)

Figure 1.1: Off-road electrics.

Recreational UTV's first made an appearance in 2004 with the introduction of the Yamaha Rhino. It was a higher performance more off-road capable (trail use) UTV targeted primarily at recreational users. Recreational UTV's are almost exclusively powered by internal combustion engines. This new type of UTV had more power and a more sophisticated longer travel suspension. It could tackle the same trails that were previously accessible only to all terrain vehicles (ATV's) with a much increased payload capability.

Approximately 5 years ago, higher performance electric UTV's have appeared on the market. Some examples are shown in Figure 1.2. The Nikola Zero won't be in production until 2019. These UTV's are all 4 wheel drive. The Ranger EV has a single electric motor with two speed transmission driving the front and rear differentials. It has a 30 hp electric motor and a top speed of approximately 40 km/h. The Prowler EV has an electric motor at the front and rear with gear reduction driving the front and rear differentials. It has a total of 38 hp available from the front and rear motors and a top speed of 40 km/h. The Nikola Zero utilizes a motor per wheel configuration with gear reduction at each wheel. It has a total of 266 hp available from the four motors in the lowest power configuration. The top model advertises 590 hp. Top speed is not advertised but the slowest model Nikola Zero accelerates to 100 km/h in 5.3 s.

(a) Prowler EV UTV (© Textron)

(b) Ranger EV UTV (© Polaris)

(c) Nikola Zero high performance UTV
(© Nikola Motor Company)

Figure 1.2: High performance off-road Electrics.

The Nikola Zero provides the best off-road performance with 14.5 in of ground clearance and 20 in of suspension travel. The Ranger EV has 10 in of ground clearance and 9 in of suspension travel. The Prowler EV has 9 in of ground clearance with suspension travel not specified.

1.2 Motivation

The superiority of the electric drivetrain for off-road vehicles is starting to influence buyers of off-road electric vehicles. Today, circa 2018, newer high performance off-road electric vehicles are starting to appear on the market. In order to facilitate the design of these new high performance vehicles, it is important to provide tools that will aid in the design of off-road electric vehicles and in particular high performance off-road electrics.

The vast majority of research and development is focused on on-road electric vehicle development because of the relatively much larger market for on-road electrics. Developers of off-road electrics will naturally leverage these developments and apply them to off-road electric vehicles. It is important to be able to characterize and quantify the performance of off-road vehicles to allow adaptation of the on-road technologies and to allow development of new off-road specific technologies for the high performance off-road electrics.

Understanding the specific requirements of an off-road electric drivetrain is crucial to developing capable and affordable high performance off-road electrics. Being able to predict and then verify different aspects of the off-road electric vehicle performance is key to enabling the design and verification of drivetrain topologies, traction management systems and basic vehicle performance in different terrain conditions.

Terramechanics is the study of off road traction. In this field much effort has been directed into understanding the performance of agricultural tractors, off-road military vehicles and construction equipment. Some work has been done on extending these results to smaller vehicles such as planetary explorers. None of the work has focused on the terramechanics of high-performance off-road vehicles. All of the mentioned vehicles are studied and modeled at low operating speeds which is representative of the normal operation of these vehicles off-road. There has been some work done in the area of undriven wheels interacting with loose soils at high speed but no studies has been done with driven wheels at high speed on loose soils.

High performance off-road vehicles travel off-road at high speeds. The modeling of soil-tire interaction needs to be extended to account for the higher operating speed and associated high slip rates in loose soil conditions. Wheel slip occurs when the circumferential speed of a wheel is greater than the ground speed of the wheel. The soil-tire interaction model for high performance vehicles can be used to aid in the design of high-performance off-road vehicles and can be used to understand and design off-road traction management systems. The ability to verify the newly developed models and systems is also crucial. New models and systems must be tested in the field before being accepted.

1.3 Thesis

A new model of traction, accounting for the combined affects of high speed and high slip, will aid in the understanding and design of high performance off-road vehicles. A high performance off-road electric vehicle research platform will enable investigations into off-road traction, off-road electric vehicle drivetrains and associated traction management systems. It is important that the platform be well instrumented in order to fully capture the state of the vehicle during off-road experiments.

1.3.1 High Performance Off-road Vehicle Model

- Expand the standard longitudinal vehicle model to account for the effects associated with high levels of slip encountered in many off-road driving situations.

- Develop a semi-emperical relationship for off-road tractive force for loose sand driving conditions expanding the applicability of current models into the regime of high performance off-road driving in loose sand. Accomplish by modeling the thrust generated at high slip and high speed.

- Develop an enhanced relationship for off-road rolling resistance for loose sand driving conditions at high speeds. Accomplish by accounting for the planing action that occurs in loose sand at high speeds analogous to a boat planing on water at high speeds.

- Expand off-road sinkage models to account for the combined affect of high slip and high speed in loose sand conditions. Accomplished by modeling the excavation produced by treaded tires operating in the high slip high speed regime.

1.3.2 An Off-road EV Research Platform

- Design and build a well instrumented electric vehicle (EV) platform suited to investigations of high performance off-road vehicles.

- Build a high performance platform that has a flexible and powerful drivetrain suited to off-road EV investigations.

1.4 Approach

In order to investigate the validity of the thesis statements in section 1.3 and to provide the contributions outlined in section 7.1, work will be completed as follows:

- Develop a practical and easy to implement high performance off-road vehicle model.

- Simulations based on the vehicle model will be used get detailed requirements for the vehicle. The vehicle requirements will be used to design the off-road EV platform drivetrain.

- An existing off-road ICE vehicle will be converted to a BEV. Conversion involves mechanical modifications to the existing chassis as required as well as implementation of an electric drive train and associated control and monitoring systems.

- Vehicle operation and performance will be validated using dynamometer testing and field tests.

Chapter 2

Prior Work

Most of the work into off-road locomotion studies (terramechanics) has been directed at low-speed off-road vehicles such as tractors and military vehicles. This early work is founded on the implicit assumption that off-road vehicles can only traverse difficult off-road terrain at low-speeds. The speed of an agricultural tractor is very low being limited by the available engine power and the very high pulling loads experienced during normal use.

Figure 2.1: Off-road racing. (© Rallystar Motorsport News).

Off-road racing and the current generation of off-road recreational vehicles demonstrate that vehicles can operate at high-speeds in very difficult off-road conditions;

loose soils, rough terrain, steep grades. Current off-road traction models do not include the effects of vehicle speed when determining expressions for tractive force, sinkage and rolling resistance. This is particularly true for loose soil conditions.

It is important to be able to validate new theories and models of high performance off road traction. Therefore, a high-performance off-road vehicle test platform is needed (in particular a BEV based research platform). Almost all of the work done on BEV development has been focused on road vehicles. There has been some development of off-road battery electric vehicles but these are low performance vehicles (essentially converted on road utility vehicles). There is a scarcity of research into off-road traction of high-performance vehicles and in particular BEV vehicles.

2.1 Terramechanics: Tire-terrain Interaction

In order to design and build a high performance off-road EV, the demands of off-road driving must be understood in detail. A model for off-road vehicle locomotion is required. This model must be applicable to high performance driving in adverse soil conditions (loose sand). A thorough understanding of the tire-soil interaction mechanics must form the basis of any work carried out in this area. This understanding is built upon the accumulated knowledge of many researchers that have over the last century examined many aspects of off-road vehicle locomotion.

The earliest works in vehicle locomotion can be traced back to the mid-1800's. These early works studied the cross-country performance of horse drawn carriages. Later, early to mid-1900's, research into the performance of agricultural equipment and off-road military vehicles started to appear. The seminal work in off-road locomotion for self-powered vehicles is Bernstein's paper " Probleme zur Experimentellen Motorpflugmechanik" published in 1913 (as discussed in [9]). This paper examines the wheel-soil mechanics of an early heavy steam engine based tractor.

Near the end of WWII Micklethwait authored a paper titled "Soil Mechanics in Relation to Fighting Vehicles" (as cited in [9]). A more rigorous description of wheel-soil mechanics began to emerge. Micklethwait started to quantify the effect of shear failure under a driven wheel using Coulomb's friction law as a starting point. From 1920 to the late 1940's Russian's expanded on Bernstein's work to enable the modernization and collectivization of Russia's farms [9].

During WWII, the urgency of war lead General Garbari of the Italian Army to independently develop his own descriptions of off-road traction [9].

After WWII, Bekker, originally from Poland, came to Canada to do work in off-road locomotion for the Canadian Army and the National Research Council. During the 1950's, Bekker expanded on the work of Bernstein and Micklethwait and produced a more complete picture of off-road locomotion [9]. Bekker eventually moved to the U.S. to continue his work.

A meeting with Garbari in the late 1950's convinced both Bekker and Garbari that the study of off-road locomotion needed to be more organized. A new field of study was born, terramechanics, the study of off-road vehicle locomotion. The first international conference on terramechanics was held in Italy in 1961. The first publication of the Journal of Terramechanics appeared soon after the conference [9].

It is interesting to note the significant contribution of the Canadian government to terramechanics research. In 1967 at a conference in Quebec City, Canada, Bekker [9, pg.51] gives acknowledgment:

> *...to the farsighted policy of the Canadian Army and to the National Research Council which, at the lowest ebb of international interest in off-road locomotion research, supported for over a decade the fundamental exploration of problems involved. I have never ceased to marvel at these liberal decisions ...*

2.1.1 Early Work – Low Speed Vehicles

In 1956 Bekker published his first book *Theory of Land Locomotion* [10] which presents methods for calculating off-road tractive forces and sinkage. The depth of penetration of wheels into undisturbed ground is the sinkage of a wheel. This early work ignores slippage and predicts only the maximum traction for differing soil and tire configurations. Sinkage is calculated assuming that wheels have zero slip (static sinkage).

Bekker's initial work on off-road traction was rapidly expanded and elaborated in the 1960's. Janosi [11] improved upon Bekker's early work and accounted for slip in the tractive force calculations. Wheel slip is defined as [1],

$$s = \frac{v_r - v_x}{v_r} \tag{2.1}$$

where $v_r = r\omega$ is the wheel speed for a wheel of radius r with angular speed ω and v_x is the tangential ground speed of the wheel. Hegedus [12] incorporated slip into his calculations of wheel sinkage. This is slip sinkage.

Hegedus showed that even a towed undriven wheel will experience slip and that this slip influences the wheel sinkage especially in loose soil conditions. Reece [13] further refined slip sinkage modeling and clearly stated the importance of slip sinkage to traction modeling in sandy terrain. Reece's paper related the sinkage of a tracked vehicle to the height of the lugs on the track and the slip of the track. This is excavation sinkage. The lugs on the track push the soil out from under the track. In 1967, Wong and Reece [14] published an algorithm for calculation of tractive force and sinkage based on Reece's work.

At the end of the 1960's it became possible to start to make some powerful predictions about off-road vehicle performance. There were, however, some caveats: the

[1] Most common definition of slip used in terramechanics.

models did not account for the effect of vehicle speed on traction and sinkage processes (especially important in loose soil conditions) and the models had just begun to account for the impact of slip on wheel sinkage. These early results were applied to low speed vehicles with good success.

Much of the work from 1970 to the 2000's was focused on small scale vehicles; small autonomous vehicles designed for unmanned exploration (Mars Rover is an example). However, some work on full-size vehicles was still done.

In 1976, Gee-Clough published a paper [15] that improved the modeling of slip sinkage. His research improved upon previous models, providing good agreement between predicted and measured values of sinkage and rolling resistance for both clay and sand soils. Results were good for deep sinkage (heavy load) and shallow sinkage (light load). The work however applies only to towed wheels and not driven wheels.

Leonovich *et al* published a paper on trafficability of planetary rovers in 1978 [16]. Leonovich applied Reece's expression for excavation sinkage of a tracked vehicle to a small wheeled vehicle. The expression from Reece's paper was corrected for the typically large area occupied by the lugs of a rubber tire. The calculated values of sinkage vs slip were compared to measured values. There was significant deviation of calculated slip from measured for the more heavily loaded wheels.

Upadhyaya *et al* published a paper in 1997 which describes an improved model for tractive force and rolling resistance [17]. This paper resulted from earlier work which began with a paper on traction prediction from 1989 [18]. The 1989 paper revealed problems with the standard set of soil parameters used in terramechanics.

From 1989 to 1997, Upadhyaya determined a set of parameters which describe different soil types in a statistically significant way and designed devices to measure the new parameters. Previous work was based upon soil parameter sets from civil engineering adapted to terramechanics. This was the first time that statistical analysis was used in a significant way in the field of terramechanics.

By 2000, the field of terramechanics yielded a robust model for off-road vehicle locomotion. Based on a handful of measured soil parameters, it was now possible to model tractive force, rolling resistance and sinkage for off-road vehicles with good accuracy. The models support both wheeled and tracked vehicles. In the case of wheeled vehicles, both driven and undriven wheel performance can now be modeled.

These developments lead to the release of an off-road simulator called Off Road Systems Interactive Simulator (ORSIS) in the late 1990's. This simulator was targeted at simulation of multi-axle military vehicles [19].

As complete as the models are, they are still only applicable to slow moving vehicles operating with, at most, moderate slip. High speed vehicles traveling on sand will plane on the surface of the sand as a boat planes on water. This has a large effect on the handling of the vehicle and the rolling resistance of the vehicle.

At high speeds and high slip, a wheel fitted with a lugged tire will generate significant thrust through the mechanism of mass transport. In extreme cases, this thrust can be many times greater than the vehicle weight, giving a normalized tractive force well above one. The lugged tire equipped wheel will also experience high sinkage at high slip rates due to the excavation of soil from under the wheel.

2.1.2 Recent Work – Accounting for Vehicle Velocity

An important paper was published in 2007 by Coutermarsh [20]. His paper examined the effect that velocity has on rolling resistance in loose sand conditions. There were some earlier attempts at accounting for velocity effects on sinkage and rolling resistance. In 1972, Leland performed extensive testing and modeling of aircraft landing gear behaviour in loose sand conditions [21]. In 1971, Pope measured the effect that speed has on rolling resistance in a clay soil [22]. The work of Leland was not incorporated into the more general developments in terramechanics until Coutermarsh's paper. Pope's work also never generated much interested and was not incorporated into the mainstream research until Coutermarsh's work.

Figure 2.2: Driving on water. (© Icelandic Formula Off-road).

Coutermarsh's experiments were carried out by towing a loaded wheel through loose sand with different loads and at different speeds up to 65 km/h (3 or 4 times faster than typical in the past). His work provided a more accurate expression for rolling resistance at higher vehicle speeds. The relationship that he developed is based on the previously developed expressions for rolling resistance, which he termed low-speed drag, and an impingement drag term that is similar to the expression for air drag on a structure.

The impingement drag term results in a lifting force on the tire because of the angle of attack of the leading face of the tire tread. This lift starts to support the vehicle weight and at high enough speeds (past planing speed) will support the weight on each wheel. This has the affect of reducing wheel sinkage and thus the rolling resistance drops after planing speed is reached.

2.1.3 Recent Work – Sinkage

Lyasko published a paper in 2010 focused on improving predictions of sinkage for wheeled vehicles. His work predicted an almost straight line relationship between slip and sinkage. According to Lyasko's expression sinkage progresses from the initial static sinkage in an almost straight line to a maximum of four times the static sinkage at 100% slip. Static sinkage for a typical off-road vehicle in sand is on the order of 3 to 4 cm. This result can not be true in general. The result implies that a wheeled vehicle would never get stuck in loose soil conditions (with the assumption of a reasonable size tire).

Figure 2.3: Stuck vehicle. (© Icelandic Formula Off-road).

Interestingly, Lyasko refers to Reece's excavation sinkage result and dismisses Reece's sinkage expression as inaccurate and impossible because it predicts infinite sinkage at 100% slip. Lyasko also points out that Reece's prediction often doesn't agree with measurements of wheel sinkage performed in experiments.

In 2014, Yamakawa *et al* published a paper that models tire behavior in loose sand. Their experiments produced sinkage vs slip results that indicate a straight line relationship between slip and sinkage. In fact the authors fit straight lines to the data to model the sinkage behavior. The fitted lines start from the balanced sinkage at zero slip and end at some finite value for 100% slip. Balanced sinkage is the level of sinkage reached once dynamic sinkage has reached it's final value. The vehicle is placed on soil and sinks to the static sinkage level after rolling for a short distance, through the mechanism of dynamic sinkage, the vehicle will settle to the deeper balanced sinkage point. Through the mechanism of excavation sinkage the vehicle will settle deeper into the soil at higher and higher slip rates.

As with Lyasko's results this method under predicts sinkage at high slip rates. The maximum predicted sinkage for a 20 cm diameter wheel is approximately 6 cm when in fact in practise the wheels of a vehicle at high enough slip will sink until the vehicle chassis rests on the ground (Figure 2.3). Yamakawa's work does clearly illustrate the dynamic nature of sinkage. There is a clear settling time associated with the measured sinkage and in fact the sinkage follows an exponential curve to a final value.

2.1.4 Tractive Force from Thrust

A significant source of tractive force on loose soils can come from thrust due to mass transport. Thrust generation becomes significant at high speeds and a high slip. It is also highly dependent on the tire tread. A tire with large lugs and lots of void space

Figure 2.4: Vehicle propelled by thrust. Drag racing on loose sand (from Wikimedia Commons).

in the tread pattern will contribute to high thrust levels. The thrust comes from the impulse imparted to the vehicle by the sand ejected to the rear of the vehicle. The same principle propels a rocket forward but here chemical energy is used to eject exhaust at a high speed to the rear of the rocket.

None of the terramechanics literature mentions this effect because low power to weight ratio vehicles are modeled. These vehicles typically operate at low speeds and at most moderate slip, never at high speeds and high slip.

2.2 Off-road EV Research Platform

Much work has been done on the development of autonomous off-road vehicles motivated by DARPA competitions in the USA (figure 2.5). The primary objective in the design of these vehicles was not high performance and the vast majority of these vehi-

Figure 2.5: H1ghlander DARPA Challenge vehicle (© Carnegie Mellon University).

cles were not electric vehicles. In fact most of the vehicles were based on existing mild off-road vehicles such as sport utility vehicles (SUV's). In addition the instrumentation was chosen to aid navigation not to enable off-road traction and performance studies [23].

Some companies have produced development platforms for electric vehicles for example figure 2.6. This platform is based on a one motor drivetrain topology. A single electric motor drives the front wheels through a differential. This configuration is not

Figure 2.6: Tabby EVO development platform (© Open Motors).

well suited to off-road use. The peak vehicle power is 40 hp providing mid-level off-road performance. The suspension is primarily designed for on-road use and is suited only to light duty off-road use. As well, the vehicle is lacking the instrumentation needed to carry out off-road performance and traction studies.

A multi-motor electric vehicle development platform was described by de Castro in [24]. The development platform is based on a MicroCar Virgo chassis. Propulsion

(a) Converted MicroCar Virgo

(b) Motor per front wheel

Figure 2.7: Multi-motor EV (de Castro).

is provided by two induction motors each rated at 3 hp driving each of the front wheels of the vehicle (figure 2.7b). Top-speed is approximately 30 km/h reached in approximately 20 s. Power is provided by four 12V lead acid batteries (105 Ah). Control inputs are throttle position and steering position. A uniform torque control strategy was used for preliminary testing of the vehicle; providing equal torque to both front motors.

This EV development platform has a flexible and powerful vehicle controller based on a Xilinx FPGA development board. The various interfaces to sensors, analog to digital converters (ADC's) and the DC to AC converters are implemented in Verilog code on the FPGA development board. A serial port is also implemented to allow data logging with a PC. The motor controller algorithms are implemented in a mix of Verilog code and embedded code running on an instantiated picoBlaze soft processor.

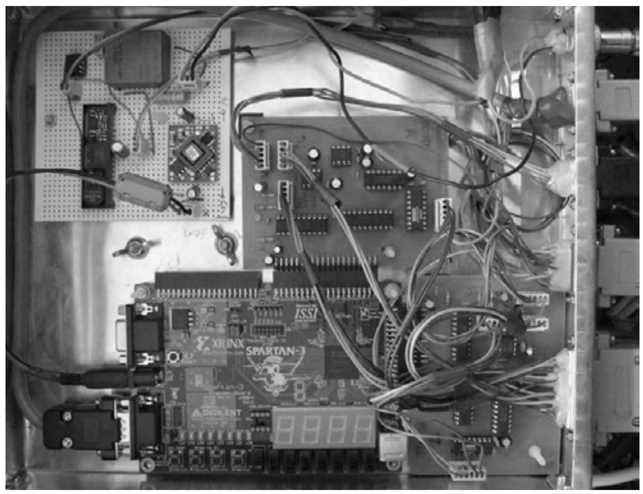

Figure 2.8: Vehicle controller (de Castro).

The total power available for propulsion in this vehicle is only 6 hp. It is a low performance vehicle based on an existing on road vehicle chassis definitely not suited to investigations into off-road electric vehicles. This development platform does have some appealing features. The motor per front wheel drive train architecture shows that a differential is not required even for an on road vehicle operating in a high traction environment. The FPGA development board provides ample processing power and the required interface logic needed to implement the vehicle controller.

Chapter 3

High Performance Off-road Vehicle Model

The design and construction of the off-road EV research platform followed a combination of traditional design and V-Cycle model based design [25] and [26]. Traditional design moves from specification to system design and then subsystem design. Subsystems are tested and integrated and then the system as a whole is tested. V-Cycle design brings simulation and modeling into the design flow at the beginning and takes advantage of rapid prototyping methods.

Because simulation and modelling are used early in the V-Cycle design process, a mathematical model for vehicle motion is developed. The model captures only the essential aspects of the vehicle dynamics. The model is used to determine the power and torque requirements for off-road driving in loose sand conditions and hardpack conditions. A longitudinal model is developed based upon models found in [27, p.42], [28, p.96], [29, ch.2] and [30]. This model allows vehicle performance to be simulated for different operating conditions. The model is used to validate design decisions that pertain to the vehicle drivetrain early in the design process. Battery sizing and electric motor selection is made based on simulation results.

3.1 Longitudinal Motion

The standard longitudinal model is augmented by accounting for wheel slip. In on-road modeling slip can be neglected because it is very small (typically less than 5% [31]). Off-road driving typically involves driving over terrain which provides very little traction, i.e. wheel slippage is high and cannot be ignored. This is especially true for high performance vehicles which can operate at high speeds and very high slip.

Consider the vehicle shown in Figure 3.1. The tractive force F_T is acted against by the rolling resistance of the tires F_r, the aerodynamic drag of the vehicle body F_d (for a wind speed of zero), and gravity F_g (for positive slopes). The net force, F_a, which

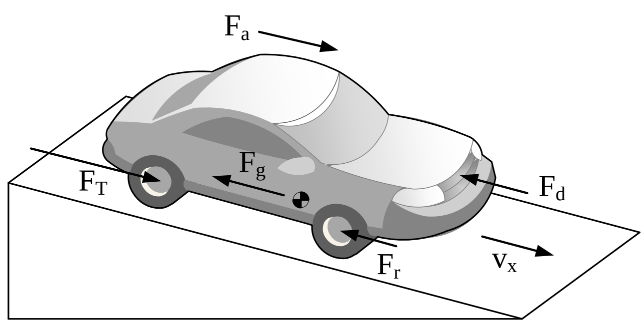

Figure 3.1: Vehicle longitudinal model.

accelerates the vehicle is given by,

$$F_a(v_x, s) = F_T(v_x, s) - (F_d(v_x) + F_r(v_x) + F_g) \tag{3.1}$$

where v_x is the vehicle speed and s is the wheel slip. Therefore, the equation of motion for the vehicle is,

$$M\frac{dv_x}{dt} = F_T(v_x, s) - (F_d(v_x) + F_r(v_x) + F_g)\,. \tag{3.2}$$

The aerodynamic drag (assuming no wind) is given by,

$$F_d(v_x) = \frac{\rho_{air} A_f C_v {v_x}^2}{2} \tag{3.3}$$

where ρ is the density of air, A_f is the vehicle frontal area and C_v is the shape factor. The force resisting motion uphill is given by,

$$F_g = Mg\frac{\beta}{\sqrt{(1+\beta^2)}} \tag{3.4}$$

where M is the vehicle mass and g is the gravitational constant for earth. The road slope β is defined by,

$$\beta = \frac{\text{road rise}}{\text{run}}. \tag{3.5}$$

Expressions need to be found for F_T and F_r in order to complete the description of the vehicle dynamics given by Eq. (3.1).

Table 3.1: Vehicle parameters.

Parameter	Value	Units	Description
M	740	(kg)	vehicle mass
A_f	3.0	(m^2)	vehicle frontal area
C_v	0.7		vehicle drag coefficient
r	29.0	(cm)	vehicle tire radius
n	5		gear ratio
g	9.81	(m/s^2)	gravitational constant (Earth)
ρ_{air}	1.20	(kg/m^3)	air density at STP
ρ	1400	(kg/m^3)	sand density
h	2.0	(cm)	tire effective lug height
w	10.0	(cm)	tire tread width
p	12	(psi)	tire pressure
z_{settle}	2.0	(cm)	static plus dynamic sinkage
z_{max}	10.0	(cm)	maximum sinkage allowed

3.2 Tractive Force

In general the tractive force acts on a vehicle to both propel it forward and to bring it to a stop. The tire terrain interaction is quite different for the case of propulsion or braking. The expression for tractive force developed here represents only the force of propulsion. In the case of a propulsion, the tractive force $F_T(v_x, v_r)$ for loose sand conditions is composed of a thrust component and a friction component.

A slipping wheel will generate thrust in loose soil (eg. sand) because of mass transport, similar to a rocket engine. Recall that the vehicle has a mass M and has a

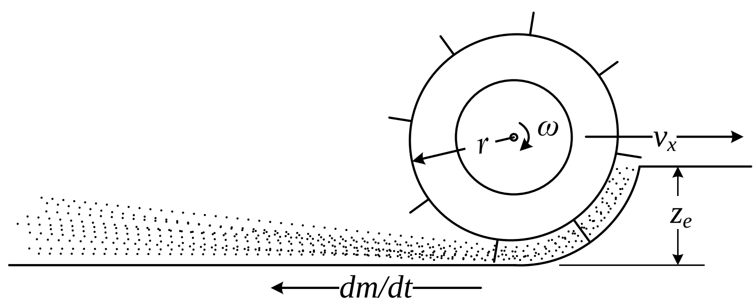

Figure 3.2: Lugged tire moving through loose sand.

velocity v_x. The tire is rotating with speed ω and has a radius of r not including the lug height h. The lug height is assumed to be small compared to the tire radius. The thrust generated by the tire can be calculated by applying conservation of momentum to the system [32, Eq.(9-17)]. The undisturbed soil will act as the stationary reference frame. Forces are considered to act purely in the lateral direction (along x direction). It is assumed that the sand is thrown straight back when in reality there is a spread in the velocity (angle) of the thrown sand grains. This assumption will result in an over estimate of the generated thrust canceling to some extent the effect of assuming that lug height is small compared to the tire radius. As well, the transported sand is assumed to be confined to the channel formed between the tire carcass and the undisturbed sand.

Conservation of momentum means that any momentum imparted to the sand must be counteracted by an equal and opposite momentum imparted to the vehicle. This gives,

$$dm(v_r - v_x) = M dv_x \tag{3.6}$$

where dm is the infinitesimal amount of sand thrown back in time dt and dv_x is the infinitesimal change in velocity of the vehicle which happens in time dt. This gives,

$$M\frac{dv_x}{dt} = (v_r - v_x)\frac{dm}{dt}. \tag{3.7}$$

The left hand side of Eq.(3.7) is simply the thrust acting on the vehicle to accelerate it, that is,

$$F_{thrust} = (v_r - v_x)\frac{dm}{dt}. \tag{3.8}$$

Assuming that lug height is small compared to tire radius, the mass transported by tire spin (Figure 3.2) is given by,

$$dm = \rho w h\, v_r dt \tag{3.9}$$

where ρ is the density of sand and w is the tire width. The thrust can then be written as,

$$F_{thrust} = \rho w h\,(v_r - v_x)\, v_r. \tag{3.10}$$

Let slip be defined as,

$$s = \frac{v_r - v_x}{v_x}, \tag{3.11}$$

where $v_r = r\omega$ is the wheel speed for a wheel of radius r with angular speed ω. This expression provides a better wheel spin metric for high slip values. This gives,

$$v_r = v_x\,(s + 1)\,. \tag{3.12}$$

Therefore, Eq. (3.10) can be rewritten as,

$$F_{thrust} = \rho w h \, (1 + s) \, s \, v_x^2 \tag{3.13}$$

where in almost all practical applications h is actually the effective lug height because tire tread almost never consists of a simple array of paddles. The effective lug height must be determined by experiment.

The friction component is based on traction data from Lyasko in [33, Figures 1 and 2]. Lyasko provides two plots of average tire performance in sand; pull coefficient vs slip and rolling resistance vs slip. The pull coefficient vs slip data is from Zoz [34]. Lyasko calculates rolling resistance in [33]. The sum of the pull coefficient and the rolling resistance is the friction component of the tractive force. Eq. (3.14) provides good agreement with the calculated values and also allows extrapolation to higher slip values. Figure 3.3 is a plot of Eq. 3.14.

$$F_{fric}^{S} = 0.55 Mg \left(1 - \frac{1}{1 + 2s}\right) \tag{3.14}$$

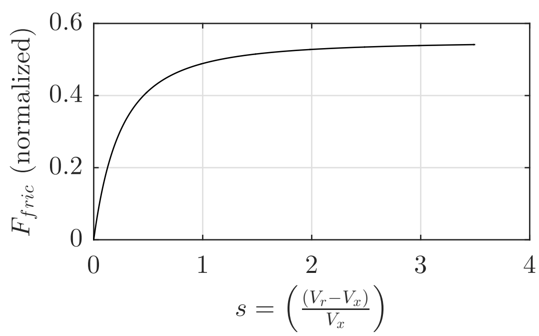

Figure 3.3: Off road friction component of tractive force.

The total tractive force for loose sand is given by,

$$F_T^S(v_x, s) = F_{thrust}(v_x, s) + F_{fric}^S(s). \tag{3.15}$$

The tractive force for hardpack conditions is based upon on-road traction vs slip taken from Cabrera [35]. It has been assumed that a well designed off-road tire will exhibit about the same grip on hardpack as an average street tire on an average paved road. In the hardpack case there is no thrust effect. Eq. 3.16 provides good agreement with the data from Cabrera. Figure 3.4 is a plot of Eq. 3.16.

$$F_T^H(s) = 0.85Mg\left(1 - \frac{1}{(1+5s)^5}\right) \tag{3.16}$$

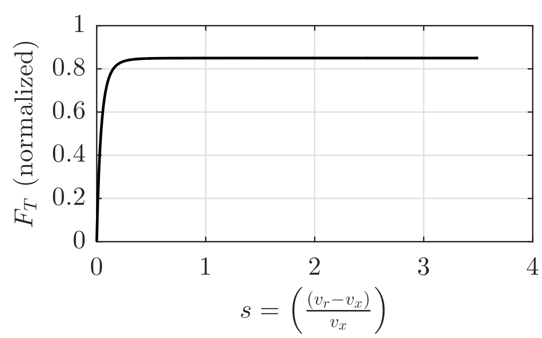

Figure 3.4: Hardpack tractive force.

3.3 Resistance

The rolling resistance $F_r^S(v_x)$ for loose sand conditions is based upon a graph from [36, p.113]. A look up table is constructed from the graph data. The table values are modified to include the effect of wheel planing. Additionally, the table values are compensated for the light loading of high performance off-road vehicle wheels by

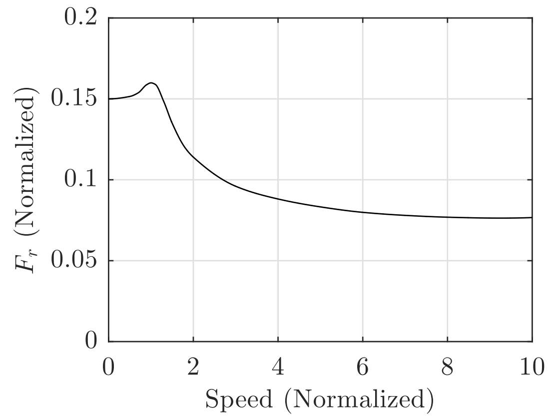

Figure 3.5: Loose sand rolling resistance.

lowering the peak rolling resistance. A portion of the data in the look up table is plotted in (Figure 3.5).

At high enough speeds a wheel will plane on sand in the same way that a boat will plane on water as explained by Coutermarsh in [20]. Planing speed is given by,

$$V_p = 1.32p \tag{3.17}$$

where V_p is the planing speed in km/h and p is the tire pressure in psi [20, Eq.(2)]. Impingement drag [20] causes rolling resistance to build until a certain speed (planing speed) is reached at which point the lift effect begins to dominate causing the rolling resistance to drop off to a much smaller value at high speeds. The results in Coutermarsh's paper are for towed wheels. It is surmised that the high slip of a driven wheel will act to reduce the peak in rolling resistance that occurs just before planing.

The hardpack rolling resistance F_r^H was assumed to be constant with a value of 0.05 (normalized to vehicle weight). The value is taken from [37, Figure 11].

3.4 Sinkage

The wheel of a vehicle sinks into the soil through a variety of mechanisms. This discussion will focus on the mechanisms relevant to loose sandy soil. Since of only propulsive forces are included in the vehicle model, only three mechanisms sinkage mechanisms will be examined; static sinkage, dynamic sinkage and excavation sinkage.

Static sinkage occurs as the tire of the vehicle first begins to sink. The grains of sand are initially squeezed out from under the sand until the pressure builds to a certain point and the sand is compacted enough to support the vehicle weight.

At a certain point the sinkage is substantial enough that the undriven wheel starts to slip. The slippage, probably in combination with tire vibrations, disturbs the compaction of the sand and allows further sinkage. This increases the contact patch allowing the sinkage to settle to a new value. This has been called slip sinkage in the literature but will be referred to as dynamic sinkage in this thesis.

Excavation sinkage only occurs for a driven wheel which has a lugged tire. As slip occurs the lugs of the tire will actually excavate soil from underneath the wheel leading to very substantial sinkage at high slip rates.

Therefore, total sinkage then may be written as,

$$z(t) = z_{ex}(t) + z_{stat}(t) + z_{dyn}(t). \tag{3.18}$$

Excavation sinkage is the dominant effect for high performance off-road vehicles. They are typically equipped with large aggressive tires that have high flotation on loose soils. Therefore, the static plus dynamic sinkage will be modeled by a single constant (z_{settle}) value that is unique to the particular vehicle and tire combination. The total sinkage is then,

$$z(t) = z_{ex}(t) + z_{settle}. \tag{3.19}$$

An expression for the excavation sinkage of a driven wheel is required to allow calculation of $z(t)$. This expression can be found by considering Figure 2.4. Sand is excavated underneath the tire by the action of the tire lugs as the tire slips. The excavation rate under the vehicle tire is given by Eq. 3.9. At the same time that sand is removed from under the tire, new sand is appearing at the leading edge of the tire as it moves forward. The fill rate, dictated by the geometry in Figure 2.4, is given by,

$$dm_x = \rho w z_e\, v_x dt. \tag{3.20}$$

The net excavation rate is the difference between the excavation rate and the fill rate, as follows,

$$\frac{dm_z}{dt} = \rho w \left(h v_r - z_e v_x\right). \tag{3.21}$$

In the steady-state ($dm_z/dt = 0$),

$$z_e^{ss} = h\frac{v_r}{v_x}, \tag{3.22}$$

or in terms of s and v_x,

$$z_e^{ss} = (1+s)h. \tag{3.23}$$

Eq. (3.23) is equivalent to the expression that appears in Reece's paper [13].

From Figure 3.6 for a tire of width w and sand of density ρ, the incremental mass of the displaced sand may be written as,

$$dm_z = \rho w l\, dz_e, \tag{3.24}$$

or

$$dm_z = 2\rho w\sqrt{2rz_e - z_e^2}\, dz_e. \tag{3.25}$$

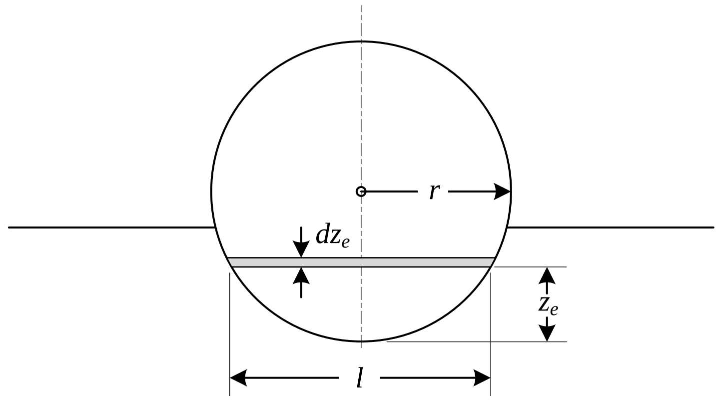

Figure 3.6: Displaced sand.

Substituting Eq. (3.25) into Eq. (3.21) and simplifying, results in,

$$\frac{dz_e(t)}{dt} = \frac{(hv_r(t) - z_e(t)v_x(t))}{2\sqrt{2rz_e(t) - z_e^2(t)}} \tag{3.26}$$

the equation for excavation sinkage of a wheeled vehicle or by substituting Eq. (3.12),

$$\frac{dz_e(t)}{dt} = \frac{(h(1 + s(t)) - z_e(t))\ v_x(t)}{2\sqrt{2rz_e(t) - z_e^2(t)}}. \tag{3.27}$$

This expression may be integrated to give the excavation sinkage vs time.

Typically sinkage is measured from the body of the tire and not the tips of the lugs. The sinkage relative to the body is then,

$$z_{ex}(t) = z_e(t) - h. \tag{3.28}$$

Therefore, the complete expression for sinkage is,

$$z(t) = z_e(t) - h + z_{settle}. \tag{3.29}$$

3.5 Application of Model

3.5.1 Steady-state Power

The total power required to propel the vehicle as a function of ground speed and wheel speed is given by,

$$P_{req}(v_x) = v_r F_T^{req}(v_x), \tag{3.30}$$

or

$$P_{req}(v_x) = v_x(s_{req} + 1)F_T^{req}(v_x), \tag{3.31}$$

from Eq. (3.12), where s_{req} is the slip required to produce the required tractive force at a given v_x.

To find the steady-state power requirements of the vehicle, the acceleration may be set to zero in Eq. (3.1), giving the following expression,

$$F_T^{req}(v_x) = F_d(v_x) + F_r(v_x) + F_g. \tag{3.32}$$

Substituting Eq. (3.32) into Eq. (3.31) gives,

$$P_{req}(v_x) = v_x(s_{req}(v_x) + 1)(F_d(v_x) + F_r(v_x) + F_g), \tag{3.33}$$

which is the total power required to move at a constant speed v_x, with,

$$s_{req}(v_x) = s(F_T^{req}(v_x), v_x). \tag{3.34}$$

where $s(F_T^{req}(v_x), v_x)$ returns the slip required to produce the given tactive force at the given ground speed; essentially the inverse of F_T. Knowing $s(v_x)$ also allows results to be presented against ground speed or motor speed.

3.5.2 Steady-state Torque

The total torque required at the vehicle wheels is given by,

$$T_{wheel}^{req} = rF_T^{req}, \tag{3.35}$$

therefore the motor torque is,

$$T_m^{req}(v_x) = \frac{rF_T^{req}(v_x)}{n}, \tag{3.36}$$

where n is the transmission gear ratio. The motor speed is given by,

$$\omega(v_x) = \frac{nv_x(s_{req}(v_x) + 1)}{r} \tag{3.37}$$

3.5.3 Maximum Acceleration and Top Speed

The tractive force at the vehicle wheels is assumed to be equal to the motor force available at the wheels. Therefore tractive force available at the wheels is given by,

$$F_T(v_x, s) = \frac{nT_m(\omega)}{r}. \tag{3.38}$$

The torque is commanded by the vehicle driver via the throttle and is restricted as follows,

$$0 \leqslant T_m \leqslant T_m^{max}, \tag{3.39}$$

where T_m^{max} is the maximum motor torque available at a given motor speed. Substituting Eq. (3.38) and rearranging gives,

$$0 \leqslant F_T \leqslant \frac{nT_m^{max}(\omega)}{r}. \tag{3.40}$$

Maximum acceleration occurs when maximum tractive force is available. Maximum tractive force corresponds to the upper limit, so that,

$$F_T = \frac{nT_m^{max}(\omega)}{r}. \tag{3.41}$$

This can be expanded to,

$$F_T = \frac{n}{r}\, T_m^{max}\left(\frac{nv_x}{r}\left(s\left(v_x, F_T\right) + 1\right)\right). \tag{3.42}$$

The values of F_T that make Eq. (3.42) true correspond to the maximum tractive force that is available at a given vehicle speed v_x. These values can be found numerically, and will be represented by,

$$F_T^{max}(v_x). \tag{3.43}$$

Substituting Eq. (3.43) into Eq. (3.2) gives,

$$\frac{dv_x}{dt} = \frac{F_T^{max}(v_x)}{M} - \frac{(F_d(v_x) + F_r(v_x) + F_g)}{M} \tag{3.44}$$

Top speed for any vehicle occurs when the tractive force is just equal to the forces resisting motion of the vehicle. Setting acceleration to zero in Eq. (3.44) gives,

$$0 = F_T^{max}(v_x) - \left(F_d(v_x) + F_r(v_x) + F_g\right). \tag{3.45}$$

The maximum speed is the value of v_x that makes Eq. (3.45) true, call it v_x^{max}.

3.5.4 Sinkage Control

The simplest method of controlling the sinkage is to control the steady-state sinkage since it depends only upon slip (Eq. (3.23)). This results in a conservative control scheme because slip is possibly reduced even before sinkage has become excessive. The dynamics are ignored. From Eq. (3.29), the steady-state sinkage can be given as,

$$z_{ss}(t) = z_e^{ss}(t) - h + z_{settle}, \tag{3.46}$$

substituting Eq. (3.23) gives,

$$z_{ss}(t) = hs + z_{settle}. \tag{3.47}$$

The sinkage must remain below a maximum allowed sinkage value z_{max}. That is,

$$z_{ss}(t) \leqslant z_{max}, \tag{3.48}$$

which gives after substitution and simplification,

$$s \leqslant \frac{z_{max} - z_{settle}}{h} = s_{control}. \tag{3.49}$$

Eq. (3.49) affects results in Section 3.5.3. Eq. (3.44) becomes,

$$\frac{dv_x}{dt} = \begin{cases} \dfrac{F_T^{max}(v_x)}{M} - \dfrac{(F_d(v_x) + F_r(v_x) + F_g)}{M}, & s \leqslant s_{control} \\[2ex] \dfrac{F_T(v_x, s_{control})}{M} - \dfrac{(F_d(v_x) + F_r(v_x) + F_g)}{M}, & s > s_{control} \end{cases} \tag{3.50}$$

Chapter 4

Off-road EV Research Platform– System Design and Specifications

4.1 Instrumentation

The vehicle needs to be well instrumented to facilitate the gathering of experimental data, such as wheel speeds, wheel torque, ground speed, vehicle attitude, steering position, vehicle location, vehicle accelerations and wheel torque. A flexible vehicle research platform should provide a picture of the vehicle state that is as complete as possible and in realtime. This will ensure that research into vehicle performance and new control algorithms is not restricted. It is also important that there is some level of redundancy in the instrumentation systems. The redundancy makes the vehicle more robust and also allows data fusion to be used to improve measurement accuracy and precision [38].

4.1.1 Speed

Vehicle speed and wheel speeds must be measured in order to calculate wheel slip. Wheel slip is an important quantity that is essential to the operation of most modern traction management systems [39]. Radar and global positioning system (GPS) based speed sensors are used to measure vehicle ground speed [40]. The radar based sensor measures the doppler shift of a microwave signal reflected from the moving ground. The GPS speed sensor is a specialized unit that provides speed updates several times per second in contrast to the normal one second updates from a position GPS. An inertial measurement unit (IMU) is also part of the sensor suite. The IMU also allows calculation of the vehicle ground speed [41]. The motor encoders are used to determine wheel speeds. The encoders determine the rotor position of the motors several times per second.

4.1.2 Position and Orientation

A GPS receiver is included to allow recording of vehicle position. Vehicle position in conjunction with a terrain map can be used augment traction management schemes with terrain information. The IMU can be used to implement an inertial navigation system that works in conjunction with the GPS to provide complete vehicle orientation and position information [41][42]. The GPS would be used to correct the inherent drift of the IMU and the IMU would provide position information during poor GPS satellite reception or coverage.

Vehicle orientation and rates of change of orientation can provide information about the ground slope and surface undulations of the terrain being traversed by the vehicle. A steering position sensor is also included in the vehicle instrumentation. Steering position can be used to proportion torque to the left and right side motors to enhance steering and vehicle controllability [3][43].

4.1.3 Torque

In-situ torque measurement can be used to improve and monitor electric vehicle performance [44]. Realtime torque measurement can provide feedback to a traction management system improving the performance of the system. The torque measurements are critical to a closed-loop torque management system such as torque assisted steering. Axle mounted wireless torque transducers will be used to measure wheel torque at each wheel position.

4.1.4 Monitoring and Control

The data generated by the various sensors on the vehicle will be processed by the vehicle control module (VCM). The VCM will be based on an FPGA development board (Terasic Cyclone V GX development board). This development board provides a very flexible and powerful processing platform for development of vehicle control and monitoring hardware and software.

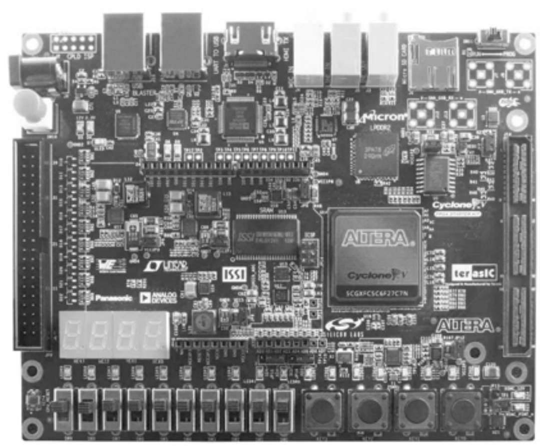

Figure 4.1: FPGA Board.

All control and monitoring of vehicle systems will be performed by the FPGA development board. It has numerous general purpose digital I/O's and 8 analog input channels. The digital and analog channels will be connected to various vehicle instruments and transducers via interface electronics. The interface electronics provides the required signal conditioning for the various different instrument and transducer signal interfaces.

The control and monitoring functions required in a vehicle are more typically handled by an embedded processor based platform. The disadvantage of this approach is the lack of flexibility. The VCM capabilities are fixed when the embedded platform is chosen. The embedded platform will typically have a single CPU with a standard set of interface peripherals. If more processing power is required later or an interface type is not supported then the platform will need to be changed or a second platform will have to be added. With the FPGA based solution another processor or peripheral interface can be added via a software change (to the FPGA code) with no changes to the physical hardware.

4.2 Drivetrain

4.2.1 Topology

Figure 4.2 shows three possible drivetrain topologies for the proposed vehicle. The one motor topology shown in Figure 4.2a provides the simplest design from the electrical systems perspective; there is only one motor to power and to monitor and control. This topology, however, does not readily lend itself to investigating vehicle traction systems. Control and monitoring at each wheel is not available.

The topology shown in Figure 4.2b uses a front and rear motor. This topology still requires front and rear differentials which makes torque vectoring difficult and inefficient (relies on individual brake actuation). Additionally, torque control via a smart differential would have a slower dynamic response than direct torque control (via motor current). The final topology shown in Figure 4.2c allows direct torque control (and monitoring) on a per wheel basis. This will allow skid steering and torque assisted steering of the vehicle as shown in [43]. The one motor per wheel topology is the best choice for a BEV research platform even though it comes with

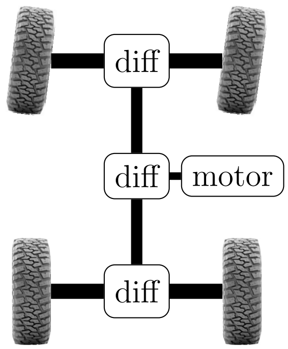

(a) One Motor

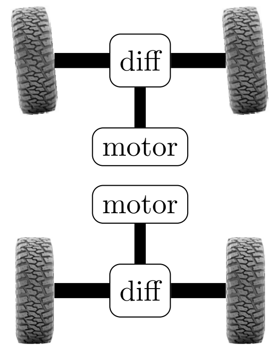

(b) Front and Rear Motors

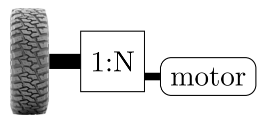

(c) One Motor per Wheel

Figure 4.2: Drivetrain Topologies.

added implementation complexity (much of the electrical system will be replicated four times). The one motor per wheel topology provides for superior traction management. The torque at each wheel may be controlled directly. This topology also eliminates the front and rear differentials offsetting the additional battery weight.

4.2.2 Components

In order to minimize the amount of time spent on mechanical design and implementation the vehicle was based upon an existing utility vehicle chassis. Polaris Industries donated a 2009 Polaris Ranger 500 EFI for the project (Figure 4.3). The Ranger 500 EFI has an ICE with a displacement of 0.5 litres producing about 32 hp. It is a four wheel drive vehicle with a front and rear differential. These are driven from a constantly variable transmission (CVT) which has a high and low range.

Early in the design phase there were numerous teleconferences with Polaris Industries engineers and Sevcon USA Inc. applications engineers (motor drive manufacturer). These discussions helped finalize the selection of the major vehicle drivetrain components. There was some discussion about possibly building a hybrid research platform but this was dismissed early in the discussions due to complexity, cost and space constraints. Instead it was decided that a BEV would be built.

Figure 4.3: Donated ICE off-road vehicle.

It was decided that the ICE drivetrain would be removed and replaced with a one motor per wheel electric drivetrain. Early discussions favoured a two-speed transmission at each wheel position. The two-speed transmission would improve low-speed efficiency of the drivetrain [45] and raise available torque for low-speed off-road applications. This idea was abandoned because no suitable transmission was found. Instead a single speed transmission with a 5:1 ratio was selected for all four wheel positions. It was also agreed that no significant changes would be made to the donated vehicle chassis. The original suspension geometry and axle placements would be maintained.

Permanent magnet alternating current (PMAC) motors were selected as the traction motors for the vehicle. These motors exhibit better controllability at low speeds and higher torque than induction motors. They are also lighter and more efficient than induction motors of the same power [46]. The four motors of the vehicle would be controlled by four dedicated motor drives. The drives are commercially available and targeted to vehicle applications.

It was decided that Lithium iron phosphate batteries would be used for the battery pack because they have a higher specific energy density than lead acid batteries and are safer than other types of lithium ion batteries for vehicular applications [47]. In addition, they are readily available in a prismatic form factor making design and construction of the battery pack simpler.

4.3 Battery Pack

Eq. (3.32) in conjunction with Eq. (3.31) was used to calculate the power required to maintain 50 km/h in both hardpack and loose sand conditions: 11 hp and 19 hp respectively. The typical off-road driving condition is assumed to be 50% hardpack and 50% loose sand. The average power requirement for typical off-road driving conditions is then assumed to be 15 hp. A one hour or greater run-time in these conditions requires a battery pack with a capacity of at least 11.2 kW-h.

Figure 4.4: Single battery from vehicle battery pack.

Lithium iron phosphate batteries were chosen for the battery pack (CIE Solutions PB2S12P0). The battery is approximately 26 cm x 18 cm x 22 cm. The nominal voltage is 7.5 V with a capacity of 180 A-h. The maximum continuous discharge rate is 900 A with 2700 A pulse discharge rate (10 s). Continuous charge current is 900 A.

The pack consists of ten of these batteries connected in series to produce a 75 V pack with 180 A-h capacity, this equates to 13.5 kW-h. Therefore, this pack will support a greater than one hour run-time in typical off-road conditions.

4.4 Electric Motors

Based on Eq. (3.33) and Eq. (3.34) and the vehicle parameters in Table 6.1, a vehicle computer model was implemented in Matlab and run. The results of the simulation are shown in Figure 4.5. From this figure, the required total horsepower to just meet the required top speed specification for hardpack is approximately 80 hp. Based upon this

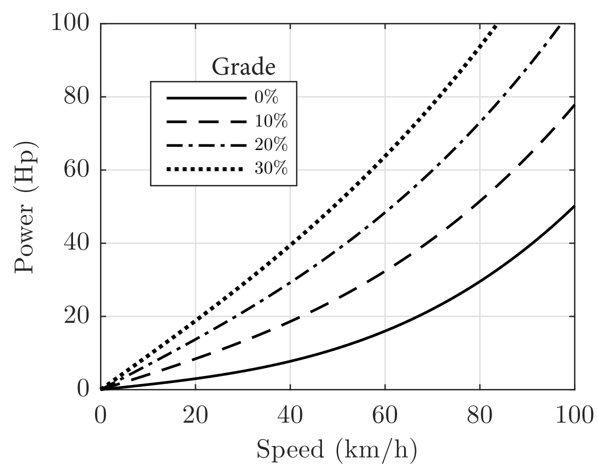

Figure 4.5: Simulated Steady-state Power vs Speed (Hardpack).

requirement and the available space in the vehicle chassis, two different Motenergy® PMAC electric motors were chosen. The ME4201 was chosen for the front motors due to space constraints at the front of the vehicle and motor cost. The ME1114 was chosen for the rear drive motors where there is more space for the larger motors. Total peak horsepower with these motor choices is 102 hp. It is also reasonable from a performance standpoint to have more power available at the rear wheels of the vehicle. There is typically more traction available at the rear due to weight transfer.

(a) Front motor

(b) Rear motor

Figure 4.6: Front and rear motors.

It is necessary that motor torque required during vehicle operation fall within the motor torque-speed envelope. The combined total maximum motor torque curve is shown in Figure 4.7 along with the total motor torque demand vs motor speed for different hardpack road grades. The torque demand plots range from 0 to 80 km/h ground speed. The motors are a good match to the total motor torque–speed envelope. The torque demand for the different driving conditions fall significantly within the torque speed envelope of the electric motors.

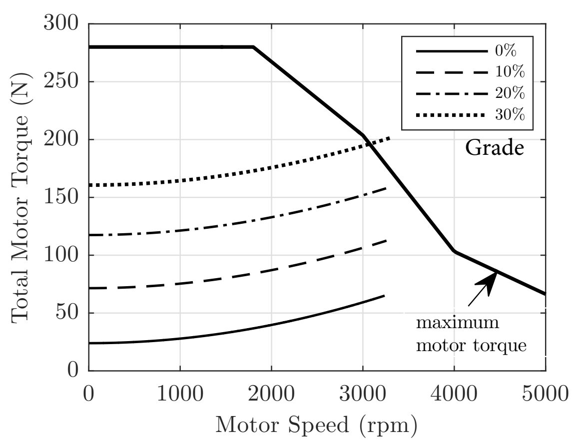

Figure 4.7: Simulated Steady-state Torque Demand (Hardpack).

It is interesting to compare the total torque available vs speed for the chosen motors and 5:1 ratio transmission to the original ICE equipped vehicle torque vs speed (high range). The four electric motors have more torque over the whole speed range and substantially more torque from 30 km/h and up. This is simply a result of the large (factor of 3) difference in horsepower.

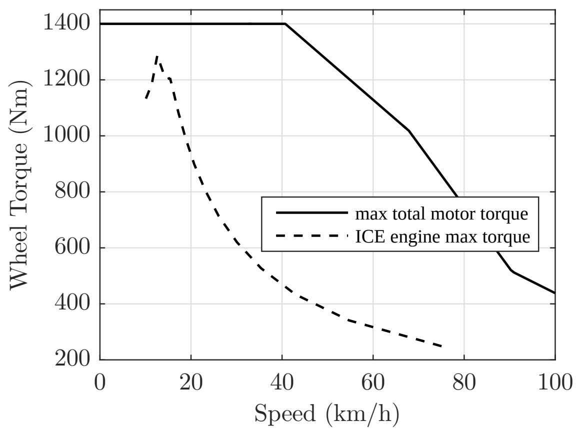

Figure 4.8: Original ICE vehicle torque comparison.

4.5 Motor Drives

Based on the selected battery pack, the selected motors and the vehicle specifications, a Sevcon Gen4 72/80 V 550 A motor drive was selected. This motor drive is used with all four motors. It is compatible with the selected battery pack voltage (75 V nominal) and can provide the peak current for the front motors (350 A) and the peak current for the rear motors (500 A). The motor drive is configured and controlled via a controller area network (CAN) bus interface [48]. Motor drive parameters are configured via the CAN bus interface using the manufacturer provided tuning software. In operational mode, the motor drive receives torque commands via the CAN bus interface and can provide monitoring of a large number of motor and motor drive quantities.

The Sevcon Gen4 motor drive family is designed for vehicle applications making it well suited for this application. The Gen4 motor drive family allows the detailed control of the motor operation. Maximum operating current versus motor speed is user programmable. In addition, the vehicle battery pack is protected from over discharge

Figure 4.9: Motor drive.

and over charge (regenerative braking) by allowing the user to specify the maximum and minimum pack voltage. Maximum current draw from the battery pack is also user adjustable. Motor temperature is monitored by this family of motor drives and will cut back motor current above a user adjustable maximum motor temperature.

4.6 Charger

An Eltek Valere EV Power Charger 3kW HE was selected for the onboard vehicle charger. This charger is designed for battery packs with a nominal voltage from 70 to 110 V (dc). It will provide a maximum of 25 A charging current allowing the

Figure 4.10: On board charger.

vehicle battery pack to be recharged from fully depleted to fully charged in less than 8 hrs. The input voltage range is from 85 to 275 V (ac). It will operate with a mains frequency range of 45 to 65 Hz.

4.7 Predicted Vehicle Performance–Validation

4.7.1 Performance Requirements

The vehicle is designed to perform as well as or better than the original donated ICE powered vehicle and have excellent off-road performance in loose sand and on hard packed clay (hardpack). The off-road EV research platform must meet the following specifications:

- The vehicle will climb a 40% grade in loose sand at 30 km/h or better and climb a 60% grade on hardpack at 30 km/h or better. It should manage a 20% grade at better than 80 km/h on hardpack and better than 60 km/h on loose sand.
- The vehicle will accelerate to 80 km/h in under 6 seconds on hardpack (level ground) and in under 10 seconds in loose sand (level ground). The top speed on level ground will be greater than 100 km/h on hardpack and greater than 90 km/h on loose sand.
- The vehicle will have a run-time of greater than one hour in typical off-road conditions.
- The vehicle will support skid steering.
- The vehicle also must function as a research platform for investigations into off-road traction and off-road electric vehicle drivetrain design.
- The vehicle will also support the development of off-road traction systems.

These requirements exceed the original donated vehicle specifications. The donated Polaris Ranger 500 has a top speed of approximately 75 km/h and can accelerate to 70 km/h in about 12 seconds.

4.7.2 Acceleration

Based on Eq. (3.43), Eq. (3.44) and the vehicle parameters in Table 6.1, a vehicle computer model was implemented in Matlab and run. The results of the simulation are shown in Figure 4.11. These results show that the predicted performance with the motors selected in section 4.4 meets the top speed and acceleration specifications for the vehicle outlined in section 4.7.1. The simulated vehicle accelerated to 80 km/h in 5.2 s for the hardpack condition and in 8.9 s for the loose sand condition. Predicted top speed is 104.5 km/h (hardpack) and 93.3 km/h (loose sand).

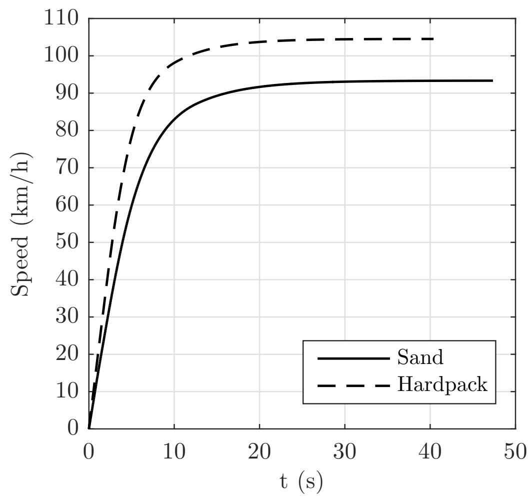

Figure 4.11: Simulated Speed vs Time (level ground).

4.7.3 Top Speed

Based on Eq. (3.45) and Eq. (3.42) and the vehicle parameters in Table 6.1, a vehicle computer model was implemented in Matlab and run in order to find v_x^{max} for different road slopes in loose sand conditions. The results of the simulation are shown in Figure 4.12. The results in Figure 4.12 show that the predicted performance with the chosen motors meets the grade-ability specifications from section 4.7.1.

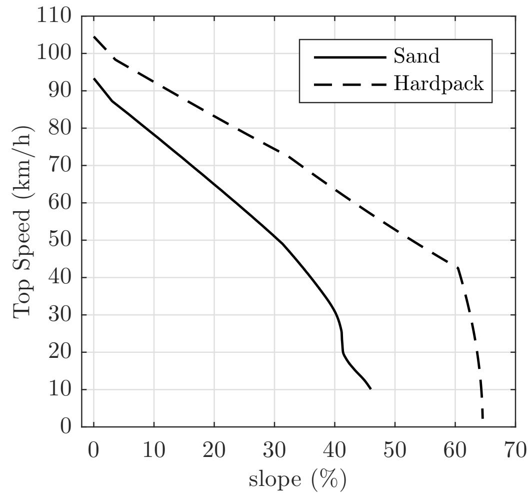

Figure 4.12: Simulated top speed vs grade.

4.7.4 Sinkage

The performance requirements set out in Section 4.7.1 have been exceeded by the simulated vehicle performance. It is also important to examine the vehicle sinkage which occurs at this level of performance. The sinkage must be substantially less than the radius of the tire to ensure that the vehicle doesn't become stuck.

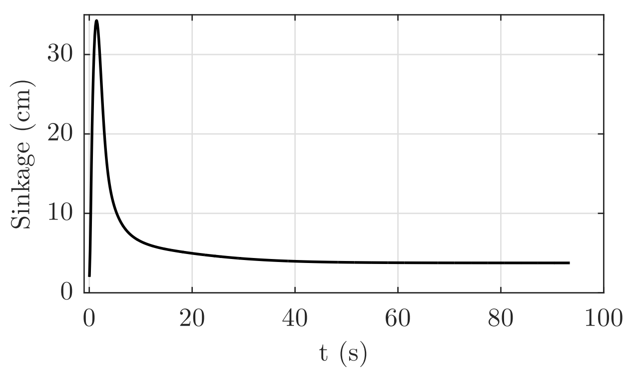

Figure 4.13: Sinkage in loose sand, no slip control, 40% grade.

Based on the results in Section 3.5.3, Eq. (3.27) and Eq. (3.29), a computer model was implemented in Matlab and simulated in order to find sinkage vs time during a maximum acceleration run. The simulation results are shown in Figure 4.13. It can be seen that the sinkage is excessive and needs to be mitigated. In fact the sinkage exceeds the tire radius and the vehicle would almost certainly be stuck.

It is assumed that the maximum sinkage for a wheel in loose sand should be kept at about 1/3 of the tire radius. With $z_{max} = 10$ cm and sinkage control implemented via Eq. (3.50), the simulation was run giving the results shown in Figure 4.14.

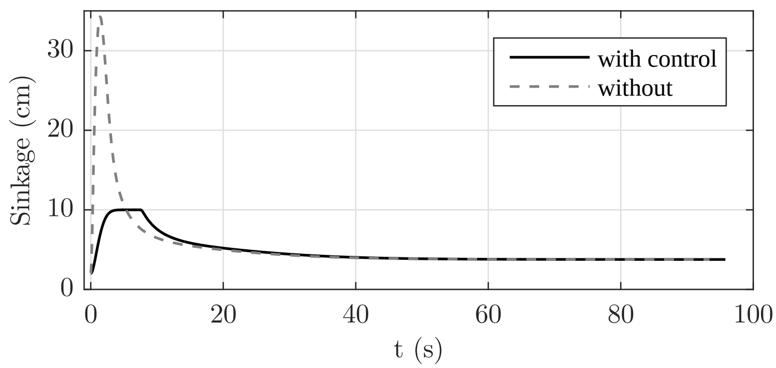

Figure 4.14: Sinkage in loose sand, with slip control, 40% grade.

Chapter 5

Design and Implementation

5.1 Chassis Preparation

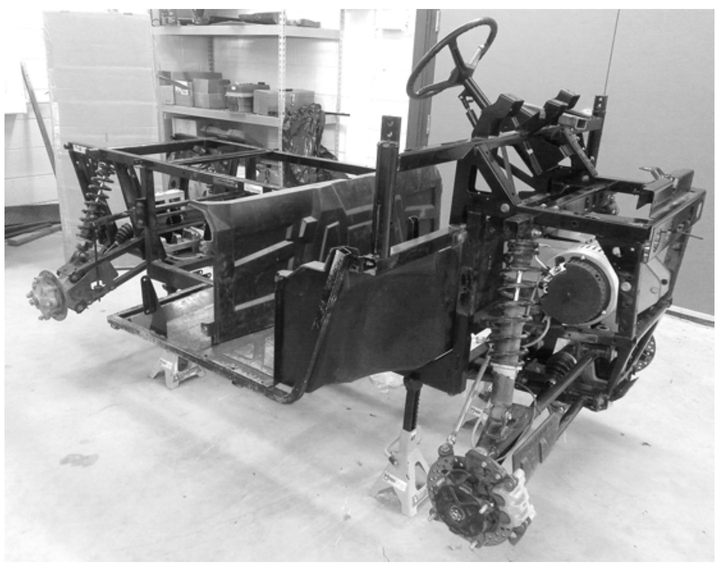

Figure 5.1: Vehicle chassis.

The donated Polaris vehicle was stripped of the original ICE power train. Because a one motor per wheel topology was chosen for the new electric drive train, all components of the original drive train were removed including the front and rear differentials. The original vehicle electrical system was also removed. All of the vehicle body panels were saved. These were reused and minimally altered to accommodate the new drive train and instrumentation. The original hydraulic brake system of the vehicle was left installed and unaltered. The original vehicle suspension and steering were also kept. Figure 5.1 shows the stripped down vehicle chassis.

5.2 Mechanical

The original vehicle front and rear differentials were replaced by transmission assemblies with the same mechanical interface at the output as the differentials. This allowed reuse of the original axles and left the suspension and braking system unaltered. The detailed mechanical drawings can be found in Appendix H.

A single speed transmission with a 5:1 ratio was designed using two #40 sprockets and a #40 roller chain. The transmission is composed of a jackshaft assembly and the motor mount. The jackshaft assembly has a 60 tooth sprocket with an internal spline that interfaces to the drive axle. The motor mount holds the motor with a 12 tooth sprocket mounted directly to the motor shaft. A roller chain connects the two sprockets. The motor mount assemblies are designed to allow chain tension to be adjusted. One end of the mounts is designed to pivot and the other end has slotted holes. Bolts secure the mounts at the slotted holes.

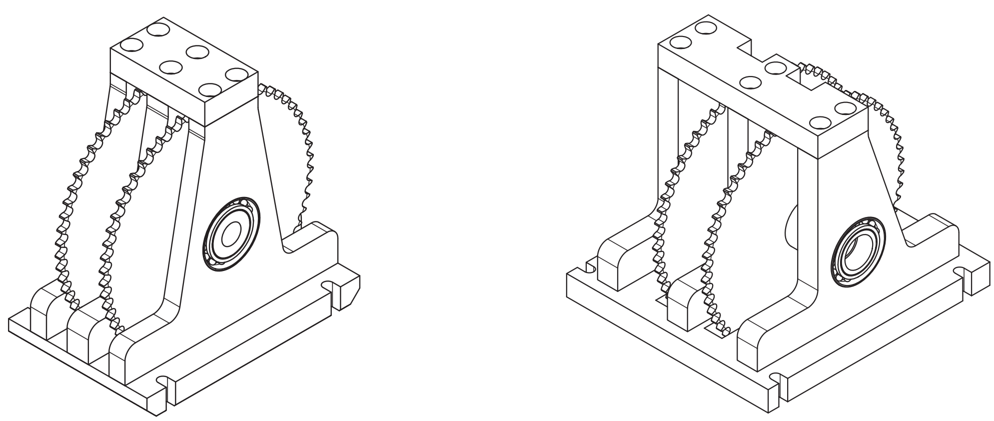

(a) Front Jackshaft Assembly　　(b) Rear Jackshaft Assembly

Figure 5.2: Design of Jackshaft Assemblies.

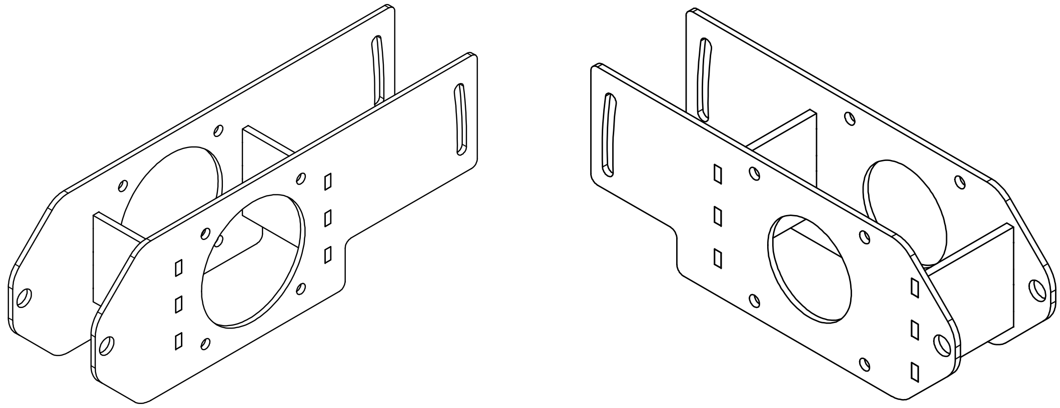

(a) Front Motor Mount (b) Rear Motor Mount

Figure 5.3: Design of Motor Mount Assemblies.

Solid modelling in Autodesk® Inventor® was used for the design of the vehicle transmission assemblies. The front and rear jackshaft assemblies are shown in Figure 5.2. The design of the jackshaft assemblies is quite rudimentary allowing fabrication with minimum machining. The assemblies are mostly composed of aluminum. The internally splined hubs and sprockets are made of steel. The front and rear motor mount assemblies are shown in Figure 5.3. The motor mounts consist of laser cut 3/16" hot rolled steel faceplates and gussets welded into an assembly.

Figures 5.4 and 5.5 show the completed transmissions. The front and rear transmissions are installed in the same position as the front and rear differentials. This is done to maintain proper alignment for the vehicle axles. Mounting of the transmission

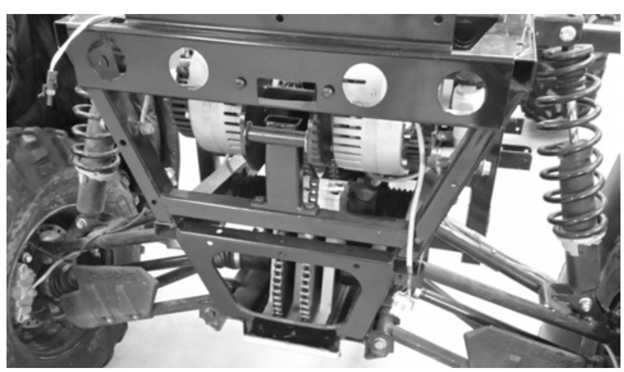

Figure 5.4: Front Jackshaft and Motor Carrier.

assembly required some modification of the vehicle chassis. Clearance for the large drive sprockets was cut into the bottom of the chassis. Mounting holes were drilled for each transmission to allow for mounting.

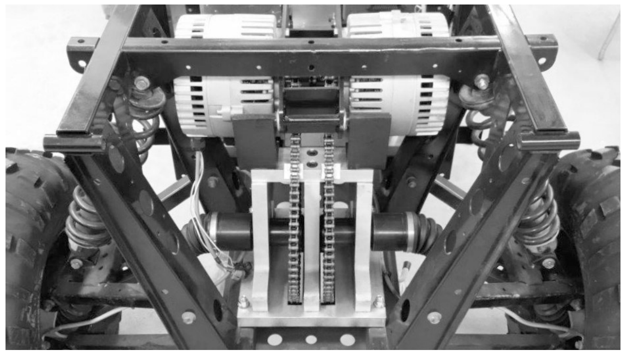

Figure 5.5: Rear Jackshaft and Motor Carrier.

Each traction motor has an associated motor drive. The four motor drives need a significant amount of cooling. Under rated driving conditions (15 hp), approximately 300 W will be dissapated by each pair of front and rear motor drives (see Figure 5.6). Air cooling was selected over water cooling due to ease of implementation. Large

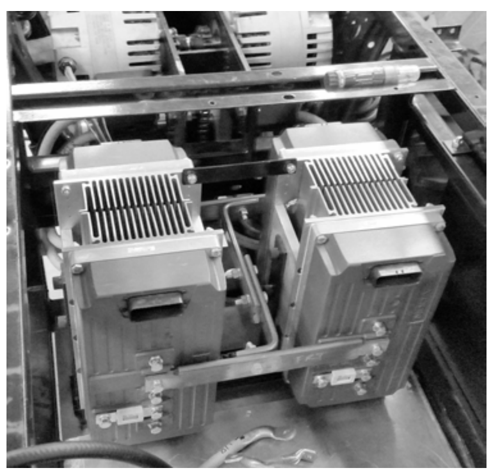

Figure 5.6: Motor drive cooling and buswork.

heatsinks running the length of each motor drive were attached to the motor drives. The attached heatsinks were used to form a finned duct by mounting the motor drives as shown. Fans were added to blow air down through the heatsinks (Figure 5.8b).

Also visible in Figure 5.6 is the heavy copper busbar that connects the four negative traction power terminals together (and to the battery negative terminal).

5.3 Subsystems Location and Mounting

The location of various vehicle subsystems and vehicle drivetrain components are shown in Figure 5.7. The vehicle subsystems are located based on the functional requirements of each subsystem. Possible interference from high current devices and high current wiring is accounted for in the choice of subsystem location. The high current 3 phase wiring running to each motor carries large sinusoidal currents with a high harmonic content making them a strong source of electromagnetic interference (EMI).

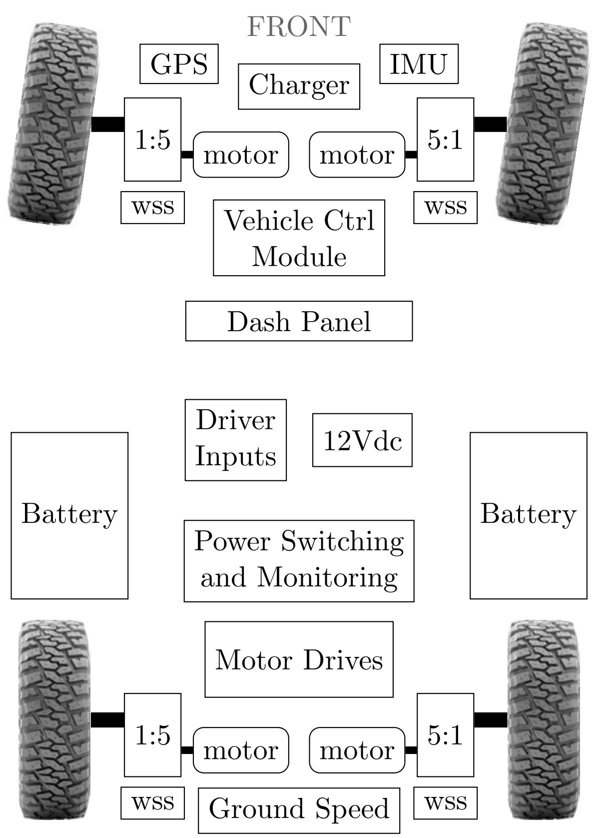

Figure 5.7: BEV Architecture.

Location and mounting of electrical components and routing of electrical wiring was determined by carefully accounting for sources of EMI. Signal wiring and sensitive electronic systems were routed and mounted far from the motor drives and all high current wiring. The VCM, GPS units, and IMU were all mounted in the dash area of the vehicle at the front. All subsystems were wired into the vehicle wiring with connectors allowing easy replacement and easy trouble shooting.

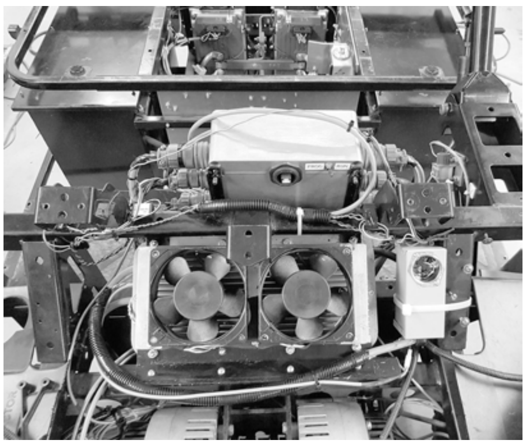

(a) VCM and Charger

(b) Motor Drives

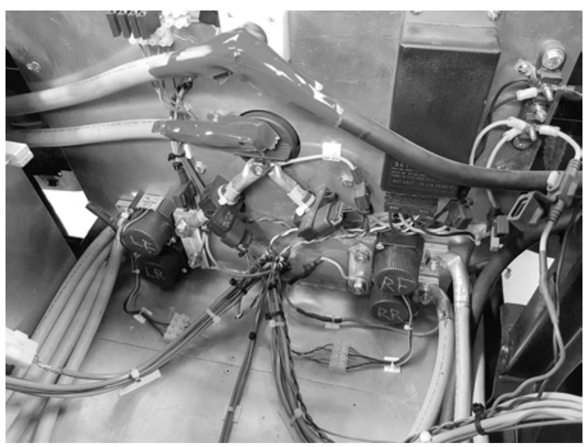

(c) Power

Figure 5.8: Subsystem mounting.

In Figure 5.8a the vehicle mounted charger is visible (two fans on top) with the VCM directly behind it. Figure 5.8b shows the four mounted motor drives (a cooling fan is on top of each pair of drives). Figure 5.8c shows the main power contactors, current sensors, 12 V(DC) supply and the two front motor drives.

In addition to the mounting of the major drive train components, numerous other smaller components were fabricated to allow mounting of various sensors, switches and displays (Figure 5.9). The radar based ground speed sensor (GSS) was mounted at

Figure 5.9: Dashboard.

the rear of the vehicle to give an unobstructed view of the moving ground behind the vehicle. The to GPS speed sensor and the IMU were located at the front of the vehicle under the vehicle dash. The GPS and GPS speed sensor antenna were mounted at the top of the roll cage over a small ground plane. A string type potentiometer was used to measure steering wheel position. It was located under the steering column. The throttle position sensor was mounted in the electronics bay found in the center of the vehicle. It is actuated with the original vehicle throttle cable.

5.4 Electrical

Vehicle traction power is switched using four contactors (one per motor drive). Power is routed from the batteries to the contactors through a main disconnect switch (isolator) which is accessible by the driver of the vehicle. The battery pack is divided into

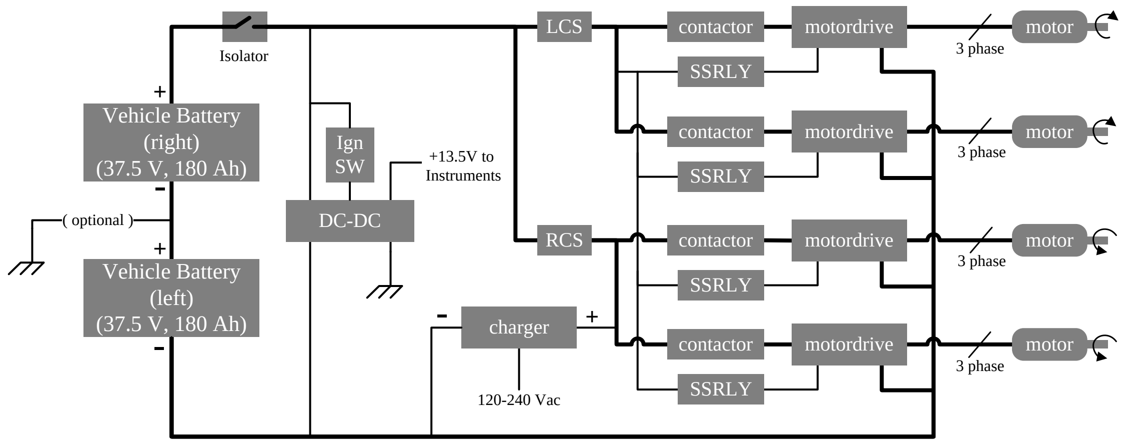

Figure 5.10: Traction power.

two packs mounted on the left and right side of the vehicle. An optional grounding point is provided which may be connected to vehicle ground with a light gauge wire limiting the maximum traction voltage to ±37.5 V relative to ground.

The battery current draw is monitored by two current sensors each rated for 1000 A. Expected peak current draw from the batteries is approximately 1800 A. Power circuit wire and cable selection is based upon the current carried by the different circuits [49]. The DC traction power from the batteries is carried by #0000 cable. The 3 phase current to the rear motors is carried by #0 cable and by #0000 cable to the front motors (much longer cable run). The motor drives are located toward the rear of the vehicle near the rear motors.

Figure 5.10 illustrates the traction power wiring. The vehicle ignition switch is a double pole double throw switch. One pole of the switch is used to indicate whether the vehicle is in run mode or charge mode (logic level signal). The other pole is used to enable the DC-DC converter (350 W) that supplies +13.5 V power to the VCM, vehicle instruments and vehicle lighting. Solid state relays, controlled by the VCM, are used to switch the circuit power to each motor drive.

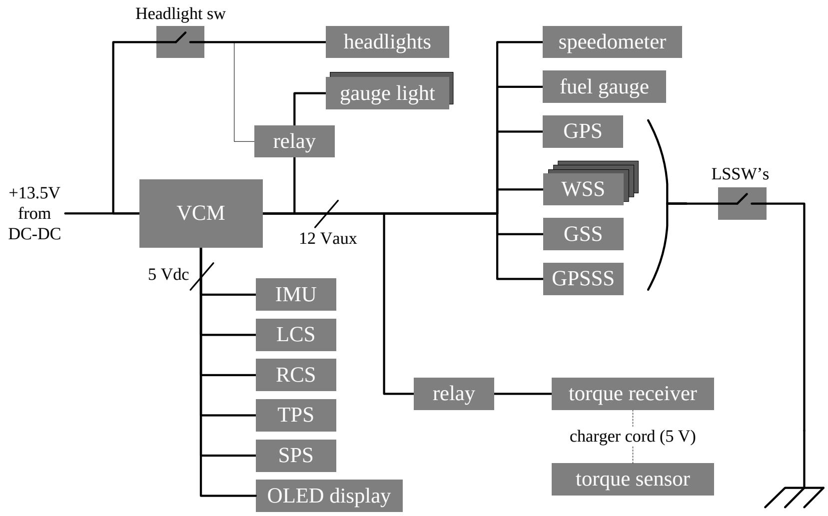

Figure 5.11: Instrument power.

The distribution of instrument power is handled by the VCM (Figure 5.11). The VCM provides regulated 5 V power as well as unregulated 12 V power (diode protected). Switched power is provided to the GPS, GSS, WSS's and GPSSS. The balance of the instruments receive power whenever the VCM is powered up. All of the instrument power connections are fused with self resetting fuses and filtered to mitigate EMI.

The vehicle headlights are powered directly from the DC-DC converter and controlled by a dash mounted switch. Gauge lighting is switched with the headlights via an isolation relay. Power to the torque transducer receiver is switched via an isolation relay controlled by the VCM. A charger cord is provided to allow recharging of the axle mounted torque transducer.

Figure 5.12 shows all of the vehicle sensors, instrumentation and associated signal interfaces. The majority of vehicle control and monitoring is handled by the VCM. Numerous different physical interfaces are provided by the VCM to interface with the various instruments and sensors. These interfaces range from simple digital I/O's and

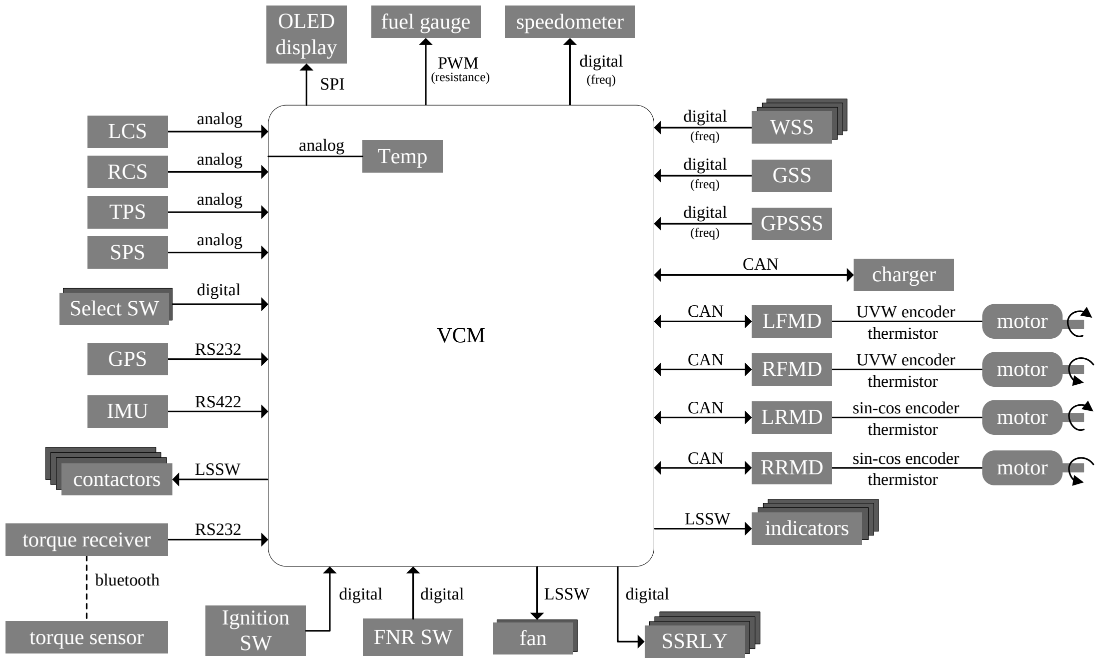

Figure 5.12: Vehicle control and monitoring.

analog inputs to complex protocol based communications channels (for example CAN bus).

The motor drives provide some additional control and monitoring functionality such as monitoring the battery voltage, battery current draw, motor current, motor voltage and motor temperature. The motor drive protects the vehicle battery from extreme current and voltage levels. These monitored values can be accessed via the CAN bus interface on each motor drive. In addition, various motor parameters, operating parameters and battery protection settings can be set through the CAN bus interface.

5.5 Vehicle Control Module

5.5.1 Hardware

The completed and assembled VCM consists of three circuit boards, the FPGA board (Figure 4.1), the interface board (Figure G.11), the expansion board (Figure G.14), an aluminum enclosure and various mounting hardware. The interface board plugs into the FPGA board expansion headers. The expansion board plugs into the expansion headers on the interface board. The completed VCM, a stack of 3 circuit boards, is shown in Figure 5.13.

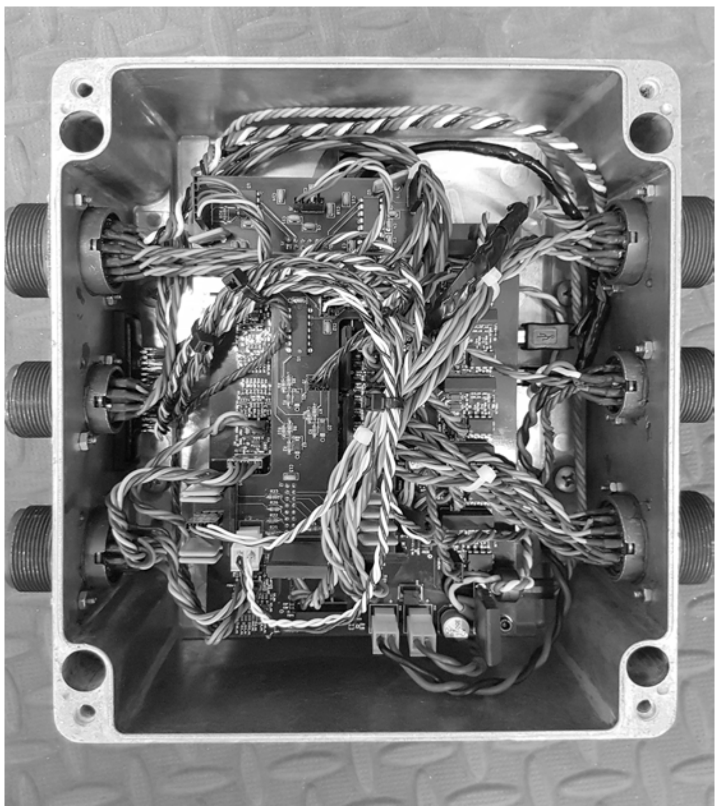

Figure 5.13: VCM.

The interface board uses surface mount technology (SMT) for most of the components and is a modern dense four layer printed circuit board (PCB) designed in Altium®. The expansion board uses mostly through-hole components for ease of assembly and is a modern dense four layer PCB designed in KiCad. Design and layout of the circuitry for the interface and expansion boards followed good engineering practices [50] [51] [52]. In particular, the layout of the PCB's was guided by [53] and [54].

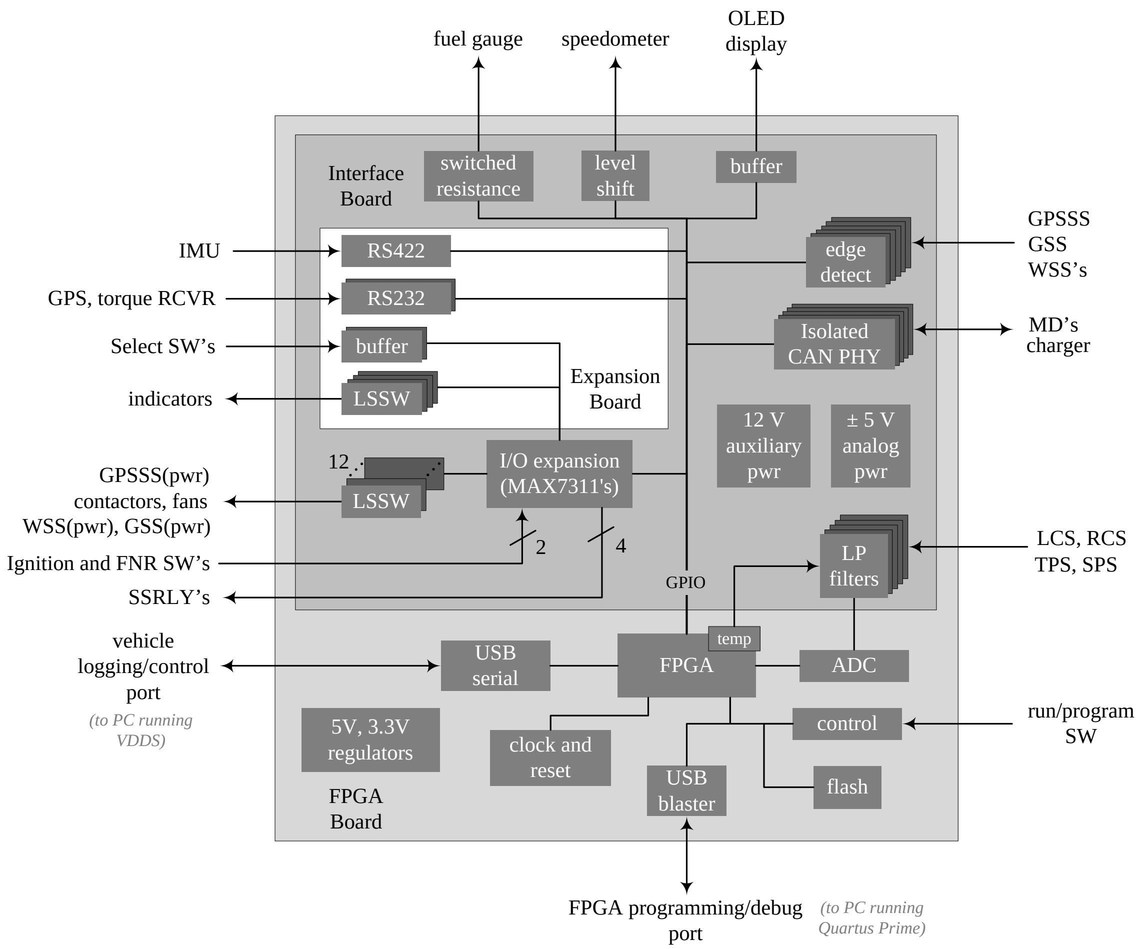

Figure 5.14: VCM circuit (block diagram).

The VCM is based on the FPGA board chosen in section 4.1.4. The FPGA board provides two USB ports; one for debugging and programming of the FPGA and one for general use (used for data logging and vehicle debugging). Flash memory is provided that stores the FPGA code and also stores code for the embedded processor instantiated in the FPGA. Voltage regulators, clocking and reset circuitry are provided for the FPGA and peripherals. In addition, a 12 bit ADC is provided to allow capture of analog signals. These peripherals are connected to the FPGA via general purpose I/O (GPIO) pins. A subset of the FPGA GPIO pins is available on expansion headers. A dedicated expansion header is also provided for the analog input channels. The Interface Board plugs into these expansion headers.

The Interface Board provides the bulk of the instrument and sensor physical interfaces for the vehicle. The physical interface circuitry provides voltage level translation, impedance matching, isolation etc. as required to match the instrument and sensor circuitry to the FPGA GPIO's. Some low side switches (LSSW) are provided to control power to some of the instruments and sensors. Low pass anti-alias filters are provided for the analog inputs (1 kHz cut off 3rd order). An I/O expansion integrated circuit is included (MAX7311). It is controlled via an I2C interface to the FPGA. It expands the number of digital I/O's available from the FPGA. Isolated CAN bus physical interface circuitry is provided to the 4 motor drives and the charger. Isolation is important because the devices do not share a ground connection with the VCM .

The Interface board provides a subset of FPGA GPIO and I/O expansion pins on two expansion headers. The Expansion Board plugs into these expansion headers. It provides some additional physical interfaces for devices added at a later date in the vehicle design.

5.5.2 FPGA Code

The selected FPGA board replaces the more typical embedded processor system that is used in vehicle applications. As mentioned in section 4.1.4, the FPGA board is a more flexible architecture that allows a custom peripheral interface and processing architecture to be implemented. Figure 5.15 shows the proof of concept implementation used to test and characterize the vehicle. It is important to emphasize that this is just one possible implementation. Other architectures are possible which may include features such as multiple processors and hardware assisted control algorithms. All of the functionality is described by FPGA code which is compiled and downloaded to the FPGA.

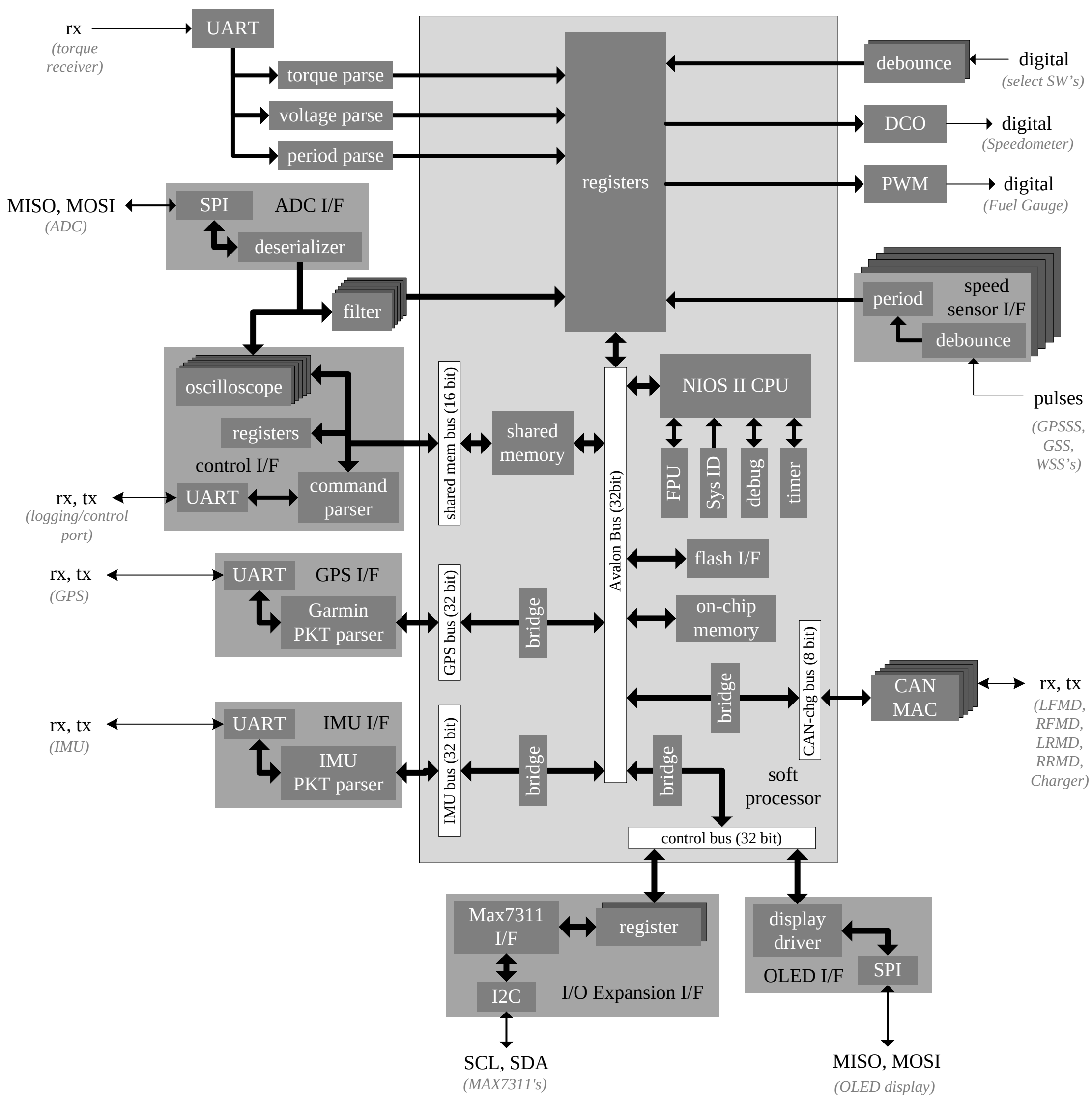

Figure 5.15: FPGA code (block diagram).

The selected FPGA board contains an Intel Cyclone V (5CGXFC5C6F27C7) FPGA. This is a small to mid-sized low cost FPGA. The code development was done with Quartus Prime 15.1 Standard Edition IDE (Intel software). In Figure 5.15, the soft embedded controller corresponds to all of the components in the central light gray block. A NIOS II processor forms the foundation of the embedded controller. All of the blocks used here are from a library provided by Intel. The soft embedded controller is implemented using QSYS 15.1 which is an Intel provided tool that allows library components to be assembled into a subsystem graphically. The output is Verilog code that is imported into the Quartus Prime project.

The outer blocks are written directly in Verilog and System Verilog. These blocks provide the various interface protocols required to interface to the vehicle subsystems. A CAN bus interface provides communication to and from the motor drives. The ADC's, which digitize the throttle position, steering position and battery current, are connected via an serial peripheral interface (SPI) interface. The various speed sensors, gauges and vehicle status and control display are connected via custom digital interfaces. A serial interface was implemented, it allows debugging of the vehicle software and enables data logging during vehicle operation. This block also supports capture of the analog channels for debugging (oscilloscopes).

The top level entity in the design is a Verilog file that ties all of the blocks together. Compiling the code in Quartus Prime produces a configuration file that is downloaded into the flash memory on the FPGA board. At power up, the flash contents are loaded into the FPGA at which point the FPGA provides the functionality shown in Figure 5.15.

The utilization of various resources in the FPGA by the proof of concept code is shown in Figure 5.16. Except for memory block usage the FPGA chosen is only about one third utilized leaving a lot of space for added functionality such as more processors or hardware assisted processing. The NIOS II processor (a complex component) typically uses 1500 to 3000 logic units. Memory block usage could be reduced by making use of the external memory modules on the FPGA board.

Flow Summary	
Flow Status	Successful - Thu May 30 19:35:15 2019
Quartus Prime Version	15.1.0 Build 185 10/21/2015 SJ Standard Edition
Revision Name	EUV
Top-level Entity Name	EUV
Family	Cyclone V
Device	5CGXFC5C6F27C7
Timing Models	Final
Logic utilization (in ALMs)	9,815 / 29,080 (34 %)
Total registers	14291
Total pins	134 / 364 (37 %)
Total virtual pins	0
Total block memory bits	2,933,064 / 4,567,040 (64 %)
Total DSP Blocks	13 / 150 (9 %)
Total HSSI RX PCSs	0 / 6 (0 %)
Total HSSI PMA RX Deserializers	0 / 6 (0 %)
Total HSSI TX PCSs	0 / 6 (0 %)
Total HSSI PMA TX Serializers	0 / 6 (0 %)
Total PLLs	2 / 12 (17 %)
Total DLLs	0 / 4 (0 %)

Figure 5.16: FPGA code compilation results.

5.6 Vehicle Software

The vehicle control and monitoring functions must execute in real-time and execute fast enough to keep up to driver demands and vehicle dynamics [55]. The selected FPGA development board provides the speed and flexibility to support all of the required interfaces and run the vehicle management and control software (VMCS) in real-time.

A NIOS II processor was instantiated in the FPGA using QSYS version 15.1. All control and monitoring of the vehicle systems is handled by the VMCS running on the NIOS II processor. The code is written in C and was developed with Nios II 15.1 Software Build Tools for Eclipse. The code runs under a real-time operating system (μC/OS-II [56]) and is task and interrupt based. All vehicle data flow is managed at the hardware level in the FPGA and passed via a processing interrupt to the NIOS II processor.

The VMCS main function shown in Figure 5.17 initializes and configures the vehicle for charging (charge mode) or operation (run mode). Once the vehicle enters either run mode or charge mode (selected by ignition switch position), the vehicle control and monitoring is handled by the interrupt service routines and tasks launched from the main function.

In run mode, the processing and MD interrupt service routines handle data transfer from the various interfaces to CPU memory space. The processing interrupt is triggered by a hardware timer in the FPGA at a rate of 200 Hz. All of the values captured from the vehicle peripherals are transferred at each interrupt. Certain vehicle

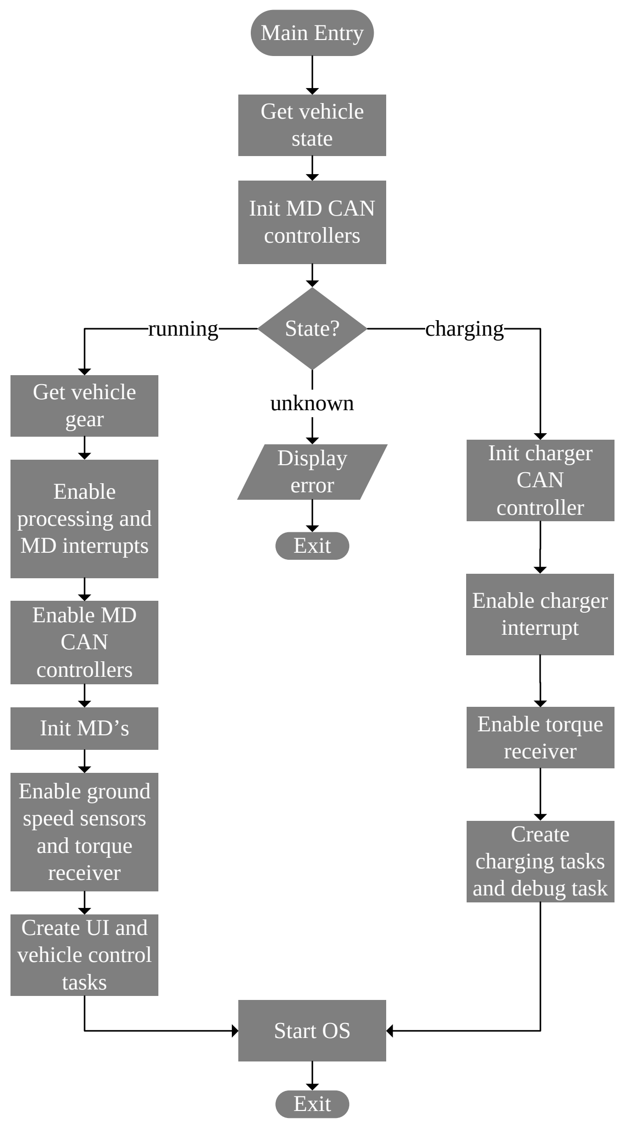

Figure 5.17: VMCS main function flow chart.

operating values (battery voltages and currents, motor voltages and currents, actual torque command, and motor speed) are transferred from the motor drives . These values are sent on each of the CAN bus interfaces by the motor drives at 10 Hz except for motor speed which is sent at a 100 Hz rate.

The control task (launched when the vehicle is in run mode) translates throttle commands to torque commands for the motor drives. In the current proof of concept VMCS, the throttle command is converted to directly into a percentage torque command that is sent to each motor drive. Each motor drive receives the exact same torque command so that each side of the vehicle receives the same amount of torque (mimicking the function of a differential). Additionally, the control task copies vehicle data to the shared memory area in the FPGA for data logging.

The vehicle user interface (UI) is provided by the UI task in run mode and by the charging tasks in charge mode. In run mode, the VMCS via the UI task provides vehicle status information to the four line display in the vehicle dash. The display is controlled via two push button switches. Different status and control displays to be selected by use of the two switches. The traction mode of the vehicle is set via the display and push button switches. Four modes are available for selection: all-wheel drive, rear wheel drive, front wheel drive and skid steer.

In run mode, all of the vehicle operating voltages, currents and temperatures may be displayed. The IMU data, GPS data and torque sensor data are all available for display. The UI task also updates the speedometer, fuel gauge and gear selection display.

In charge mode, the four line display is fixed and displays charging current and voltage along with charger temperature and mains voltage and current. Charging is fully automatic and starts when the AC mains is connected to the charging port. The charging current and voltage are managed by the charging tasks. The charger is activated by sending charging commands at a rate of 5 Hz. CAN bus communication with the charger is handled via the charger interrupt service routine.

Additionally, in charge mode the vehicle supports debugging which allows remote control and monitoring of some of the vehicle subsystems. The debug mode can be started from the vehicle data logging and debug software (VDDS). Charging is disabled when in debug mode.

5.7 Data Logging and Debug Software

The VCM has a USB port dedicated to debugging and data logging (see Figures 5.14 and 5.15). Debugging is supported when the vehicle is in charge mode and data logging is supported when the vehicle is in run mode. The USB virtual serial port connects to a PC running custom software that implements the data logging and debug features. The VDDS is written in Visual C++ using Microsoft foundation classes (MFC).

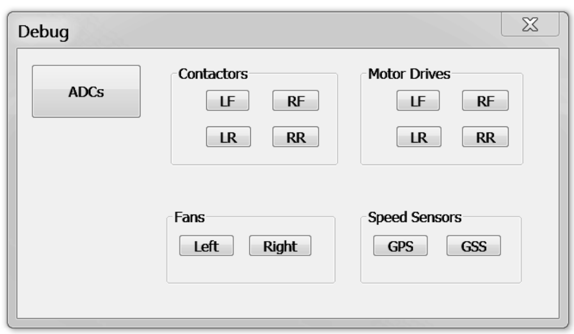

Figure 5.18: Debug interface.

The shared memory region (see Figure 5.15) is used to pass button status to the VMCS when the vehicle is in debug mode. In run mode, the shared memory region is used by the VMCS to pass vehicle parameters to the VDDS. The VMCS sets a flag whenever data is ready for reading by the VDDS. A circular buffer is maintained by the VMCS and VDDS to avoid data drops. The VDDS writes the vehicle parameters to a comma delimited file. A routine was written in Matlab to produce a summary set of plots from the logged data (see section F).

Chapter 6

Vehicle Performance

6.1 Early Testing and Setup

The driving mode is selected when the vehicle ignition switch is turned clockwise from the off position. Initial testing of the vehicle in driving mode happened during configuration of the motor drives. The vehicle was lifted up onto jack stands leaving the wheels of the vehicle free to turn. The speed control loop was validated with the

Figure 6.1: Dynamometer Testing (U of M).

vehicle wheels turning freely. The vehicle speed was governed at 80 km/h for all testing to date. Drivetrain oscillation caused by play in the drivetrain was eliminated by tuning the torque control loop parameters of the motor drives. Loading was provided by the vehicle hydraulic disc brake system.

Some further tuning of the torque control loop parameters was carried out by mounting the vehicle on a wheel dynamometer Figure 6.1 in the EV lab. The vehicle was positioned with the rear wheels on the dynamometer roller. The capability of the motor drive and motor cooling systems was also partially tested by operating the vehicle on the dynamometer. The vehicle speed was varied to provide loading through the inertia of the dynamometer roller. Some loading was provided by the dynamometer magnetic brake as well. The temperature of the rear motors remained below 85 °C. The temperature of the motor drives remained below 32 °C.

Figure 6.2: Winter test drive.

In addition to the lab testing. Some preliminary qualitative field testing of the vehicle was performed in winter and autumn. The vehicle drove and handled well in the adverse winter driving conditions (Figure 6.2). It also performed well in hard pack terrain (Figure 6.3) easily climbing an approximately 50 % grade.

The early field testing and the associated collected data logs allowed preliminary

(a) Facing hill (b) Side view

Figure 6.3: Dike climbing.

calibration of the vehicle speed sensors. The data logs also verified the functionality of the balance of the vehicle instrumentation.

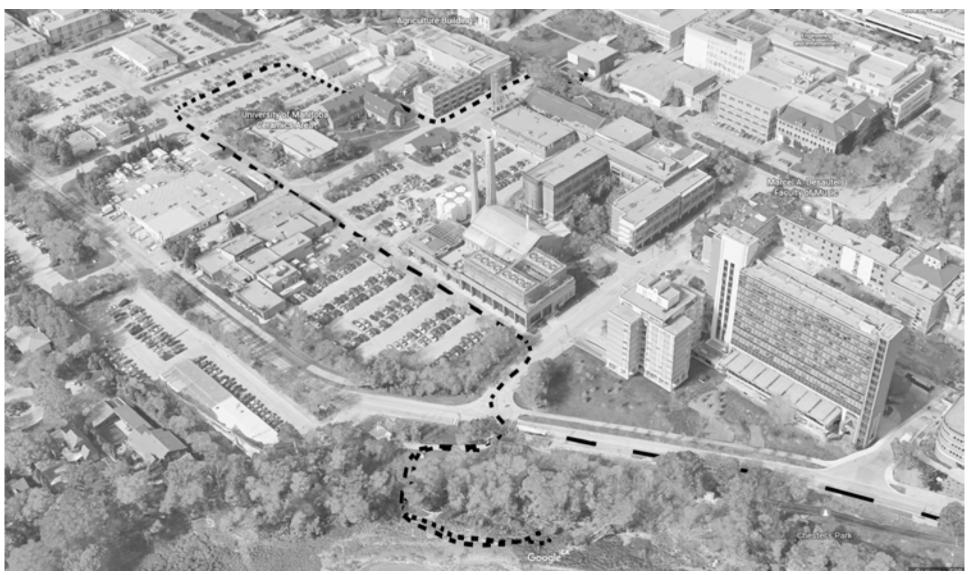

Figure 6.4: Drive around campus (GPS path).

Short trips on campus were taken occasionally for testing purposes. Figure 6.4 shows a trip around campus used to verify some software changes. This trip included a small off-road excursion along the bank of the Red River.

6.2 Drive Train Performance

An attempt was made to measure the torque at the rear wheels using the EV lab dynamometer in inertia only mode (relying upon drum inertia to load the drivetrain). These results were not consistent with the expected torque speed curves of the front and rear motors. It was determined that the dynamometer was either not correctly calibrated or not correctly configured. An off-site dynamometer was used for further testing.

Figure 6.5: Transporting vehicle to offsite dynamometer.

A hub dynamometer would have been the preferred equipment for testing the vehicle performance. This type of dynamometer has the advantage of being able to test the power output at fixed speeds (not relying on inertia at all). It was however not possible to couple the vehicle to a hub dynamometer. None of the contacted facilities had the correct adapter for this vehicle type. Ultimately the vehicle was transported to Speed Factor Racing (Winnipeg, MB) for further dynamometer testing. The dynamometer at this facility is a drum type wheel dynamometer providing drum inertia and brake loading. This dynamometer had been recently installed and recently calibrated.

Figure 6.6 shows the vehicle strapped to the dynamometer for front motor power

Figure 6.6: Off-site dynamometer testing.

measurement. The dynamometer was configured to measure wheel horsepower vs drum speed. The brake loading feature was not used. All of the test pulls on the dynamometer were done using only the drum inertia. Typically wheel dynamometers are used to get an estimate of the engine horsepower of a vehicle. The dynamometer software corrects the measured wheel horsepower to give engine horsepower. This feature was disabled during all tests.

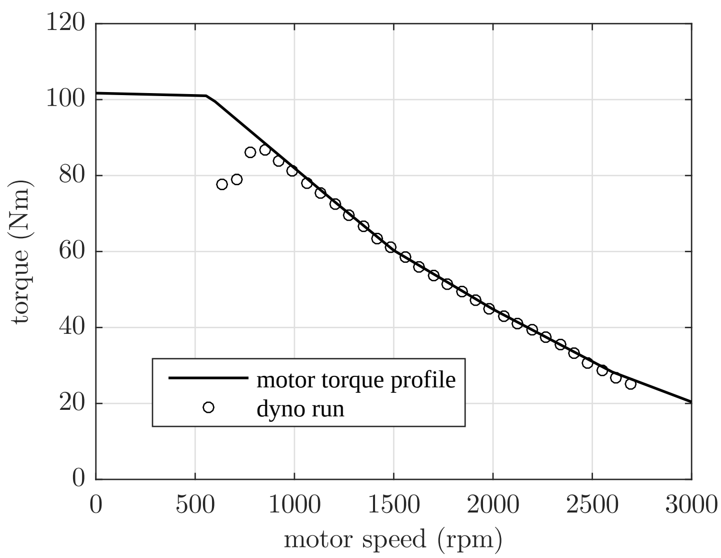

Figure 6.7: Front motors dynamometer run.

The horsepower vs wheel speed data collected from the dynamometer runs was converted to motor torque vs motor speed data. The resulting torque vs speed results were calibrated to the measured stall torques for the front and rear motors respectively (see Appendix C). The measured results are compared to the respective motor torque

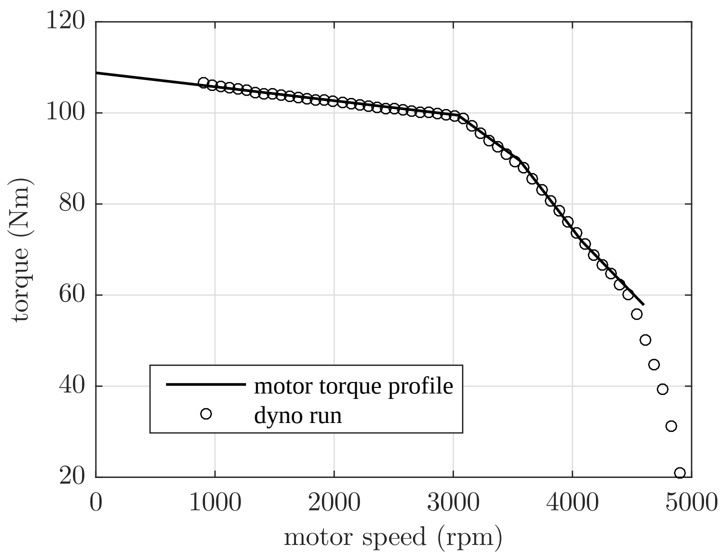

Figure 6.8: Rear motors dynamometer run.

profiles (the expected torque vs speed curve for each of the motors). The profiles are based on the corrected motor current maps (Appendix B). The motor current maps are programmed into the respective motordrives. The current maps were provided by the motor manufacturer and approximately follow the hyperbolic constant power curve after base frequency. The initial flat portion of the map is determined by the maximum motor current. The current maps are scaled by the respective motor torque constants (Appendix A) and compensated for electrical and windage losses in the motors (Appendix D). The calibrated dyno run results are plotted in Figures 6.7 and 6.8. The agreement between the measured results and the respective calculated motor torque profiles is good.

The front motor dynamometer results show some deviation from predicted above 2400 rpm. Operation in this region requires significant field weakening to be in effect because of the motor K_e and the battery voltage. Field weakening in a permanent magnet machine is accomplished by raising the direct axis component of the stator current to counteract the field of the permanent magnets on the rotor thus decreasing the back EMF of the motor. This keeps the motor terminal voltage lower than the motordrive output voltage. The counteracting field is limited to a maximum value to prevent permanently demagnetizing the rotor permanent magnets. It is possible that the maximum limits for d-axis current have been reached at or around 2400 rpm resulting in the drop off of torque. The dip in front motor torque below about 800 rpm is due to the dip in the motor current map which is explained in Appendix B.

The rear motor dynamometer results show some deviation from the predicted torque above about 4400 rpm. This deviation can be fully attributed to the soft onset of the vehicle speed governor.

6.3 Hardpack Field Testing

The vehicle was transported to a rural area for performance testing on a hardpack road surface (see Figure 6.9). Two maximum acceleration tests were conducted on the hardpack road surface both with and against the wind. Following the acceleration

(a) Hwy 59 and south floodway near Winnipeg, MB (© Google)

(b) Hardpack road surface

Figure 6.9: Hardpack field testing.

tests the vehicle was driven extensively on the hardpack road surfaces available in the area. The driveability and handling of the vehicle were excellent. There was no power over or under steer noted during any of the driving. This validated the practice of providing balanced torque to all four wheels similar to what is accomplished with an all wheel drive system in a vehicle with a single engine/motor. Some short excursions were also made onto some hardpack trails running in and along the Red River Floodway. Again handling and maneuverability of the vehicle were both excellent. In total the vehicle was driven for approximately 2 hours on mostly hardpack surfaces at moderate to lowspeeds. At the end about 25% battery capacity remained. Drive time was significantly longer than expected because of the low average vehicle speed and the hardpack surface. Motor temperatures stayed well below the maximum cutoff temperature of 110°C.

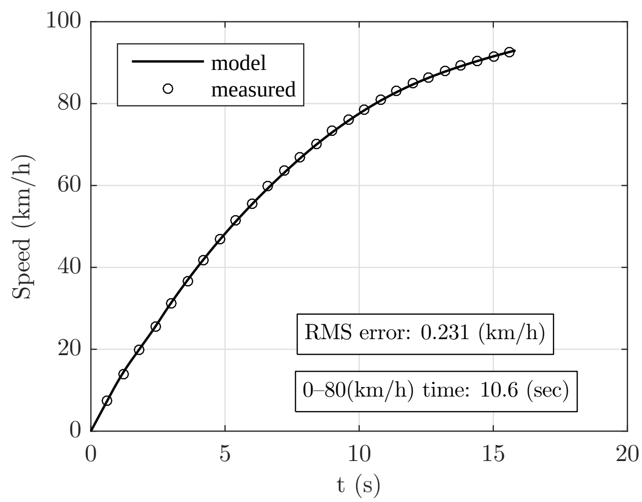

Figure 6.10: Hardpack acceleration test: 22 km/h tailwind.

The two maximum acceleration tests were conducted on the stretch of hardpack road highlighted in Figure 6.9a. The tests were run back to back in quick succession. A pass was made in one direction and then immediately the vehicle was turned around and a pass was made in the opposite direction. There was a gusty 23–24 km/h wind blowing during the testing at approximately 20 degrees to the road so that there was an effective wind speed of 22 km/h either against or with the vehicle during the tests. The road surface had essentially zero slope which was later verified from examination of the data log. The height variation along the road was less than 0.5 m and was random. The vehicle battery was essentially fully charged before the maximum acceleration tests.

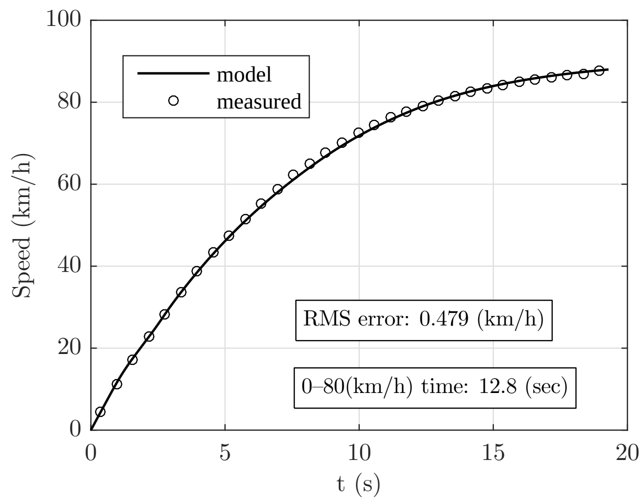

Figure 6.11: Hardpack acceleration test: 22 km/h headwind.

The results of the two maximum acceleration passes are shown in Figures 6.10 and 6.11 (measured data points). The results from simulation of the vehicle model (from Chapter 3) are also plotted in these figures. There is excellent agreement between the predicted vehicle speed and measured speed particularly for the tailwind test pass. The larger discrepency seen at around 10 seconds in the headwind pass is most likely due to a wind gust.

The vehicle model was updated to include the actual measured mass of the vehicle, the mass of the driver and the equivalent mass of the rotating drivetrain components. The rotating components of the vehicle experience a linear as well as rotational acceleration. The effective mass of a rotating component is given by,

$$M_{eff} = J\left(\frac{n}{r}\right)^2, \tag{6.1}$$

where J is the moment of inertia, n the gear ratio and r the wheel radius. The vehicle drag coefficient was adjusted to give good agreement between the simulation results and the measured results. The vehicle frontal area was updated to provide a more realistic estimate of the vehicle frontal area. In addition, the vehicle model was updated to include the effect of wind on the vehicle air drag force.

Table 6.1: Updated vehicle parameters.

Parameter	Value	Units	Description
M	765	(kg)	vehicle mass
M_d	100	(kg)	driver mass
M_r	49	(kg)	equivalent mass due to rotational inertia
A_f	2.1	(m^2)	vehicle frontal area
C_v	0.6		vehicle drag coefficient
p	15	(psi)	tire pressure

The vehicle acceleration is slower than the initial predictions made in Section 4.7.2. The total motor torque available over the operating range is much lower than was assumed in the initial simulations. These torque curves were based upon information provided by the motor manufacturer and distributor. The actual available torque, especially for the front motors, is significantly lower. In addition, the mass of the vehicle was slightly underestimated and more importantly the mass of the driver and effective mass of rotating components was not included in the initial simulations.

6.4 Loose Sand Field Testing

Loose sand field testing took place at the end of October. The local weather conditions in Southern Manitoba had deteriorated to the point where outdoor testing of the vehicle would not be possible. Alternative indoor test locations were sought. Indoor horse arenas were the only real viable option that was found. Several were contacted and Cloud Nine Ranch near Steinbach, MB agreed to rent out their indoor horse arena on an hourly basis for vehicle testing. The facility has an 80' by 160' indoor arena with loose non-packing sand riding surface.

Figure 6.12: Indoor horse arena (near Steinbach, MB).

The vehicle was transported to Cloud Nine ranch on a flatbed trailer. After unloading, the vehicle was driven into the indoor arena. The maximum acceleration of the vehicle was measured in the indoor arena. Following the maximum acceleration testing the vehicle was driven extensively inside the arena. The vehicle speed was limited to below 30 km/h because of the size of the arena. Handling and maneuverability in the loose sand were excellent. The vehicle exhibited no power under or over steer. In total the vehicle was driven for about 1 hour.

Figure 6.13: Wheel spin under hard cornering.

During hard driving (Figure 6.13), full to near full throttle with lots of hard cornering, it was possible to overheat the front motors within about 1 minute. The rear motors never overheated. At the end of all the testing approximately 30% capacity remained in the vehicle battery.

The maximum acceleration test was run with the battery capacity at essentially 100%. The arena sand had been freshly harrowed and leveled. The arena is sheltered from the wind and is level. Only one maximum acceleration pass was made. The results of the maximum acceleration test are shown in Figure 6.14 (measured data points). The results from simulation of the vehicle model (from Chapter 3) are also plotted in this figure. There is very good agreement between the predicted vehicle speed and measured speed. The low maximum speed attained during the test is a result of the limited space available. The vehicle had to both accelerate and stop within the confines of the arena.

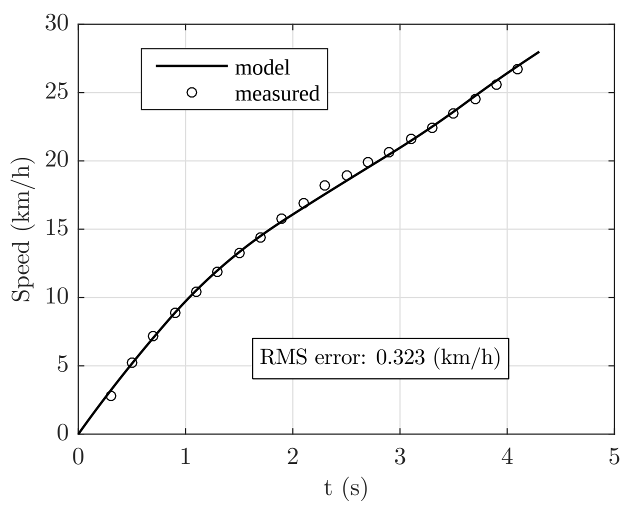

Figure 6.14: Sand acceleration test.

Figure 6.15 shows the measured slip during the maximum acceleration test (measured data points). The results from the simulation are also shown in this figure. There is definitely some correlation between the measured and simulated results but the agreement is quite bad overall. One significant contributing factor to the discrep-

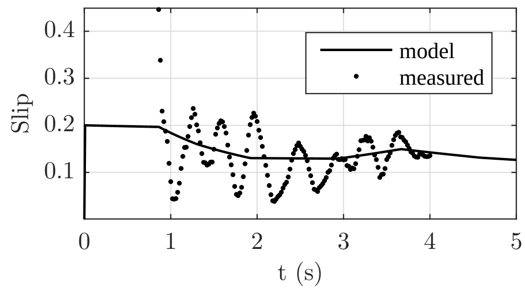

Figure 6.15: Slip during sand acceleration test.

ancy between measured and simulated results is the poor dynamic performance of the sonar based ground speed sensor at low speeds. The response time of the sensor is very long at low speeds. This accounts in particular for the large deviation between 0 and 1 second. Another factor is the lack of direct wheel speed measurement. The wheel speed is inferred from the respective motor speed accounting for the gear ratio. The transmission is a chain drive that suffers from a large back lash which could in conjunction with some slight torque ripple account for some of the deviation at higher speeds. Also, recall that the slip is defined as,

$$s = \frac{v_r - v_x}{v_x}, \tag{6.2}$$

making the slip very sensitive to small variations in ground speed at low speeds so that very accurate measurement of ground speed is required to measure slip. Instead of sonar based ground speed measurement perhaps image based motion sensing could be used or perhaps a position/speed measuring fifth wheel could used. In addition, direct wheel speed measurement would improve slip measurement. This could be accomplished with an encoder mounted on each wheel of the vehicle.

Figure 6.16 shows the simulated sinkage vs time for the vehicle. There was no discernible sinkage observed in the vehicle tracks so only the simulated result is shown. The predicted excavation sinkage is approximately 2 mm in depth. This is swamped

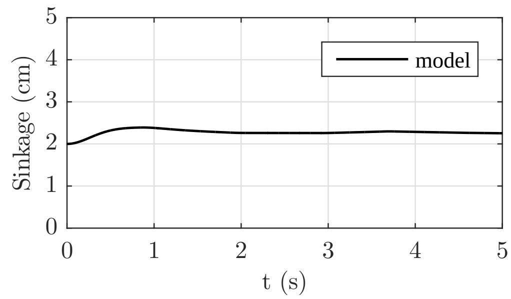

Figure 6.16: Sinkage during sand acceleration test.

by the large 2 cm static sinkage and the uncertainties of sinkage measurement on a loose sandy surface. Essentially the simulated results agree with what was observed in the test.

The vehicle model was further updated to produce the very good agreement between measured and simulated performance evident in Figure 6.14. The loose soil rolling resistance curve was updated to the curve shown in Figure 6.17a. The peak is slightly broader than before and more significantly the rise to the peak is more gradual. The drop off after the peak is also lower now. Figure 6.17b shows the new tractive force curve (friction component) used in the simulation. The peak friction component of tractive force is significantly higher and rises faster than before. The

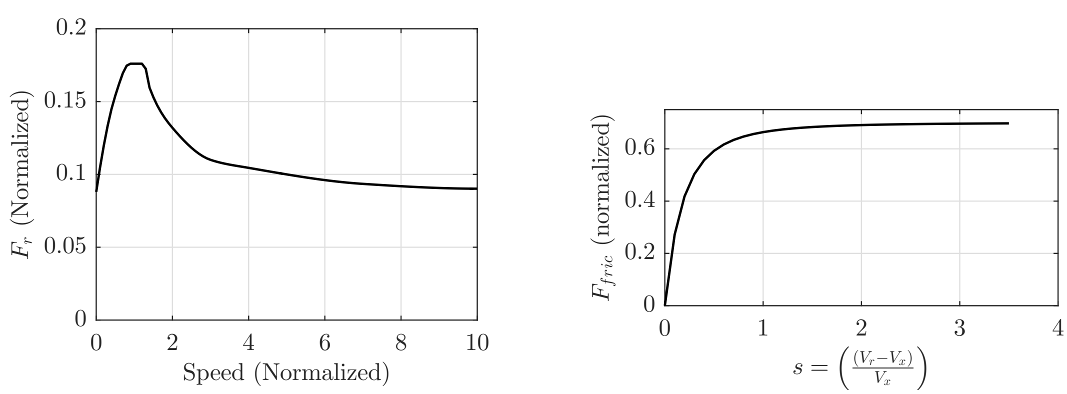

(a) Loose sand rolling resistance

(b) Off road friction component of tractive force

Figure 6.17: Vehicle model updates (offroad).

adjusted friction component of tractive force curve is further validated by results from Appendix E.

The acceleration of the vehicle is much slower than initially predicted in Section 4.7.2. This is due to the updated vehicle parameters and reduced total motor torque (see end of Section 6.3). The amount of slip and sinkage is much lower than initially predicted. This is again mostly attributable to the increased mass and loss of torque but is also significantly reduced due to the higher than expected traction in the loose sand of the arena.

The low level of slip attainable with the current vehicle configuration and the sand conditions in the horse arena prevented any significant traction testing from being carried out. The sinkage control algorithm that was developed could not be tested because of a complete lack of any significant slip. Figure 6.13 does show some significant wheel spin. This occurred only when the vehicle was cornering hard. In hard cornering the inside wheels are unloaded somewhat due to the action of the lateral acceleration on the vehicle centre of mass. In addition, the very significant slip evident in the figure occurred mainly because the inside wheels were further unloaded as they crossed a previously made rut in the sand.

Chapter 7

Contributions, Conclusions and Future Work

7.1 Contributions

To support the design of new high performance off-road electric vehicles a model of high performance off-road vehicle dynamics was developed. The model supports simulation of vehicle performance for demanding conditions such as loose sand and also supports simulation in less demanding conditions such as hardpacked clay. The model can be used to predict power requirements in varying off-road conditions and is thus an invaluable tool for the vehicle designer. The developed vehicle model was validated for both hardpack and loose soil conditions.

An off-road battery electric vehicle was designed and built to support the development of future off-road vehicles and in particular off-road vehicle drivetrains. The platform has a high performance drivetrain topology combined with comprehensive monitoring instrumentation and a flexible and powerful FPGA based vehicle control module. The vehicle drivetrain and instrumentation were successfully tested and validated.

A flexible well instrumented high-performance development vehicle can aid in the development of future off-road vehicles and off-road vehicle drivetrains. This platform provides a means to collect performance data that will allow verification of new models for off-road traction. The measured performance data will also provide insights that can form the basis of new research in the area of high performance off-road traction.

7.2 Conclusions

The vehicle model developed was successful in predicting performance in both hard-pack and loose soil conditions. With the updated model inputs, the predictions are accurate and very applicable to off-road vehicle design.

Overall the vehicle performs well both on and off-road. The performance however does not meet the original performance requirements. Despite the lower than expected performance, the vehicle proved capable of investigating both on and off-road driving providing insights into the performance issues of the vehicle itself.

The vehicle instrumentation provides an abundance of information for future investigations into off-road vehicle performance and for off-road vehicle development. The vehicle instrumentation worked well overall. The data gathered by the vehicle instrumentation allowed the vehicle performance to be characterized and assessed. However, accurate ground speed measurement proved to be more difficult than anticipated. The development of a sensor capable of dealing with high acceleration and rapidly varying surface texture should solve this problem.

7.3 Future Work

Some shortcomings in ground speed measurement and vehicle wheel speed measurement were noted. Improvements in these two measurements should be made in a future iteration of the vehicle to improve the accuracy of calculated wheel slip. Development of the wheel torque sensor should be continued and completed as a direct wheel torque measurement would greatly benefit any traction management scheme.

In its current configuration the vehicle lacks the torque to perform traction studies at high slip rates. Available wheel torque may be raised by redesign of the vehicle transmission (raising the gear ratio) or preferably by replacing the current motor with higher performance motors.

Figure 7.1: Field testing.

Bibliography

[1] International Energy Agency, "Global EV Outlook 2017," *IEA Publications*, pp. 1–71, 2017.

[2] T. Becker, I. Sidhu, and B. Tenderich, "Electric vehicles in the United States: a new model with forecasts to 2030," University of California, Berkeley, Tech. Rep., 2009.

[3] A. Hajihosseinlu, S. Filizadeh, G. Bistyak, and E. Dirks, "Electronic differential design for a vehicle with four independently controlled in-wheel motors," *2014 IEEE International Electric Vehicle Conference, IEVC 2014*, 2014.

[4] B. K. Sovacool, "Early modes of transport in the United States: Lessons for modern energy policymakers," *Policy and Society*, vol. 27, no. 4, pp. 411–427, 2009.

[5] S. Agostino, "The Electric Car," *IEEE Potential*, vol. 12, no. 1, pp. 28–32, 1993.

[6] J. Anderson and C. D. Anderson, *Electric and Hybrid Cars: A History*, 2nd ed. McFarland & Company, Inc., 2010.

[7] C. Sulzberger, "An early road warrior: electric vehicles in the early years of the automobile," *IEEE Power and Energy Magazine*, vol. 2, no. june, pp. 66–71, 2004.

[8] Natural Resources Canada, "Average Retail Prices for Regular Gasoline in 2018 (Canada)," 2018. [Online]. Available: http://www2.nrcan.gc.ca/eneene/sources/pripri/prices_bycity_e.cfm

[9] M. G. Bekker, "Evolution of approach to off road locomotion," *Journal of Terramechanics*, vol. 4, no. 1, p. 5, 1967.

[10] M. G. Bekker, *Theory of Land Locomotion.* Ann Arbor: The University of Michigan Press, 1956.

[11] Z. J. Janosi, "Performance Analysis of a Driven Non-deflecting Tire in Soil," U.S. Army Tank-automotive Center, Center Line, Tech. Rep., 1963.

[12] E. Hegedus, "Pressure Distribution and Slip-Sinkage Relationship under Driven Rigid Wheels," Warren, Michigan, 1962.

[13] A. R. Reece, “Problems of Soil Vehicle Mechanics,” U.S. Army Tank-automotive Center, Warren, Tech. Rep., 1964.

[14] J. Y. Wong and A. R. Reece, “Prediction of rigid wheel performance based on the analysis of soil-wheel stresses. Part II. Performance of towed rigid wheels,” *Journal of Terramechanics*, vol. 4, no. 2, pp. 7–25, 1967.

[15] D. Gee-Clough, “The Bekker theory of rolling resistance amended to take account of skid and deep sinkage,” *Journal of Terramechanics*, vol. 13, no. 2, pp. 87–105, 1976.

[16] A. L. Leonovich, P. N. Pavlov, V. V. Cromov, I. Y. Ilyin, V. A. Lozhkin, V. K. Mishkin, and P. N. Naumov, “The efficient evaluation of soil trafficability of planetary vehicles,” *Acta Astronautica*, vol. 5, no. 7-8, pp. 507–514, 1978.

[17] S. K. Upadhyaya, M. Sime, N. Raghuwanshi, and B. Adler, “Semi-empirical traction prediction equations based on relevant soil parameters,” *Journal of Terramechanics*, vol. 34, no. 3, pp. 141–154, 1997.

[18] S. K. Upadhyaya, D. Wulfsohn, and G. Jubbal, “Traction prediction equations for radial ply tyres,” *Journal of Terramechanics*, vol. 26, no. 2, pp. 149–175, 1989.

[19] C. Harnisch, “Drive Line Concepts for Multi-axle Off-road Vehicles - Simulation with ORIS,” in *7th European Conf. of the ISTVS*, 1997, p. 8.

[20] B. Coutermarsh, “Velocity effect of vehicle rolling resistance in sand,” *Journal of Terramechanics*, vol. 44, no. 4, pp. 275–291, 2007.

[21] T. J. W. Leland and E. G. Smith, “Aircraft Tire Behavior During High-speed Operations in Soil,” National Aeronautics and Space Administration, Washington, Tech. Rep., 1972.

[22] R. G. Pope, “The effect of wheel speed on rolling resistance,” *Journal of Terramechanics*, vol. 8, no. 1, pp. 51–58, 1971.

[23] D. H. Walling, “The Design of an Autonomous Vehicle Research Platform,” Ph.D. dissertation, Virginia Polytechnic Institute and State University, 2017.

[24] R. De Castro, R. E. Araújo, and H. Oliveira, “Control in multi-motor electric vehicle with a FPGA platform,” *Proceedings - 2009 IEEE International Symposium on Industrial Embedded Systems, SIES 2009*, pp. 219–227, 2009.

[25] S. Abourida, C. Dufour, and J. Bélanger, “Real-Time and Hardware-In-The-Loop Simulation of Electric Drives and Power Electronics : Process, problems and solutions,” *Simulation*, no. May 2014, pp. 1908–1913, 2005.

[26] R. Frevert, J. Haase, R. Jancke, U. Knochel, P. Schwarz, R. Kakerow, and M. Darianian, *Modeling and Simulation for RF System Design.* Springer Science and Business Media, 2005.

[27] C. Mi, M. A. Masrur, and D. W. Gao, *Hybrid Electric Vehicles: Principles and Applications with Practical Perspectives*, 1st ed. Chichester: John Wiley & Sons, Ltd., 2011.

[28] R. Rajamani, *Vehicle Dynamics and Control*, F. Ling, Ed. Troy, NY: Springer, 2006.

[29] M. Ehsani, Y. Gao, and A. Emadi, *Modern Electric Hybrid Electric and Fuel Cell Vehicles*. Boca Raton, FL: CRC Press, 2010.

[30] R. V. N. Melnik, N. Song, and P. Sandholdt, "Dynamics of Torque-Speed Profiles for Electric Vehicles and Nonlinear Models Based on Differential-Algebraic Equations," *Proceedings of the fourth international conference on dynamical systems and differential equations*, pp. 610–617, 2002.

[31] W. F. Milliken and D. L. Milliken, *Race Car Vehicle Dynamics*. Warrendale: SAE International, 1995.

[32] D. Halliday and R. Resnick, *Fundamentals of Physics*, 2nd ed. New York: John Wiley & Sons, Ltd., 1981.

[33] M. I. Lyasko, "How to calculate the effect of soil conditions on tractive performance," *Journal of Terramechanics*, vol. 47, no. 6, pp. 423–445, 2010.

[34] F. M. Zoz, "Predicting Tractor Field Performance (Updated)," *American Society of Agricultural Engineers*, vol. 33, no. 87, p. 16, 1987.

[35] J. A. Cabrera, J. J. Castillo, J. Pérez, J. M. Velasco, A. J. Guerra, and P. Hernández, "A procedure for determining tire-road friction characteristics using a modification of the magic formula based on experimental results," *Sensors (Switzerland)*, vol. 18, no. 3, 2018.

[36] T. D. Gillespie, *Fundamentals of Vehicle Dynamics*. SAE International, 1992.

[37] D. Holloway, W. Wilson, and T. Drach, "Examination of ATV Tire Forces Generated on Clay, Grass, and Sand Surfaces," in *Government/Industry Meeting and Exposition, Washington, DC*. SAE, 1989, p. 12.

[38] P. S. Maybeck, *Stochastic Models, Estimation, and Control*, ser. Mathematics in Science and Engineering. Elsevier Science, 1982.

[39] H. Sado, S. Sakai, and Y. Hori, "Road condition estimation for traction control in electric vehicle," in *IEEE International Symposium on Industrial Electronics*. Bled: IEEE, 1999, pp. 973–978.

[40] R. Vishwanathan, P. Weckler, J. Solie, and M. Stone, "Evaluation of ground speed sensing devices under varying ground surface conditions," *2005 ASAE Annual International Meeting*, 2005.

[41] D. Titterton and J. Weston, *Strapdown inertial navigation technology.* London: Peter Peregrinus Ltd., 1997.

[42] F. Mas, Q. Zhang, and A. C. Hansen, *Mechatronics and Intelligent Systems for Off-road Vehicles.* London: Springer Verlag, 2010.

[43] J. Wang, Q. Wang, L. Jin, and C. Song, "Independent wheel torque control of 4WD electric vehicle for differential drive assisted steering," *Mechatronics*, vol. 21, no. 1, pp. 63–76, 2011.

[44] T. Bohn, M. Duoba, and R. Carlson, "In-Situ Torque Measurements in Hybrid Electric Vehicle Powertrains," in *Electric Vehicle Symposium*, Anaheim, 2007.

[45] X. Jun-Qiang, X. Guang-Ming, and Z. Yan, "Application of automatic manual transmission technology in pure electric bus," *2008 IEEE Vehicle Power and Propulsion Conference, VPPC 2008*, pp. 5–8, 2008.

[46] J. W. Schultz and S. Huard, "Comparing AC Induction with Permanent Magnet motors in hybrid vehicles and the impact on the value proposition," Parker Hannifin–EMN Division–Automation Group, Rohnert Park, CA, Tech. Rep., 2015.

[47] J. Larminie and J. Lowry, *Electric Vehicle Technology Explained.* Chichester: John Wiley & Sons, Ltd., 2003.

[48] R. Bosch, "BOSCH CAN Specification," pp. 1–73, 1991.

[49] D. M. Gaston, "Selection of Wires and Circuit Protective Devices for STS Orbiter Vehicle Payload Electrical Circuits," NASA Lyndon B. Johnson Space Center, Houston, Tech. Rep., 1991.

[50] W. Kester, "High Speed Design Techniques," Analog Devices, Tech. Rep., 1996.

[51] R. Cohea, P. Davis, J. Jeter, D. Kimbrough, P. Najafi, P. Nelson, W. Pickens, and M. Vea, "BNR Richardson Hardware Design Guide," Bell Northern Research, Richardson, Tech. Rep., 1998.

[52] W. Kester, *Mixed-signal and DSP Design Techniques.* Analog Devices, 2000.

[53] M. I. Montrose, *Printed Circuit Board Design Techniques for EMC Compliance: A Handbook for Designers*, ser. IEEE Press Series on Electronics Technology. Wiley, 2000.

[54] H. W. Johnson and M. Graham, *High-speed Digital Design: A Handbook of Black Magic.* Prentice Hall, 1993.

[55] J. Sanchez and M. P. Canton, *Embedded Systems Circuits and Programming.* Boca Raton, FL: CRC Press, 2012.

[56] J. J. Labrosse, *MicroC/OS-II: The Real Time Kernel*, ser. Meets requirements for safety-critical systems. Taylor & Francis, 2002.

[57] J. Füzer, Z. Birčáková, A. Zeleňáková, P. Hrubovčák, P. Kollár, M. Predmerský, and J. Huňady, "Investigation of total losses of non-oriented electrical steels," *Acta Physica Polonica A*, vol. 118, no. 5, pp. 1018–1019, 2010.

[58] J. E. Vrancik, "Prediction of Windage Power Loss in Alternators," National Aeronautics and Space Administration, Washington, DC, Tech. Rep. October, 1968.

Appendices

Appendix A

Motor Constants

A.1 Rear Motors

In order to measure motor torque, the apparatus shown in Figure A.1 was constructed. It consists of a constant radius lever arm and an electronic scale. The torque at the wheel is simply the product of the lever arm length and the force reading from the scale.

Figure A.1: Motor torque calibration setup.

The results of the measurements are shown in Figure A.2. Motor torque equals wheel torque divided by the transmission gear ratio (5:1). A straight line with zero offset was fit to the data. The slope of the fit line is equal to 0.126 which is the torque constant for the rear motors (Eq. A.5), that is,

$$K_T = 0.126 \left(\frac{\text{Nm}}{\text{A}}\right). \tag{A.1}$$

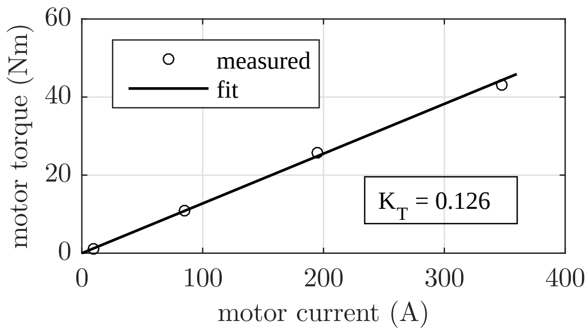

Figure A.2: Motor torque calibration.

The torque constant for a PMAC motor my also be calculated from the voltage constant of the motor. The electrical power for the motor,

$$P = \sqrt{3} V_{ll} I_l = V_{ll} I_{eff}. \tag{A.2}$$

The effective current ($I_{eff} = \sqrt{3} I_l$) is typically used when dealing with PMAC motors and in fact this is the current value reported by the motor drives used in the vehicle. The electrical power is equated to the mechanical power giving,

$$V_{ll} I_{eff} = \omega T = \frac{2\pi N}{60} T, \tag{A.3}$$

where N is the motor speed in rpm and V_{ll} is the line to line RMS motor voltage. This may be rewritten as,

$$K_T = \frac{60}{2\pi} K_e, \tag{A.4}$$

where,

$$K_T = \frac{T}{I_{eff}}, \tag{A.5}$$

and,

$$K_e = \frac{V_{ll}}{N}. \tag{A.6}$$

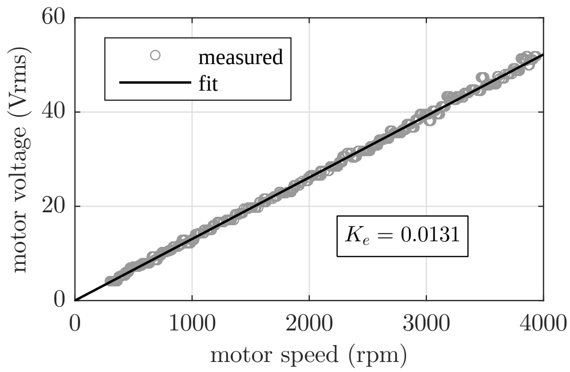

Figure A.3: Voltage constant rear motor.

It is important to note that V_{ll} must be measured when the motor terminals are open circuit. Figure A.3 shows the measured motor voltage vs motor speed. These measurements are taken from an actual vehicle data log. The data is taken from a period in which the vehicle is coasting down from a high speed. The slope of the fit line is equal to 0.0131 which is the voltage constant for the rear motors (Eq. A.6). Therefore, using Eq. A.4,

$$K_T = 0.125 \ \left(\frac{\text{Nm}}{\text{A}}\right). \tag{A.7}$$

The final value of is the average of these two values rounded to three digits,

$$K_T^{rear} = 0.126 \ \left(\frac{\text{Nm}}{\text{A}}\right). \tag{A.8}$$

A.2 Front Motors

The torque constant for the front motors is based solely on the voltage constant measurement. It was not possible to accurately measure the front wheel torque due to movement of the front wheel. As for the rear motors, the motor voltage and speed

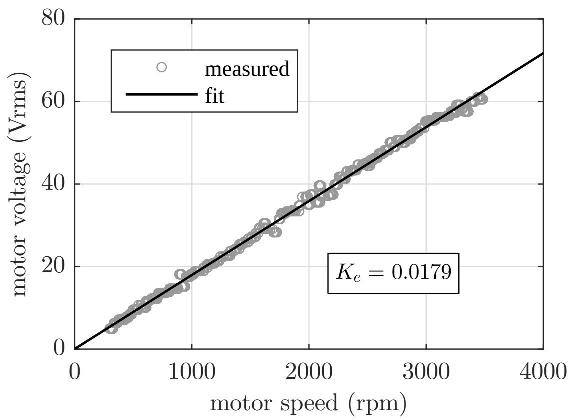

Figure A.4: Voltage constant front motor.

are taken from the vehicle data log. Figure A.4 shows the measured motor voltage vs motor speed. Therefore, from Eq. A.4,

$$K_T^{front} = 0.171 \left(\frac{\text{Nm}}{\text{A}}\right). \tag{A.9}$$

Appendix B

Motor Current Map Deviations

An important part of the configuration of the vehicle motor drives is setting the current map for the front and rear motors. The current map for each of the motors was provided by the motor manufacturers. The current map determines the maximum current that can be sent to the motor at any given motor speed. It is approximately a maximum torque vs speed map if scaled by K_T. The vehicle throttle position is mapped to a motor current command via the current map so that the vehicle throttle is essentially commanding motor torque.

B.1 Front Motors

Figures B.1 and B.2 show a significant droop in the commanded motor current (at 100% throttle) starting after 500 (rpm). In Figure B.1 the current drops to about 200 (A) and comes back up to the set current map at around 800 (rpm). In Figure B.2 the current drops to about 170 (A) and comes back up to the set current map at around 1200 (rpm). The depth and duration of the current droop is dependent on the vehicle loading.

The dynamometer used for the testing is a full size vehicle dynamometer. The inertia of the dynamometer rotating drum simulates the mass of a typical street car

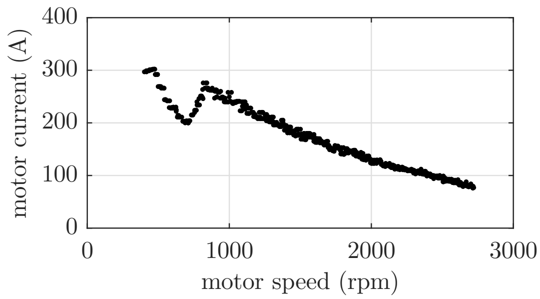

Figure B.1: Front motor current droop (dyno run).

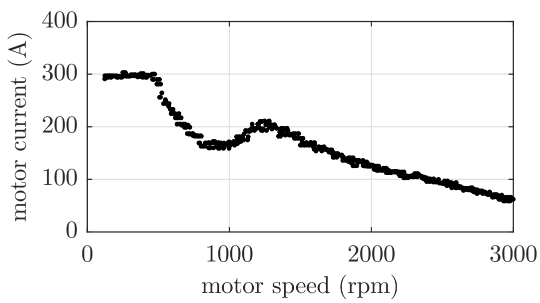

Figure B.2: Front motor current droop (hard pack).

about 1800 (kg). The acceleration of the drum will be much slower than the acceleration of the vehicle. At or around 500 (rpm) the motor drive throttles back the motor current probably due to an over current condition. After a set time the current is again examined and found to be back within limits. At this time the motor drive starts to follow the current map again.

Numerous thorough examinations of the motor drive settings for the front motor drives revealed no settings that might cause this behaviour. There are hundreds of parameters that control the behaviour of the motor drive. It is possible that there is some interaction between some of the settings that is not understood.

Because the current droop could not be eliminated, the current map for the front motor drives was compensated to account for the current droop. The compensation is based upon the droop shown in Figure B.2 obtained during a test drive on hardpack. This is a conservative estimate of the actual current map. The droop is slightly less for loose soil conditions because the acceleration is slightly lower. Figure B.3 shows the current map overlaid on the measured motor current (solid line). The current map used in the vehicle modelling and simulation is modified to approximately follow the current droop along the dashed line.

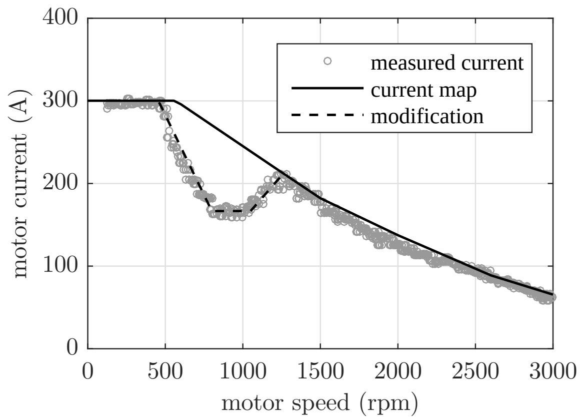

Figure B.3: Rear motor altered current map.

B.2 Rear Motors

Figure B.4 shows measured commanded current vs motor speed (at 100% throttle). Instead of being constant from 0 to 3040 (rpm), it starts higher than it should and drops off to the set value at 3040 (rpm). The current map used in the vehicle modelling

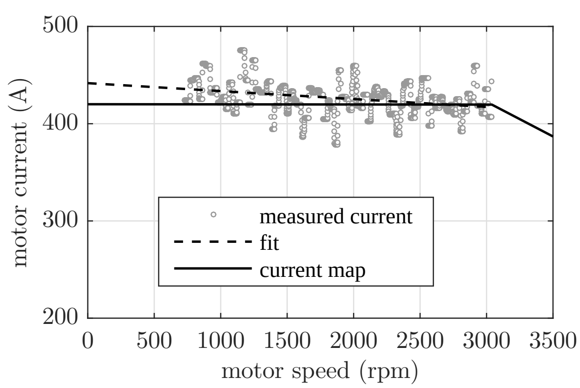

Figure B.4: Rear motor current slope.

and simulation is modified to use the dashed fit line from 0 to 3000 (rpm). The equation for the linear fit is: $I_{\text{motor}} = -0.00465N + 434.1$.

Appendix C

Dynamometer Calibration

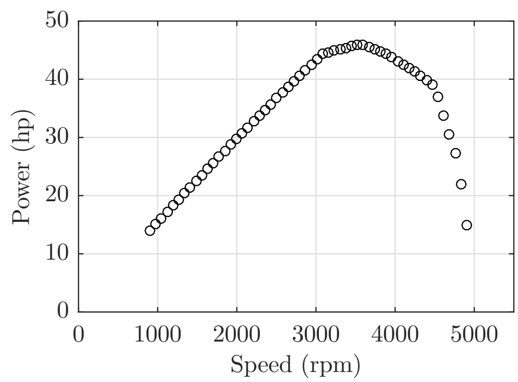

Figure C.1: Total horsepower (rear motors).

The measured horsepower vs motor speed for the two rear motors of the vehicle is plotted in Figure C.1. The measurements were taken at Speed Factor Racing (Winnipeg, MB). The corresponding torque vs motor speed curve is plotted in Figure C.2

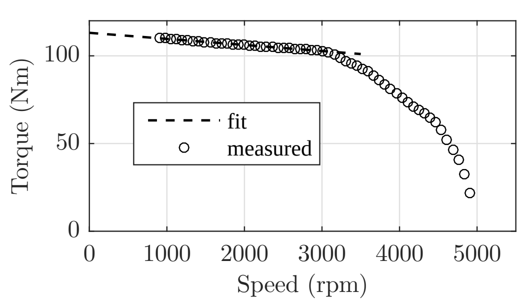

Figure C.2: Total torque (rear motors).

(measured data points). The dashed line is a linear fit to the measured torque for motor speed less than 3000 rpm. The y intercept of this line is 113 Nm. The calculated total stall torque for the rear motors, using results from Sections A and B, is,

$$109\ (\mathrm{Nm}) = 2 \cdot 434\ (\mathrm{A}) \cdot 0.126\ (\mathrm{Nm/A}). \tag{C.1}$$

Therefore the dynamometer torque measurements are scaled by a factor of,

$$0.965 = \frac{109}{113}. \tag{C.2}$$

Appendix D

Motor Torque Profiles

The motor current profiles from Section B are scaled by the motor torque constants to give motor torque vs speed. The resulting torque curves are shown in Figures D.1 and D.2. Note that the torque shown is for two motors. In Figure D.1 there is good

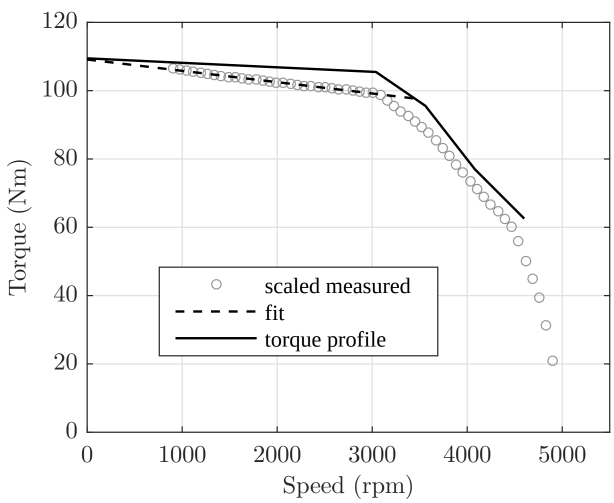

Figure D.1: Total torque (rear motors).

agreement between the measured torque vs speed and the torque curve at 0 rpm. This is as expected because of the dynamometer calibration. At other speeds there is a discrepency that grows with increasing motor speed. This discrepency is also apparent for the front motors in Figure D.2. There must be some speed dependent

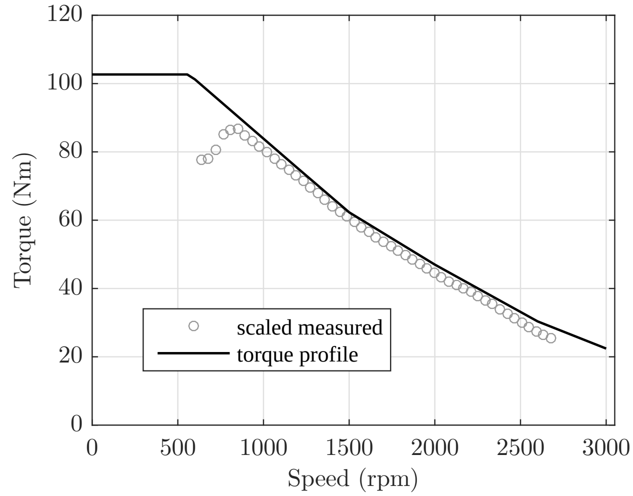

Figure D.2: Total torque (front motors).

effect that is reducing the torque.

In fact all electric motors suffer power losses due hysteresis, eddy current and anomalous losses [57]. An emperical equation for the electrical losses may be written as

$$P_{loss} = C_0 f + C_1 f^{\frac{3}{2}} + C_2 f^2, \tag{D.1}$$

where C_0, C_1 and C_2 are constant for a given flux density and f is the frequency of the motor current. The three terms in the equation correspond to the hysteresis, anomalous and eddy current losses respectively. For losses at maximum motor output torque it is reasonable to assume a constant flux density in the motor. Therefore, the torque losses can be written,

$$T_{loss} = D_1 f^{\frac{1}{2}} + D_2 f, \tag{D.2}$$

where D_1 and D_2 are assumed constant. The hysteresis term is dropped because it is constant and has already been accounted for in the calibration proceedure. Another significant power loss in electric motors is the loss due to windage [58]. Windage power loss is proportional to motor speed cubed. Therefore,

$$T_{loss} = D_3 f^2, \tag{D.3}$$

where D_3 is assumed to be constant. The total torque losses are then,

$$T_{loss}^{tot} = D_1 f^{\frac{1}{2}} + D_2 f + D_3 f^2. \tag{D.4}$$

The motor torque profiles are adjusted by T_{loss}^{tot} to give the final torque profiles which are shown plotted in Figures 6.7 and 6.8. The good match between the torque profiles and the measured torque values was achieved by finding appropriate values for the three loss constants. The values selected for the loss constants result in 1% anomalous losses and 3% eddy current losses at 3000 rpm for both the front and rear motors. The front and rear motors suffer 2% windage loss at 2000 and 3000 rpm respectively.

Appendix E

Traction–Sinkage Measurement

(a) Torque measurement setup

(b) Wheel sinkage in wet sand

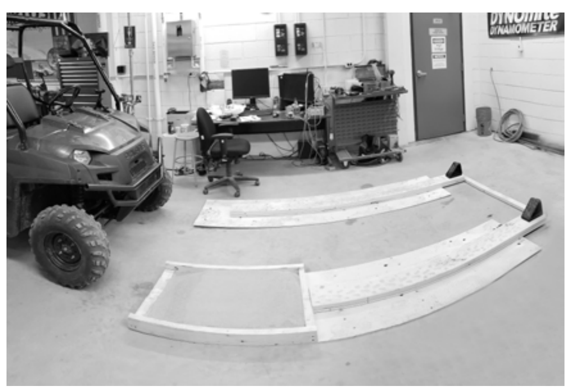

(c) Traction test bed

Figure E.1: Measuring torque vs sinkage.

Due to the higher than expected vehicle weight and the lower than expected total torque, the vehicle performance does not meet the original expected performance.

The vehicle as it stands simply does not have enough torque to produce significant slip in loose soil conditions. After field testing in loose soil conditions, it also became apparent that sand can have a higher friction coefficient than was originally anticipated (particularly for wet sand). In order to verify this conjecture, the test set up shown in Figure E.1 was constructed. The sand used to fill the sandbox approximates the sand found at the Cloud Nine indoor riding facility. A small sample of sand was brought back from the arena. Sand with a similar grain size distribution was locally purchased. The moisture content was adjusted to 7% (matching the arena sample).

The platform and sandbox shown in Figure E.1c were built to keep the vehicle level during testing and keep the loading on the wheels realistic. Figure E.1a shows the torque measurement apparatus. It consists of a weigh scale, pulley system and constant radius lever attached to the wheel. The pulley system is anchored to the vehicle rollcage.

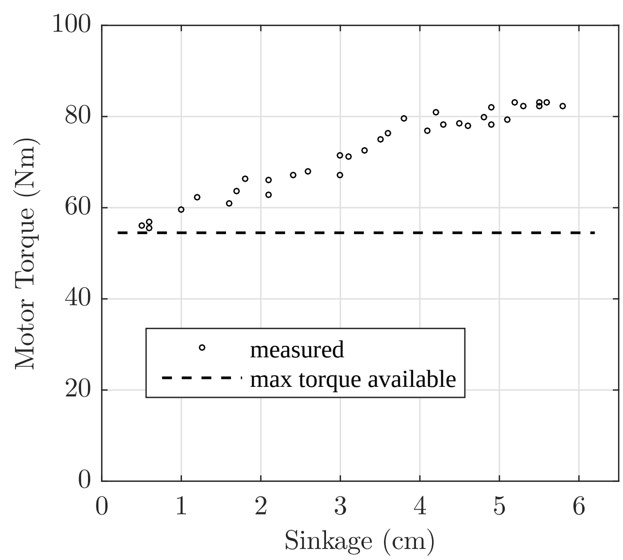

Figure E.2: Motor torque vs sinkage.

The test was performed by pulling the rope which would move the torque lever and thus turn the wheel. The wheel was rotated small fractions of a revolution until the wheel sinkage changed appreciably. During the rotation of the wheel the scale reading was monitored. The value just before cessation of movement was recorded along with wheel centre to sand distance. The results of the experiment are shown in Figure E.2. The lowest value of torque recorded at the onset of sinkage is already just at the absolute highest torque available from the rear motors which have a higher torque output than the front motors. This agrees with what was observed in the field very small slip with very low sinkage. Also interesting to observe is the significant rise in required torque for only moderate sinkage.

Practically speaking, the currently available torque would need to almost double to reliably break the wheel free and allow high levels of slip. This could be accomplished by replacing the transmissions with a 10:1 ratio transmission or replacing the motors with higher torque motors. Both of these options would reduce the top speed of the vehicle.

Appendix F

Example Data Log

The VDDS running on a PC produces the data log files. The data log files are comma separated value (CSV) formatted files. This format is easily imported into many programs for analysis. A program was written in Matlab script to graph all of the data in a given data log. An example output from the Matlab script is shown on the following pages.

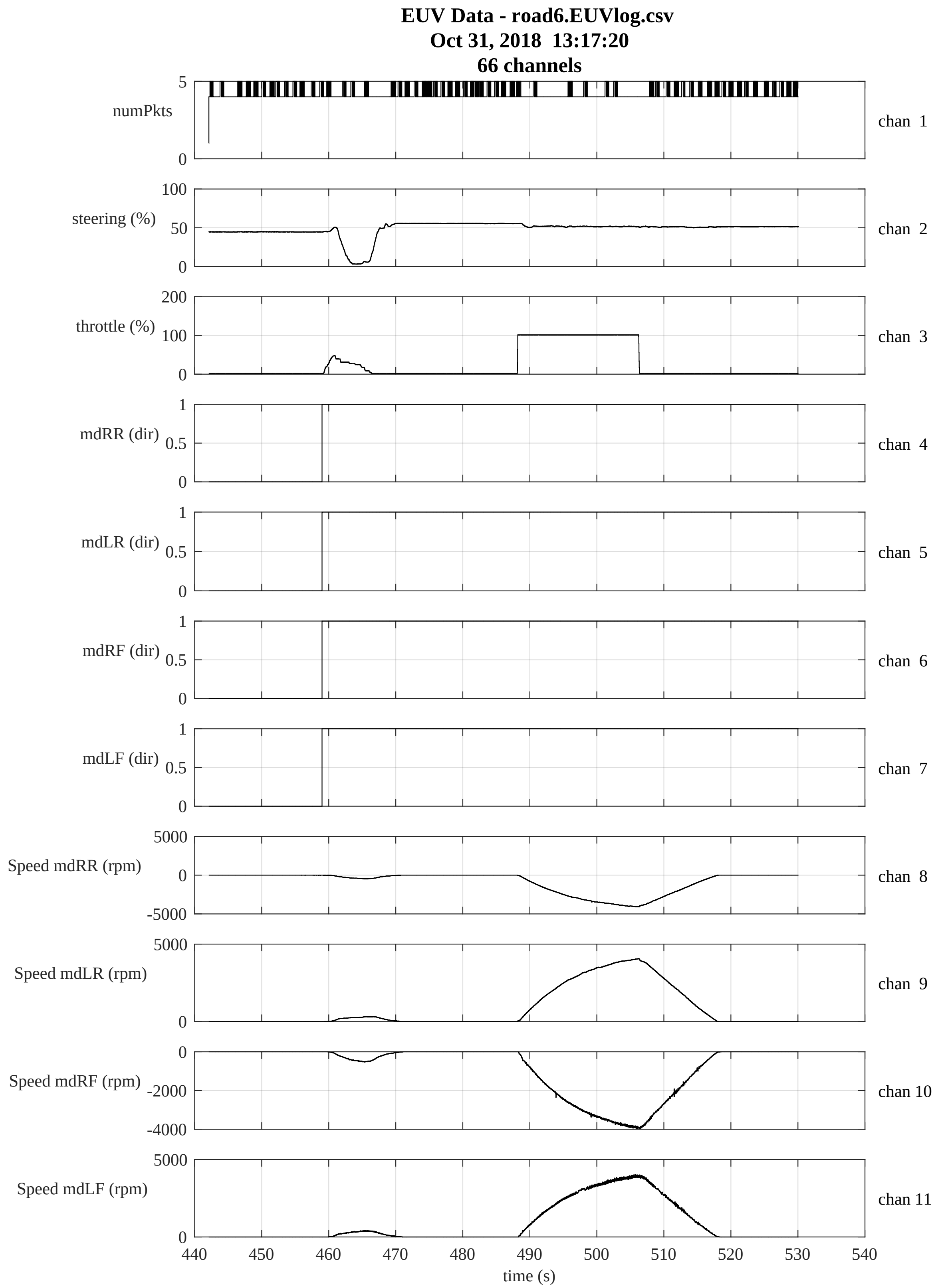

Figure F.1: Example Data Log (channel 1–11).

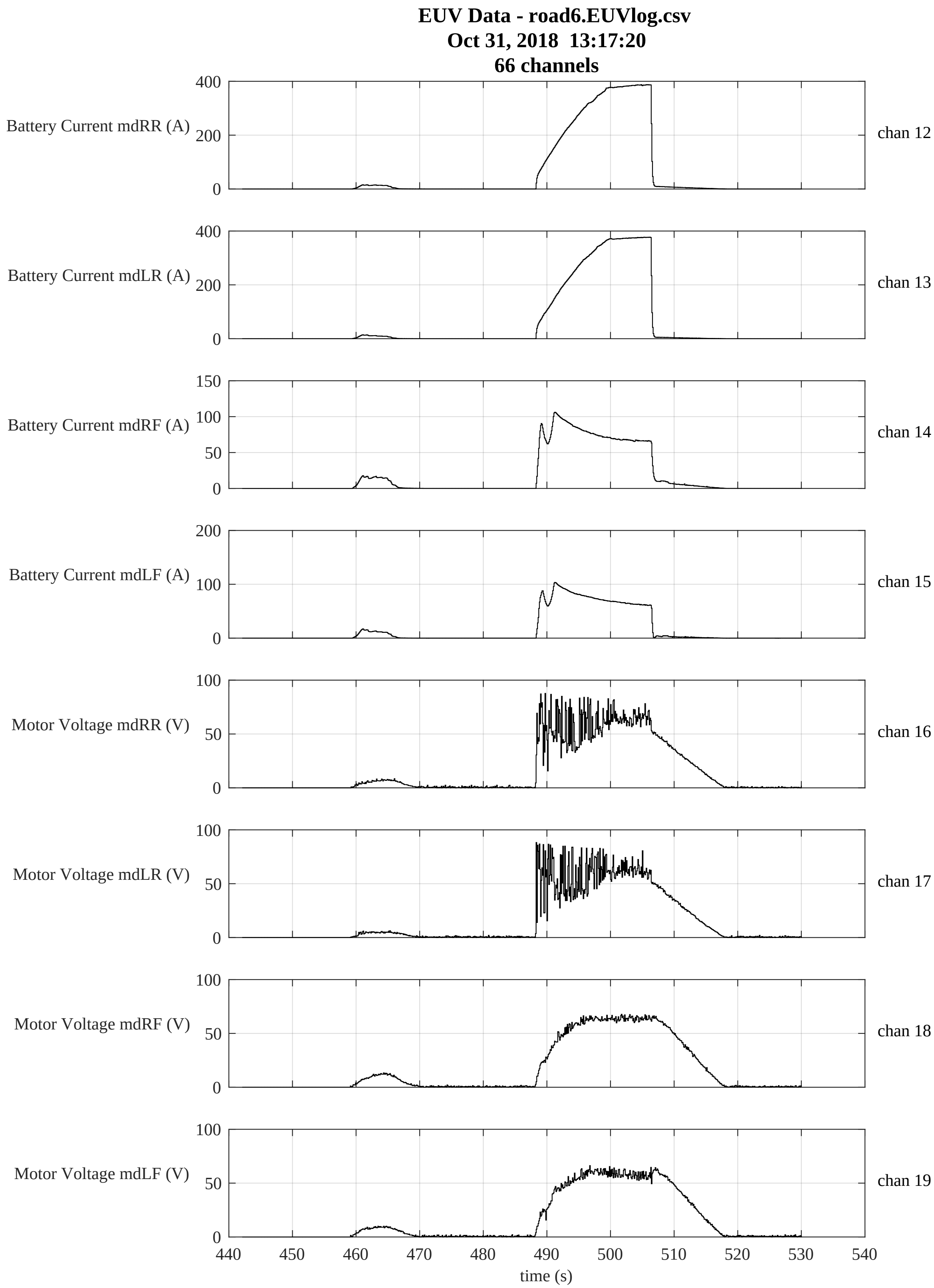

Figure F.2: Example Data Log (channel 12–19).

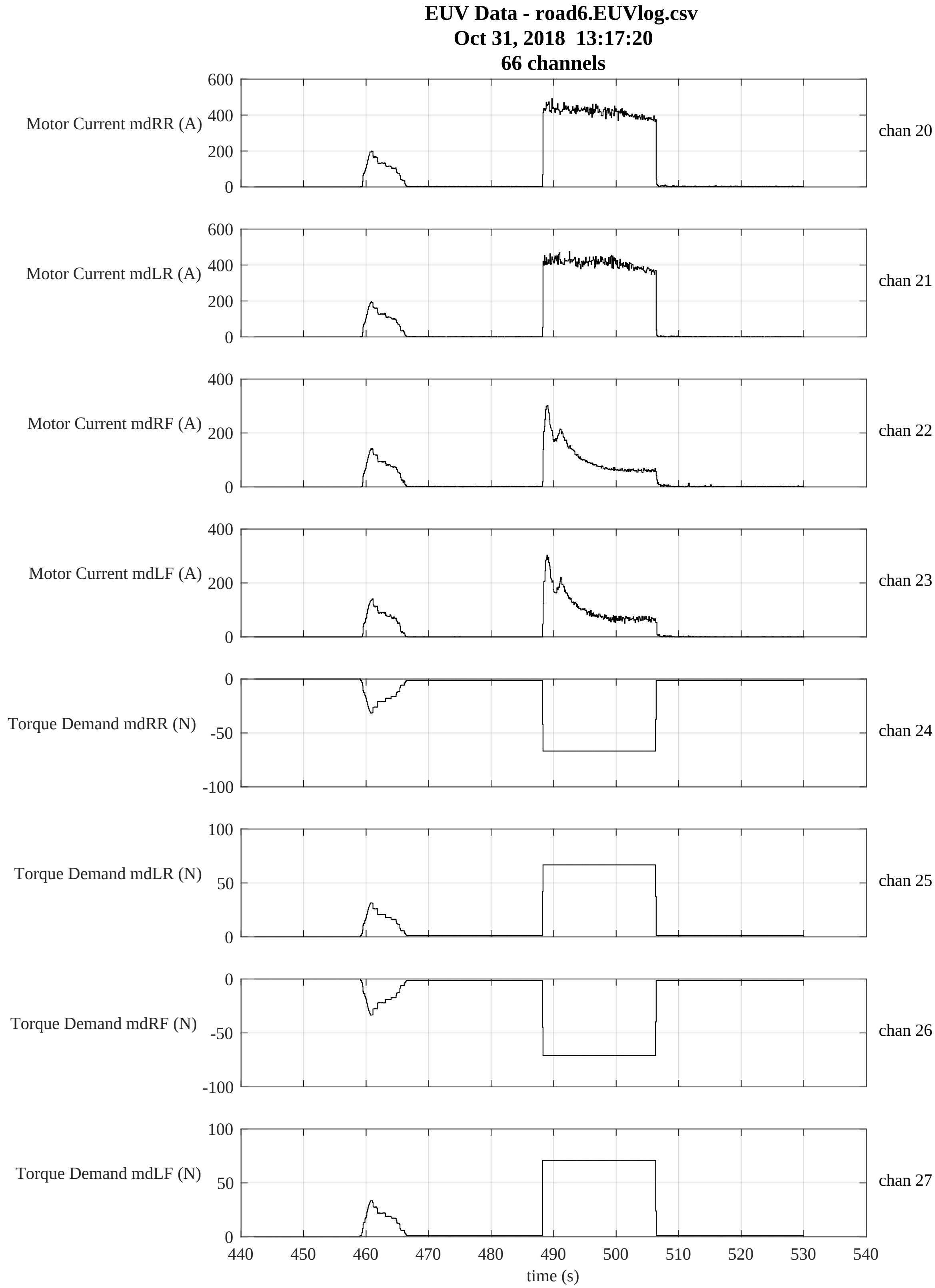

Figure F.3: Example Data Log (channel 20–27).

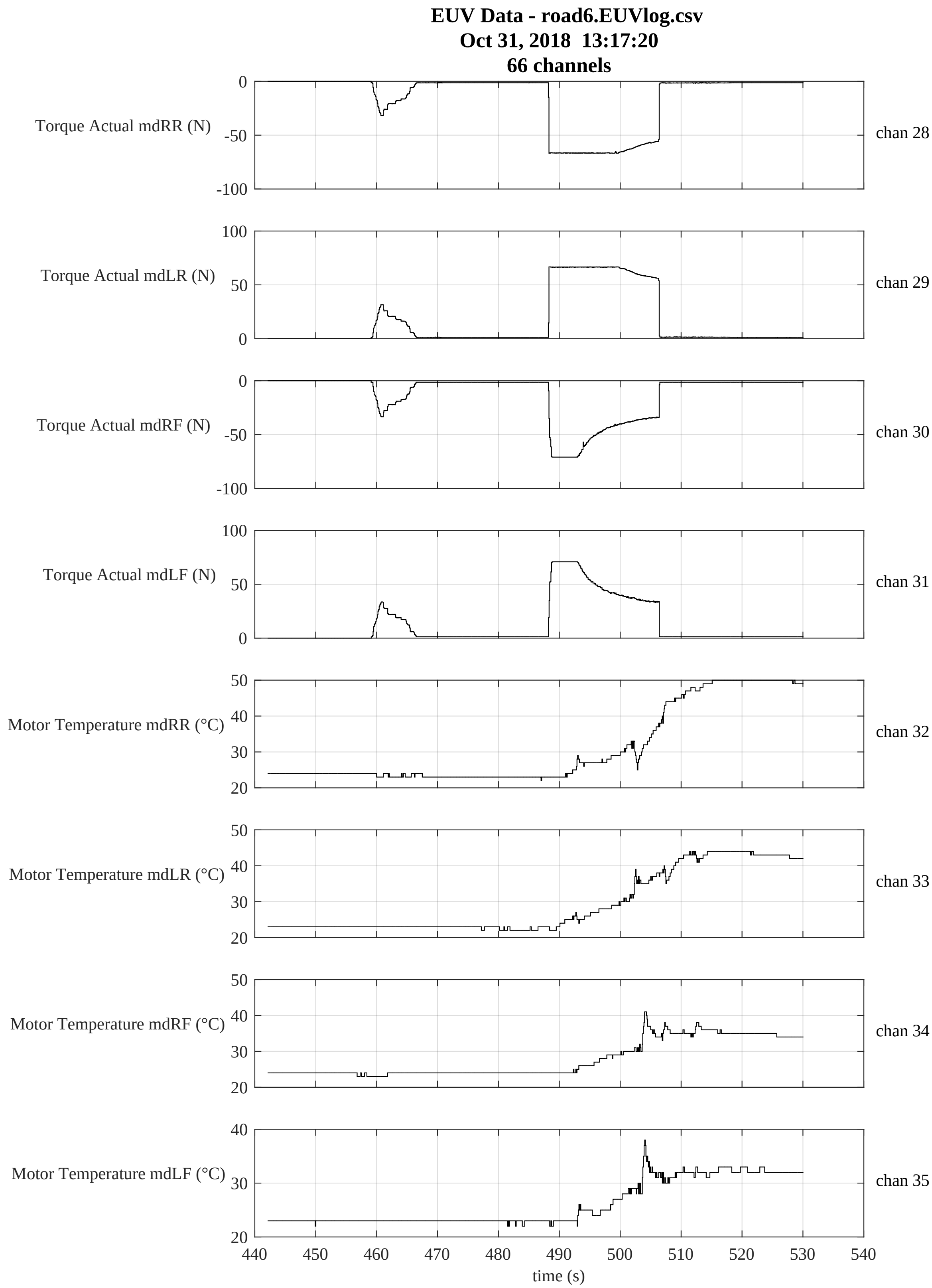

Figure F.4: Example Data Log (channel 28–35).

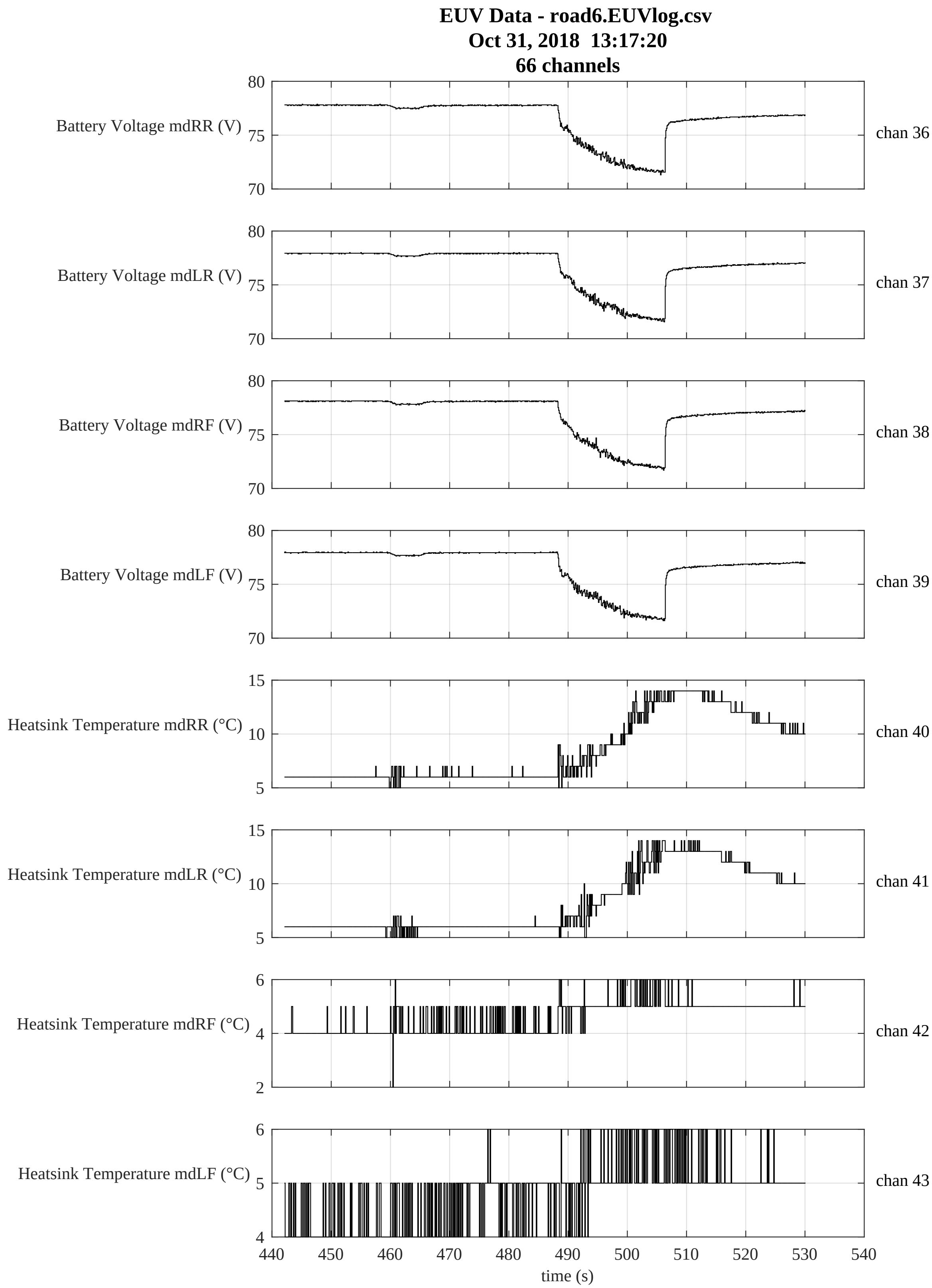

Figure F.5: Example Data Log (channel 36–43).

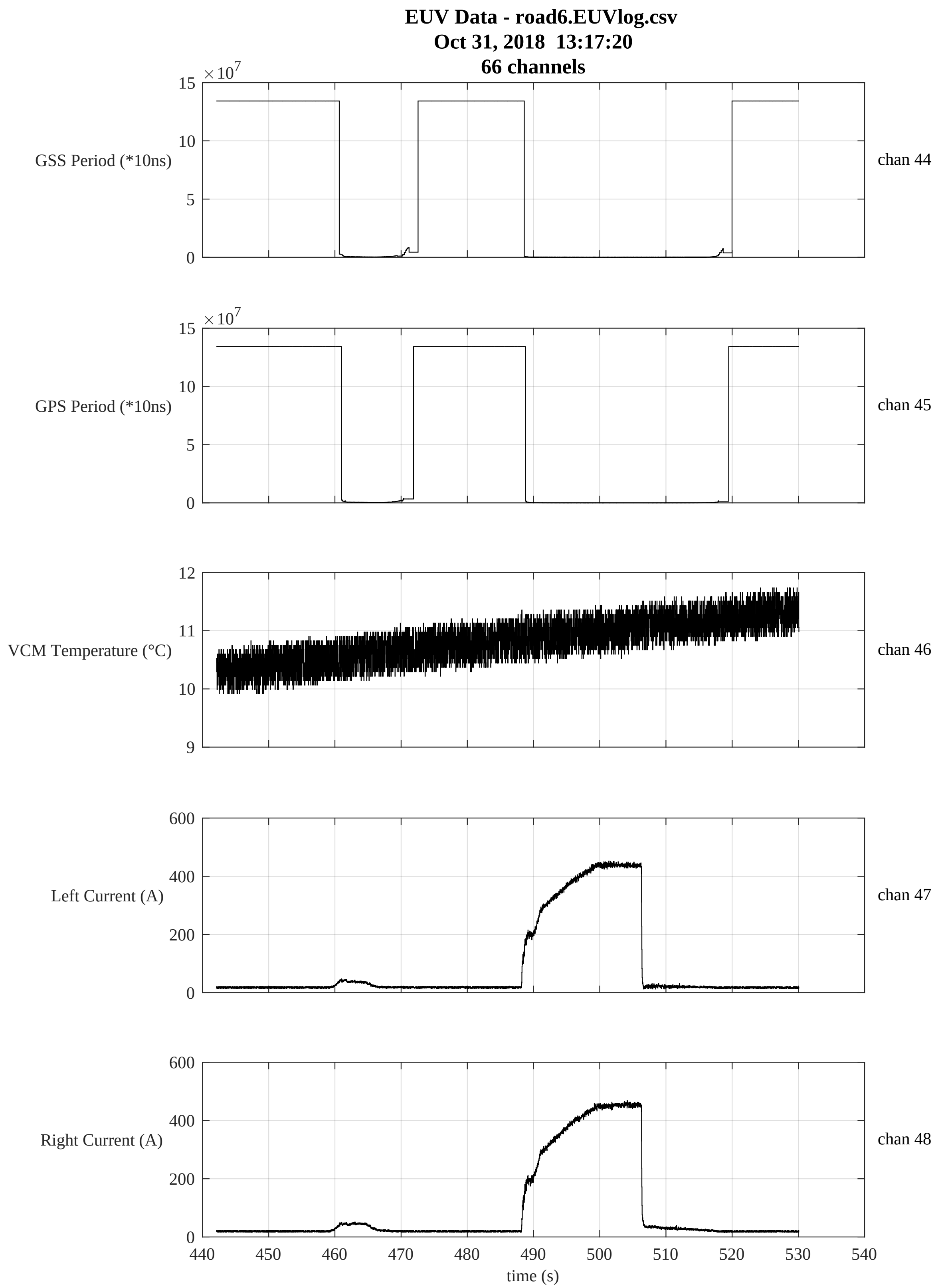

Figure F.6: Example Data Log (channel 44–48).

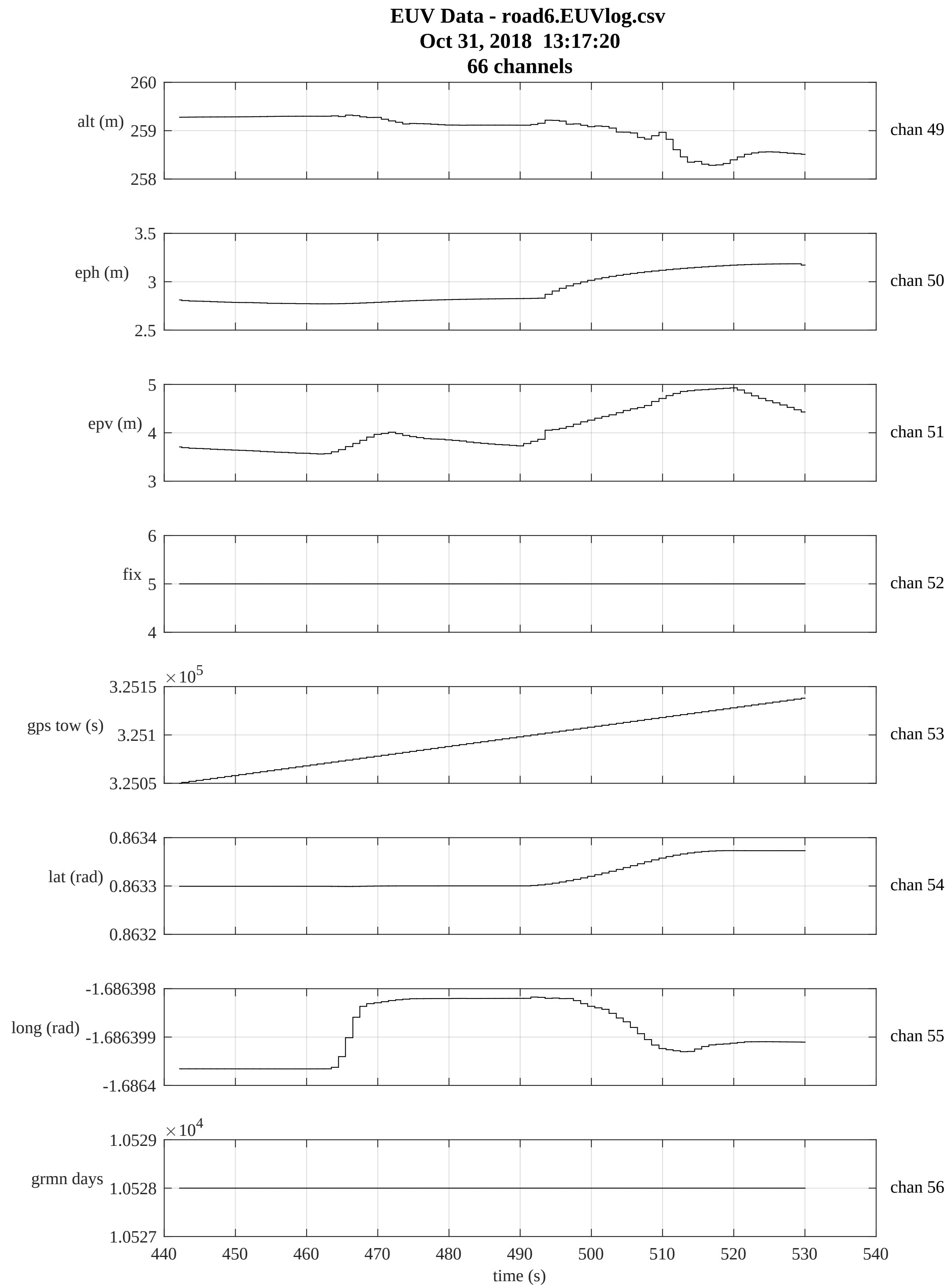

Figure F.7: Example Data Log (channel 49–56).

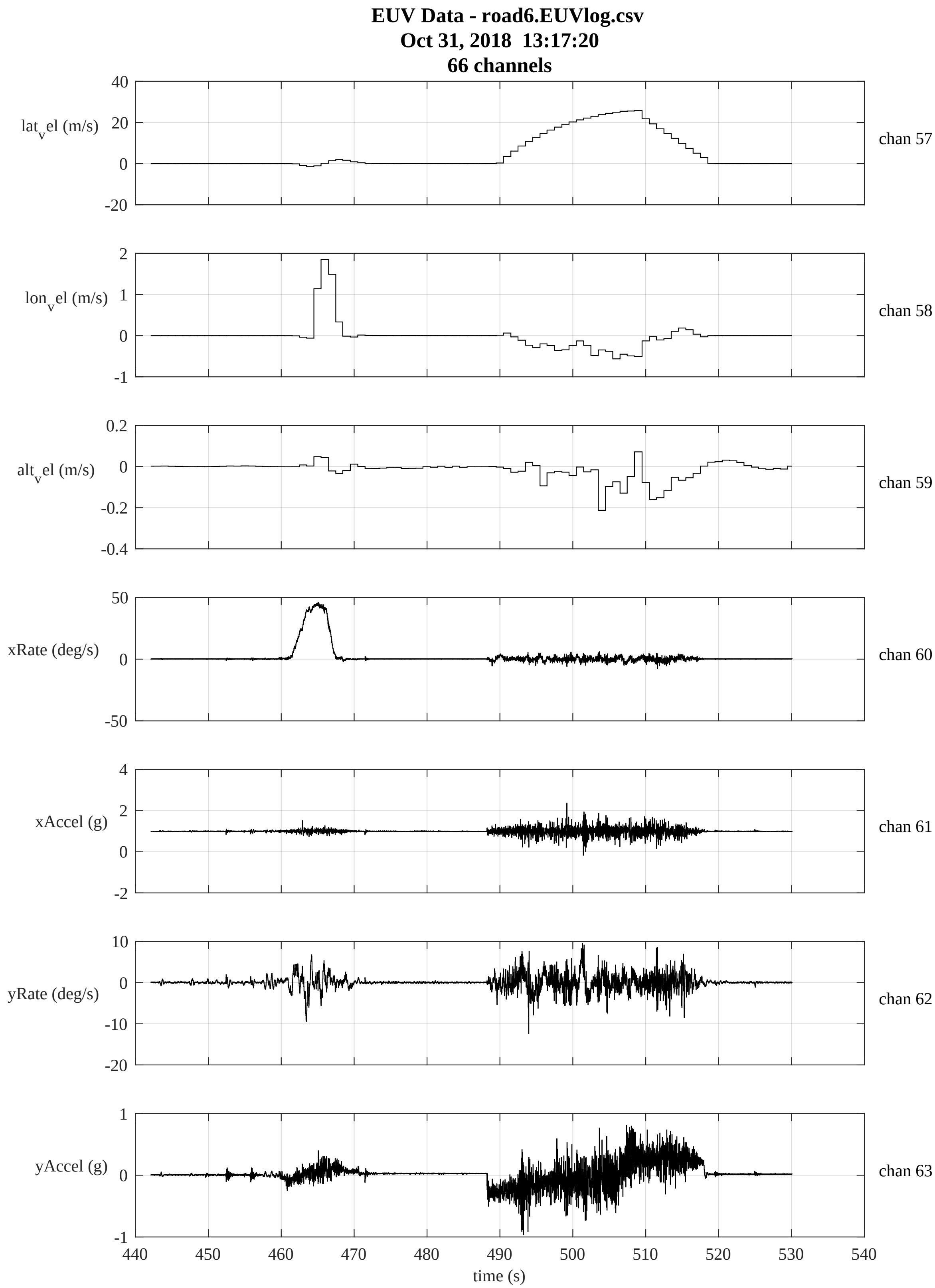

Figure F.8: Example Data Log (channel 57–63).

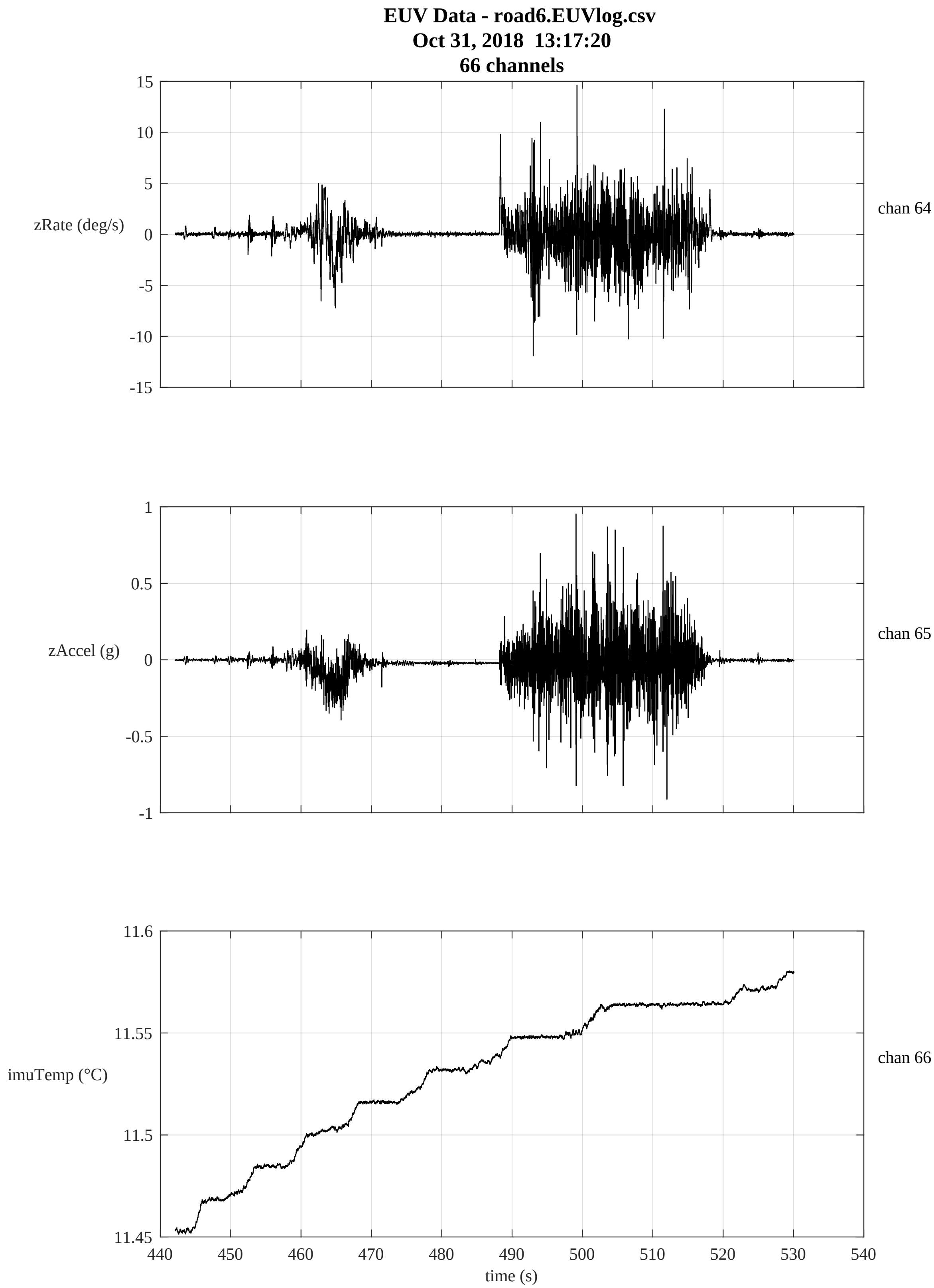

Figure F.9: Example Data Log (channel 64–66).

Appendix G

Printed Circuit Boards

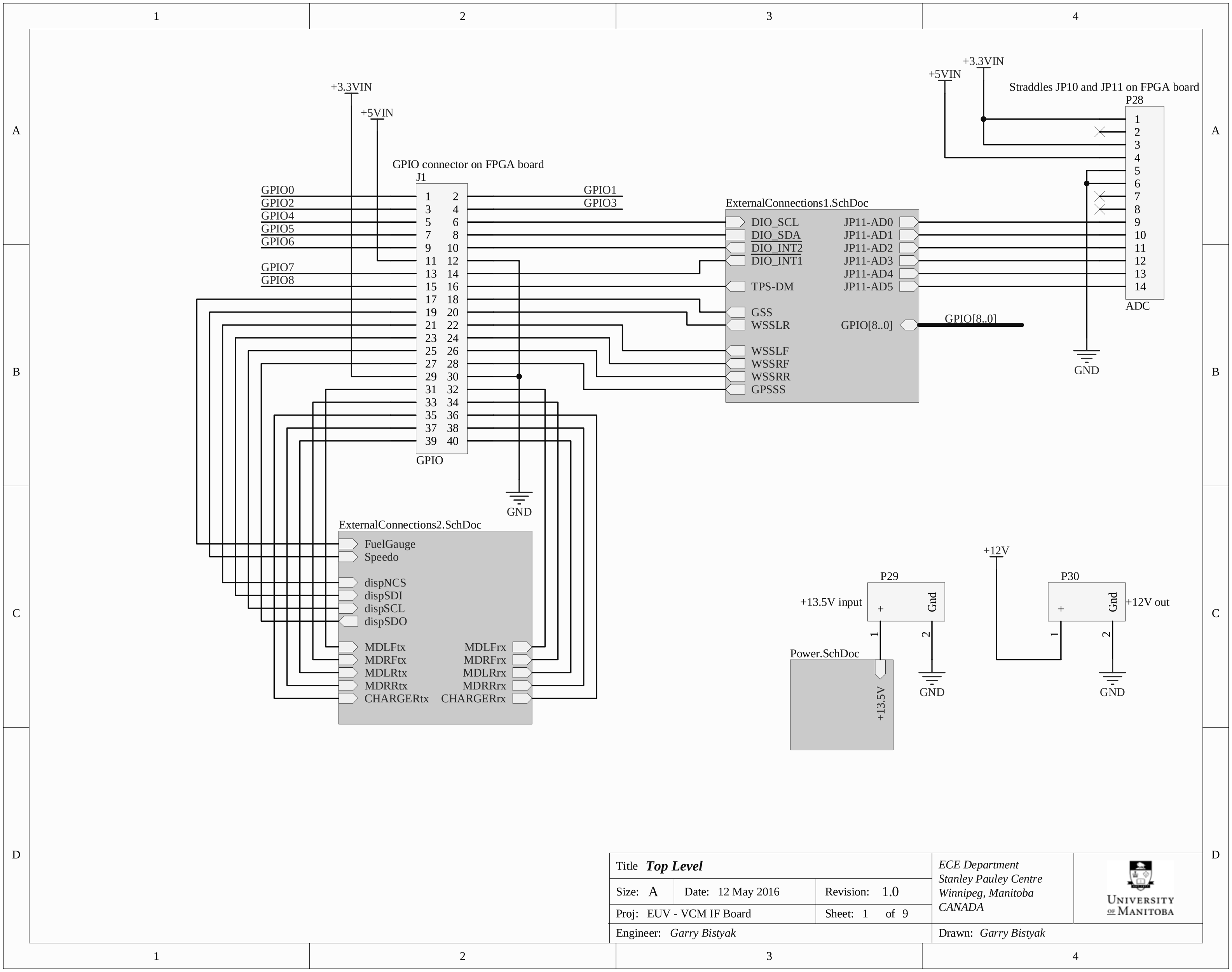

Figure G.1: Interface board schematic top level.

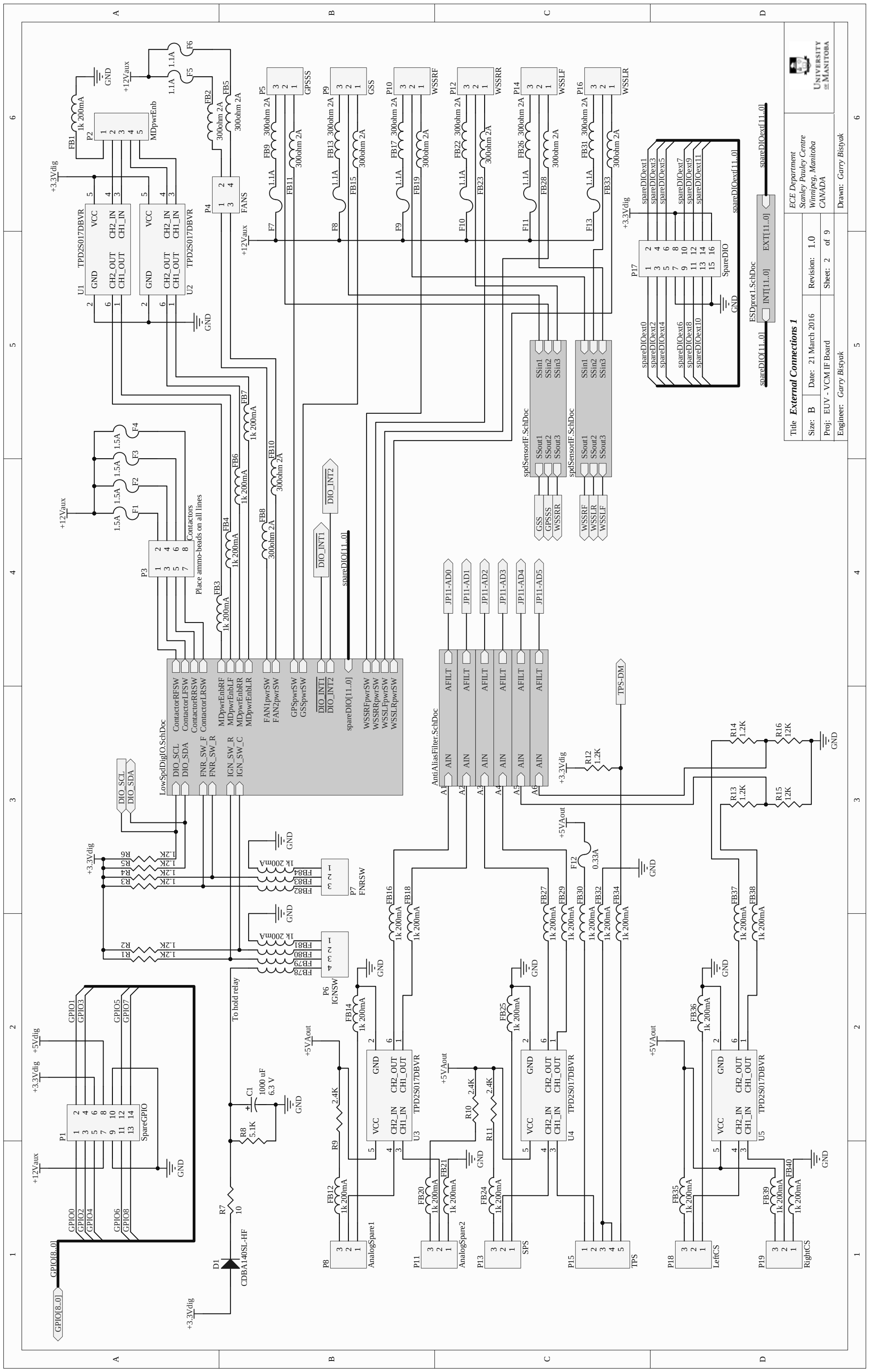

Figure G.2: Interface board schematic external connections 1.

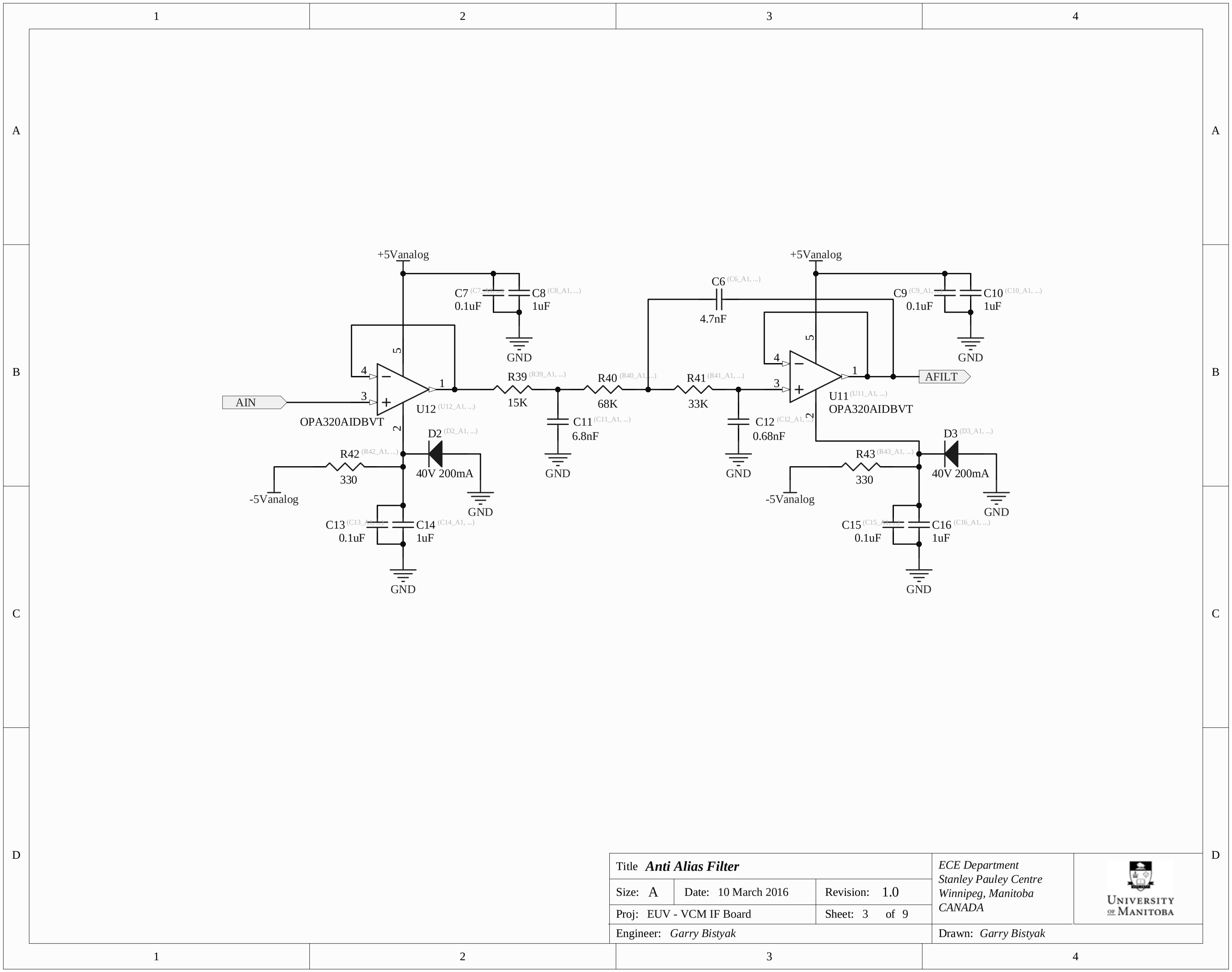

Figure G.3: Interface board schematic anti-alias filter.

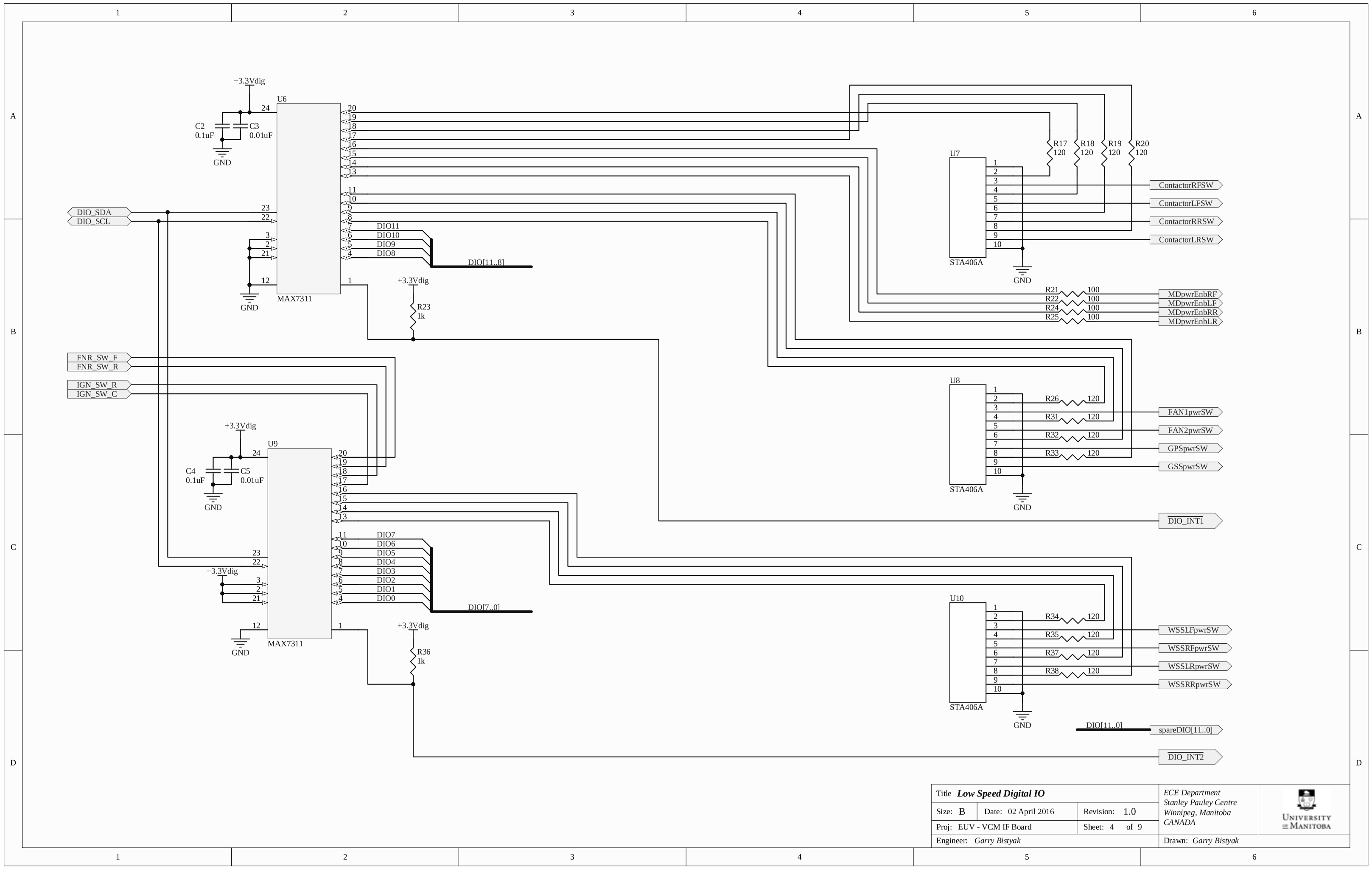

Figure G.4: Interface board schematic low speed digital I/O.

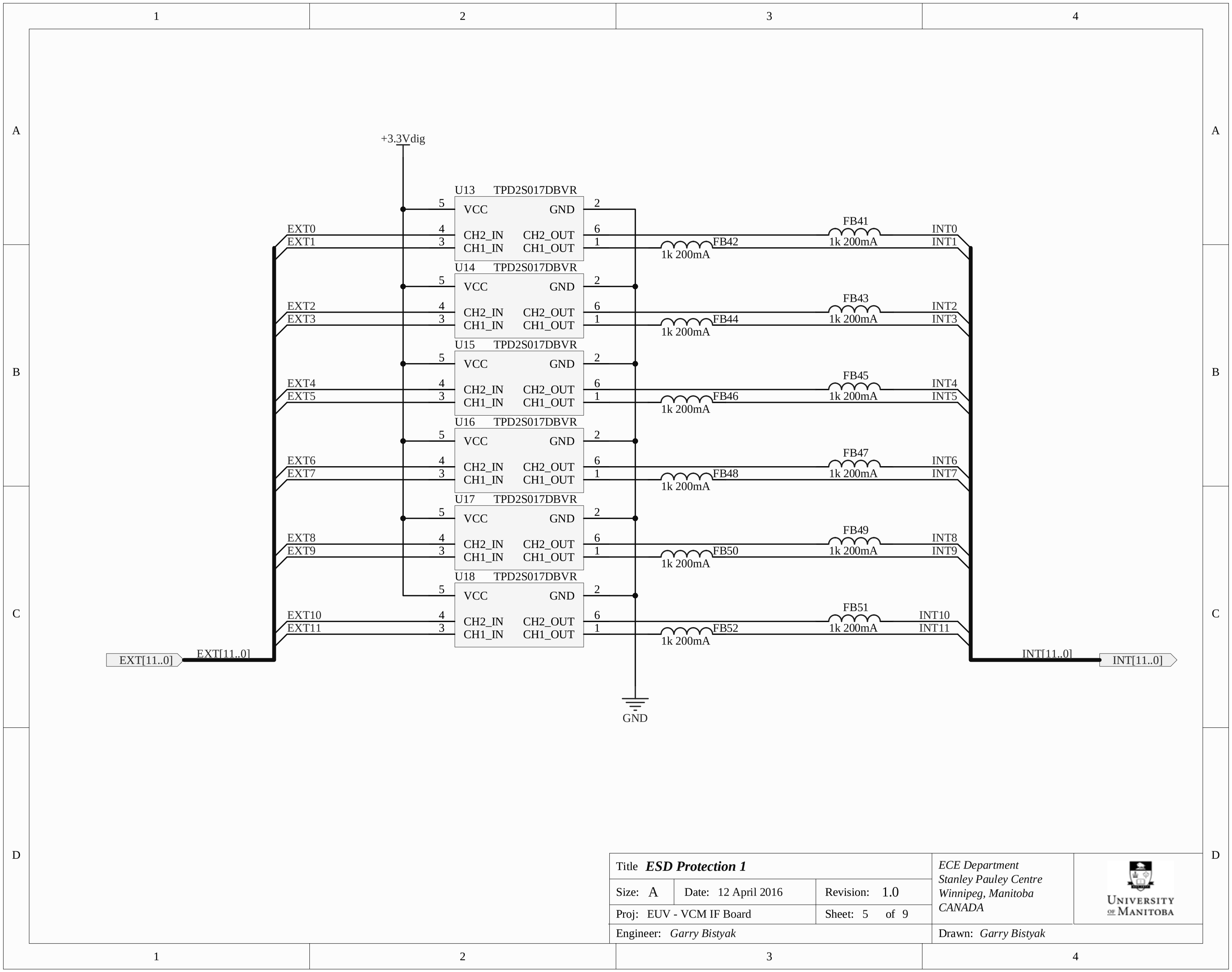

Figure G.5: Interface board schematic ESD protection 1.

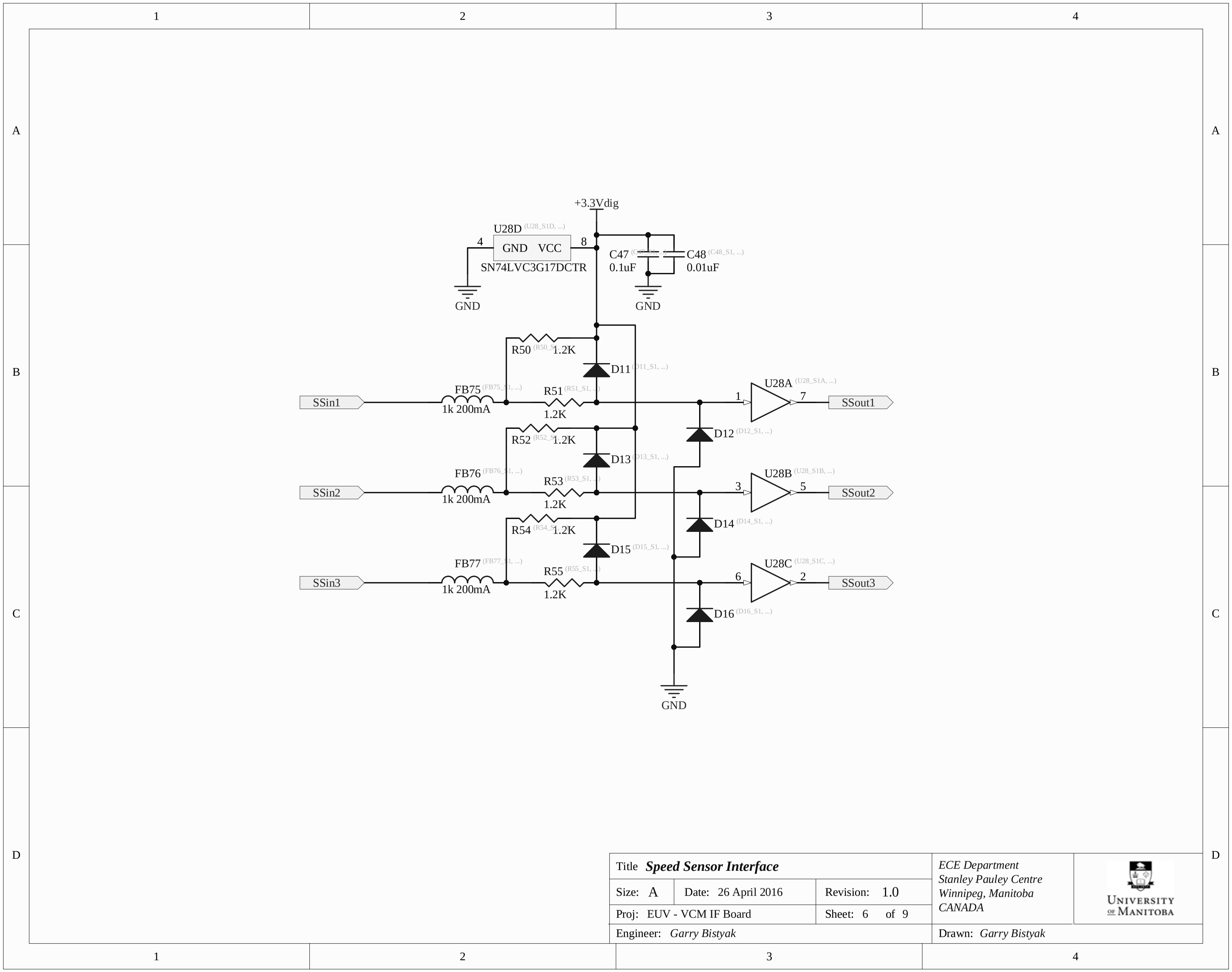

Figure G.6: Interface board schematic speed sensor interface.

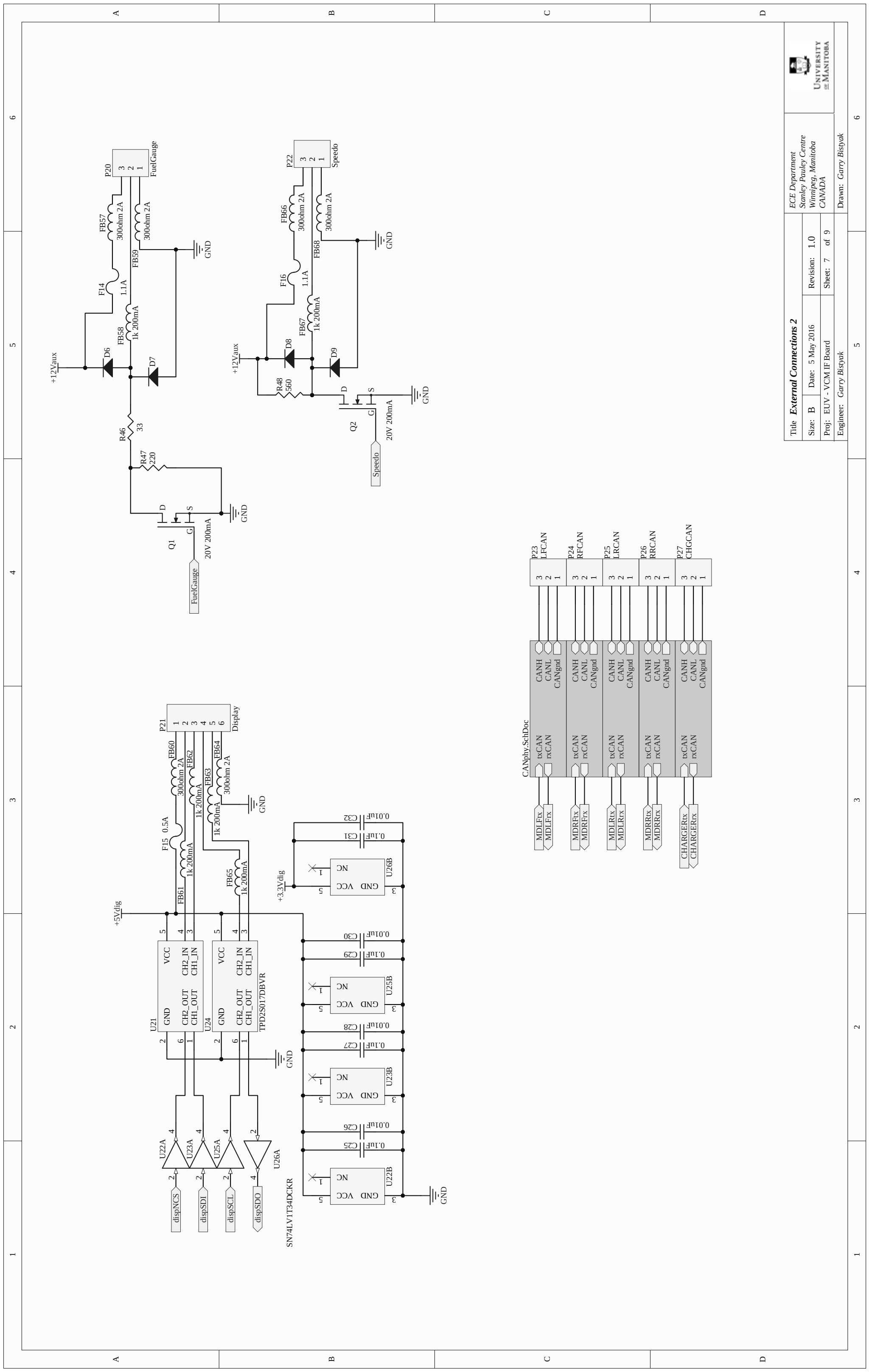

Figure G.7: IF board schematic external connections 2.

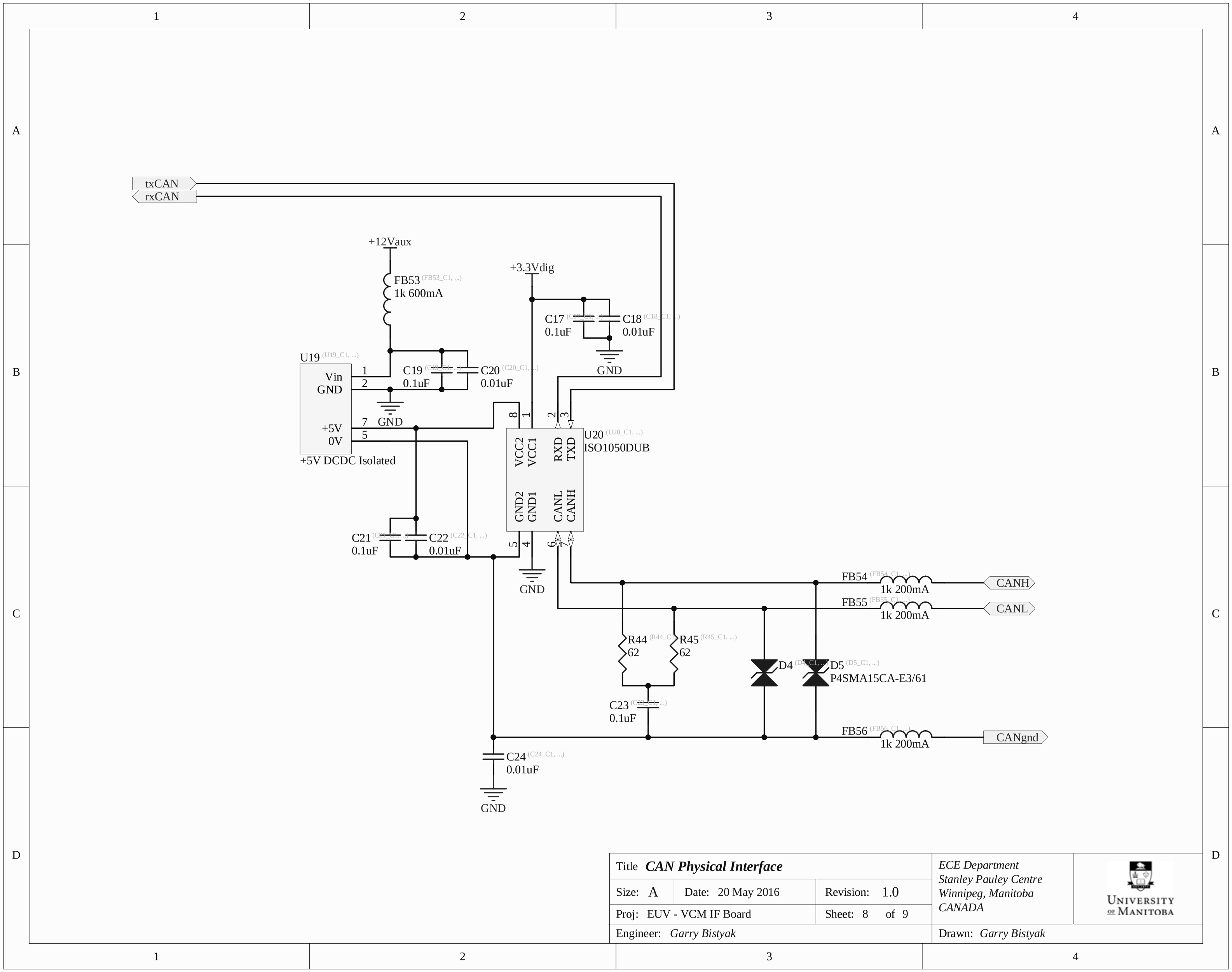

Figure G.8: Interface board schematic CAN physical interface.

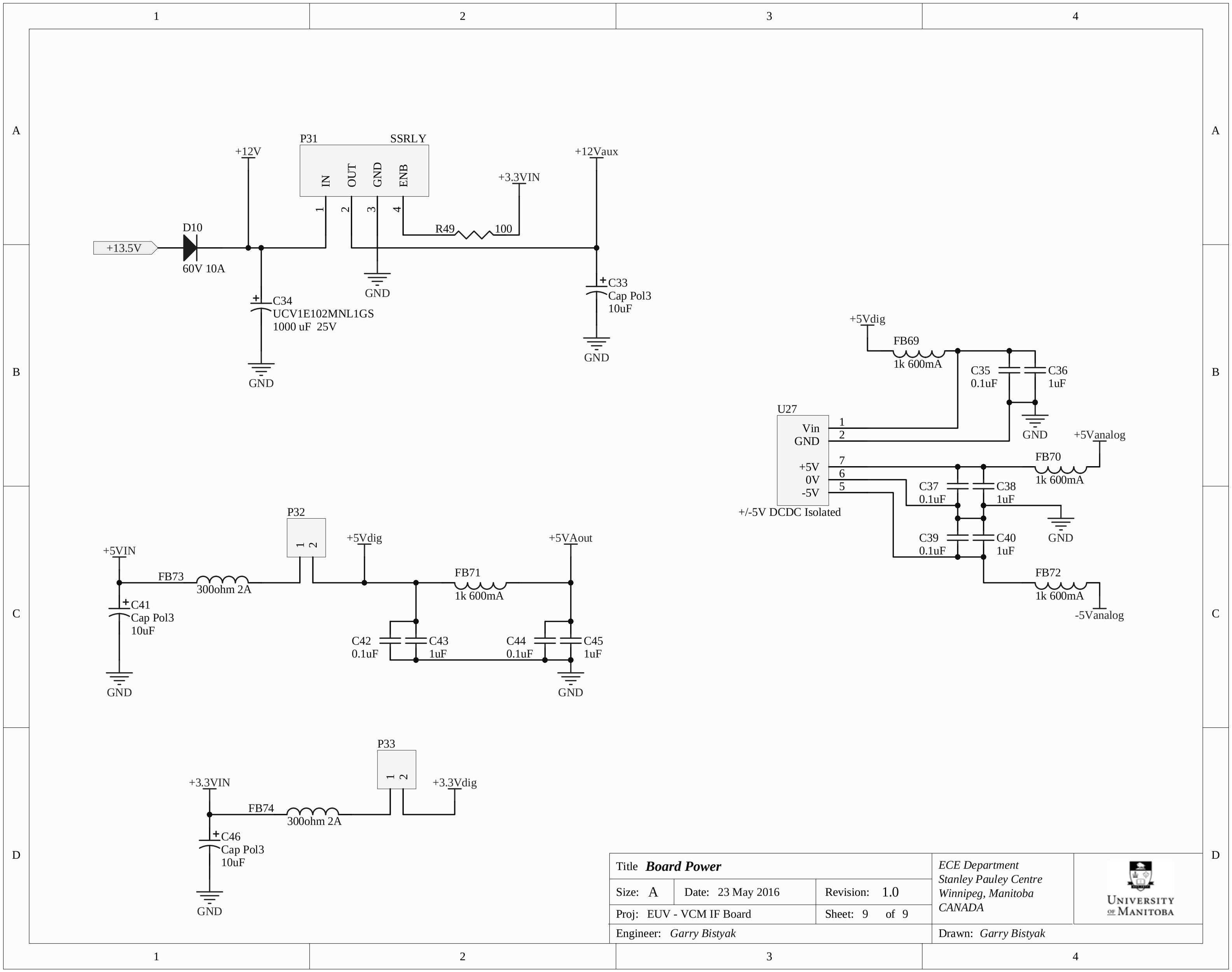

Figure G.9: Interface board schematic board power.

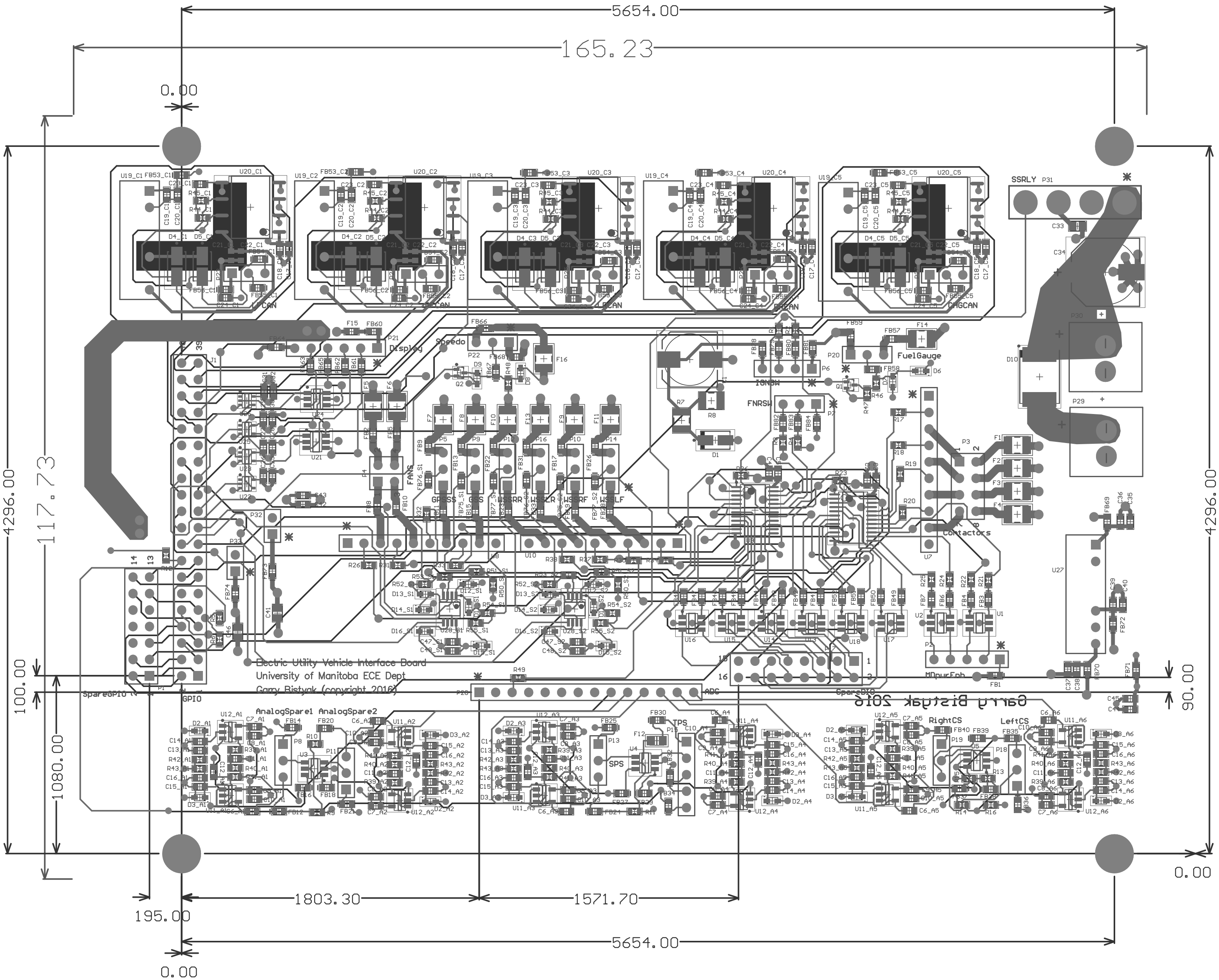

Figure G.10: Interface board PCB layout.

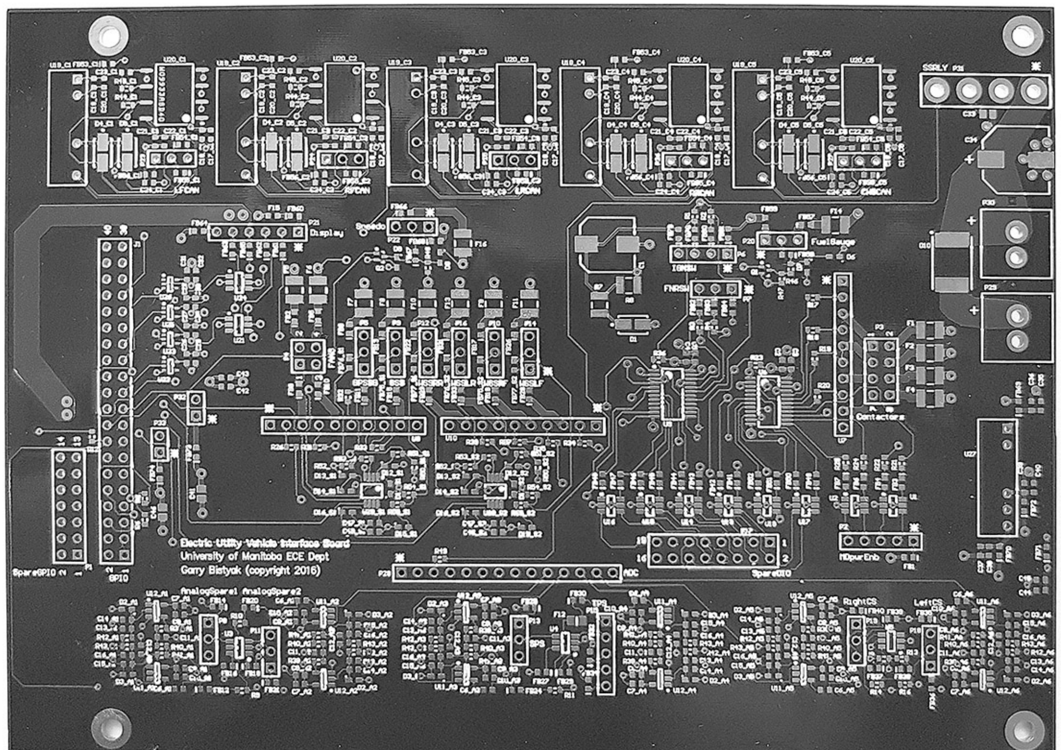

Figure G.11: Interface Board.

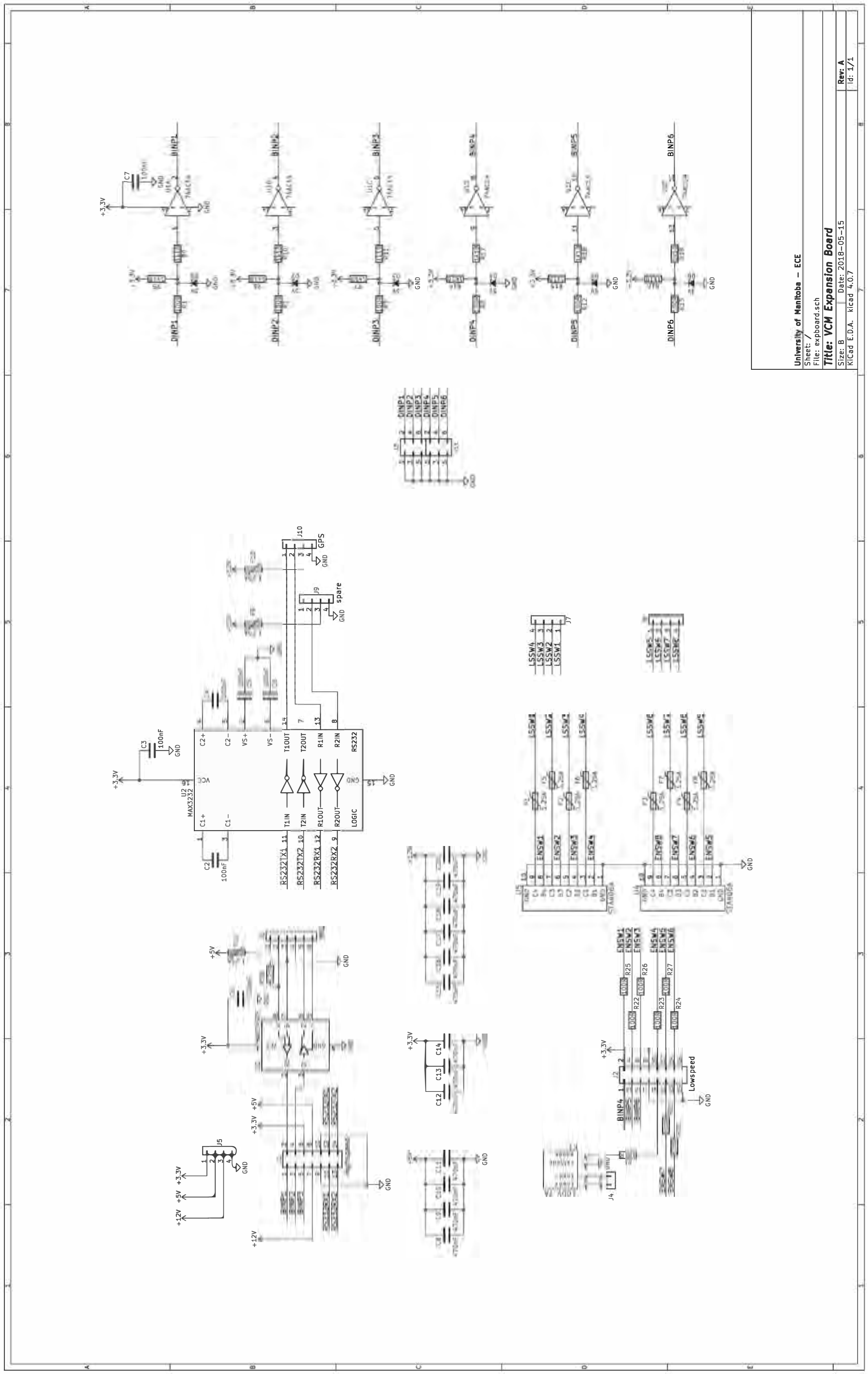

Figure G.12: Expansion board schematic.

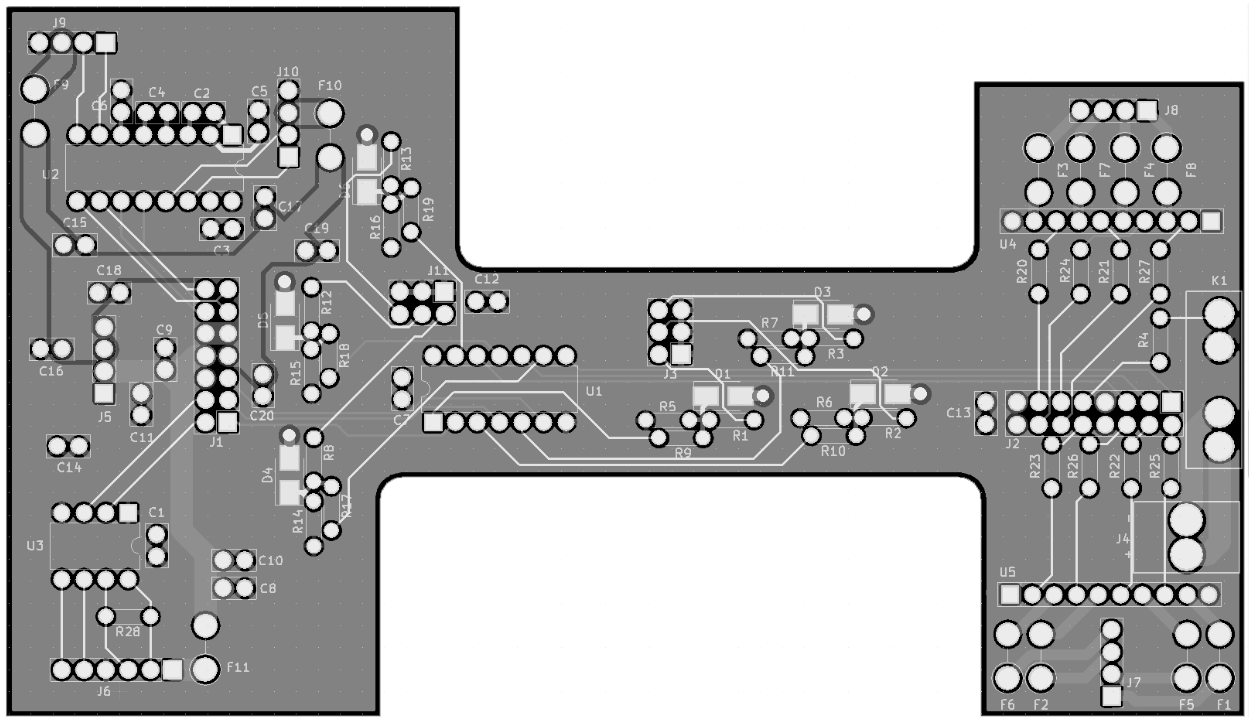

Figure G.13: Expansion board PCB layout.

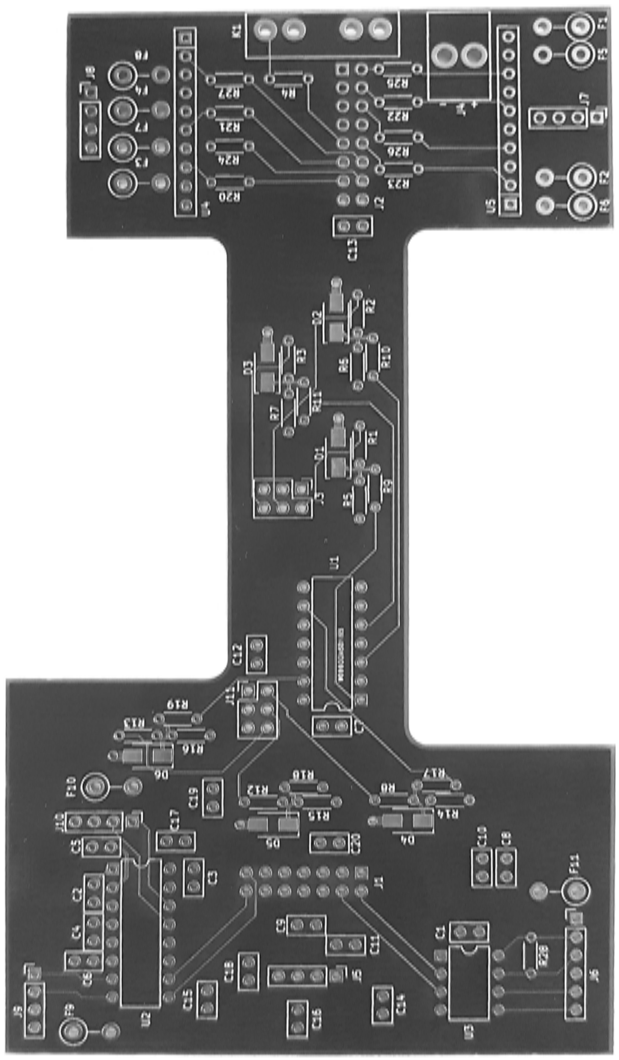

Figure G.14: Expansion Board.

Appendix H

Mechanical Drawings

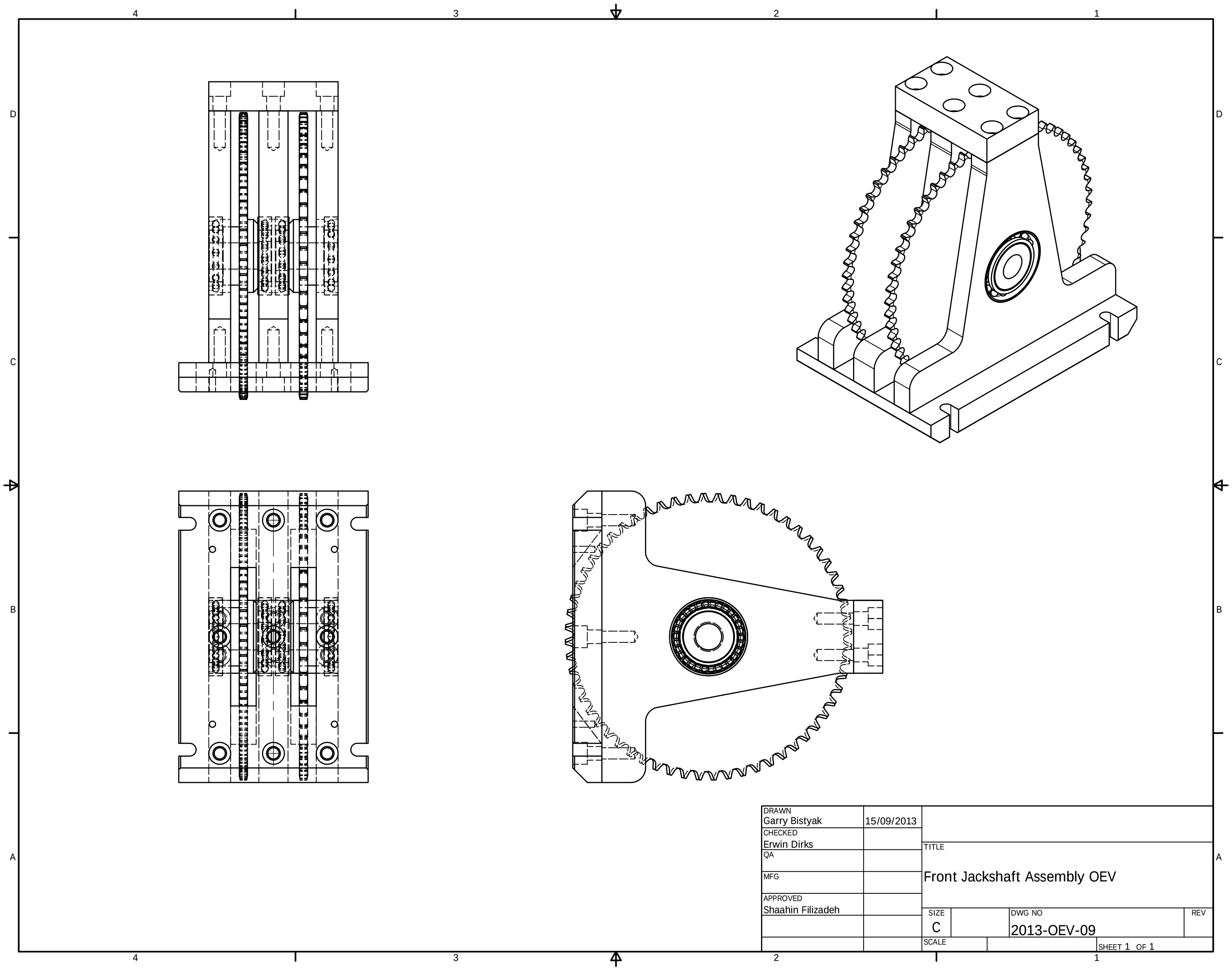

Figure H.1: Front jackshaft assembly.

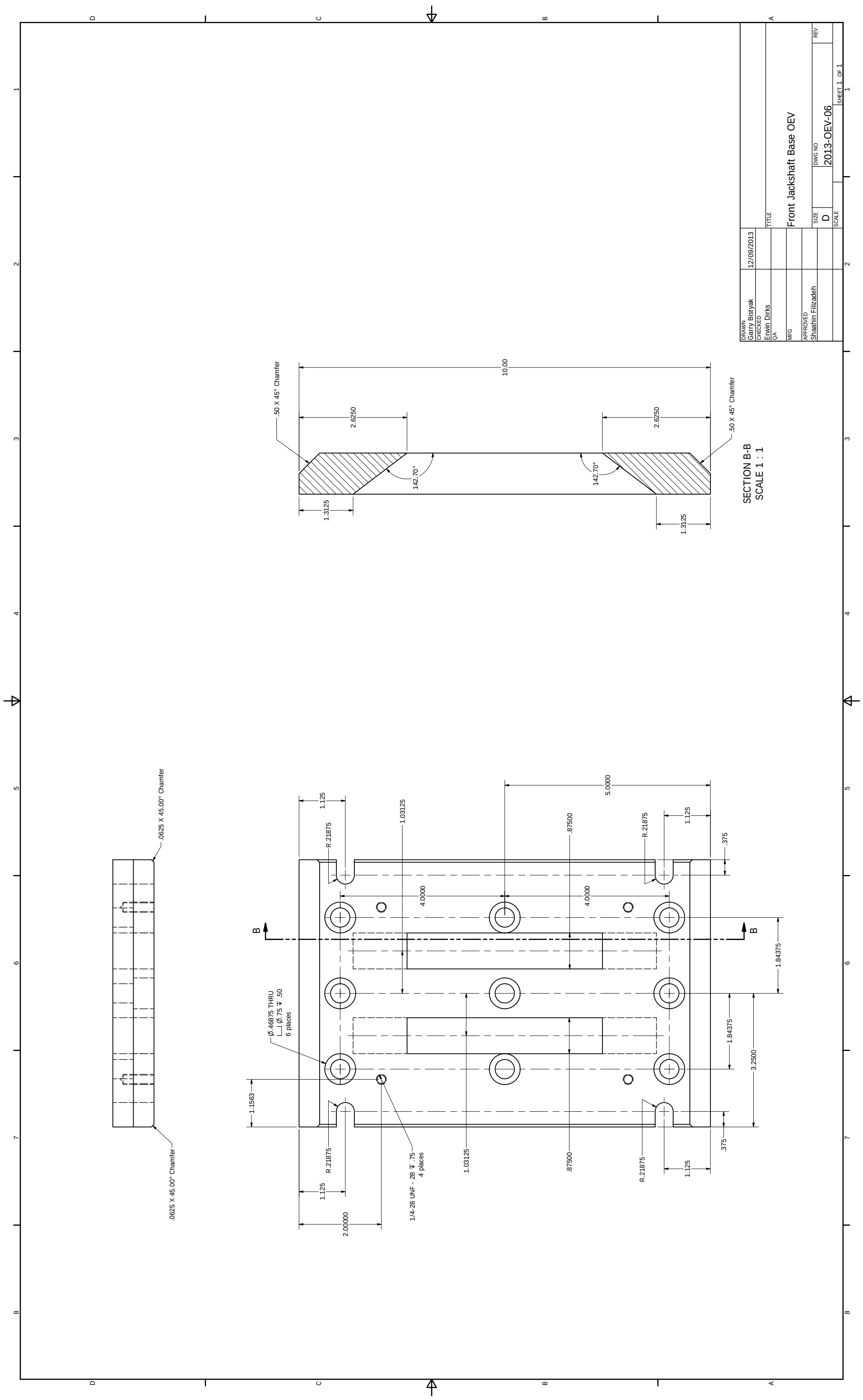

Figure H.2: Front jackshaft assembly base.

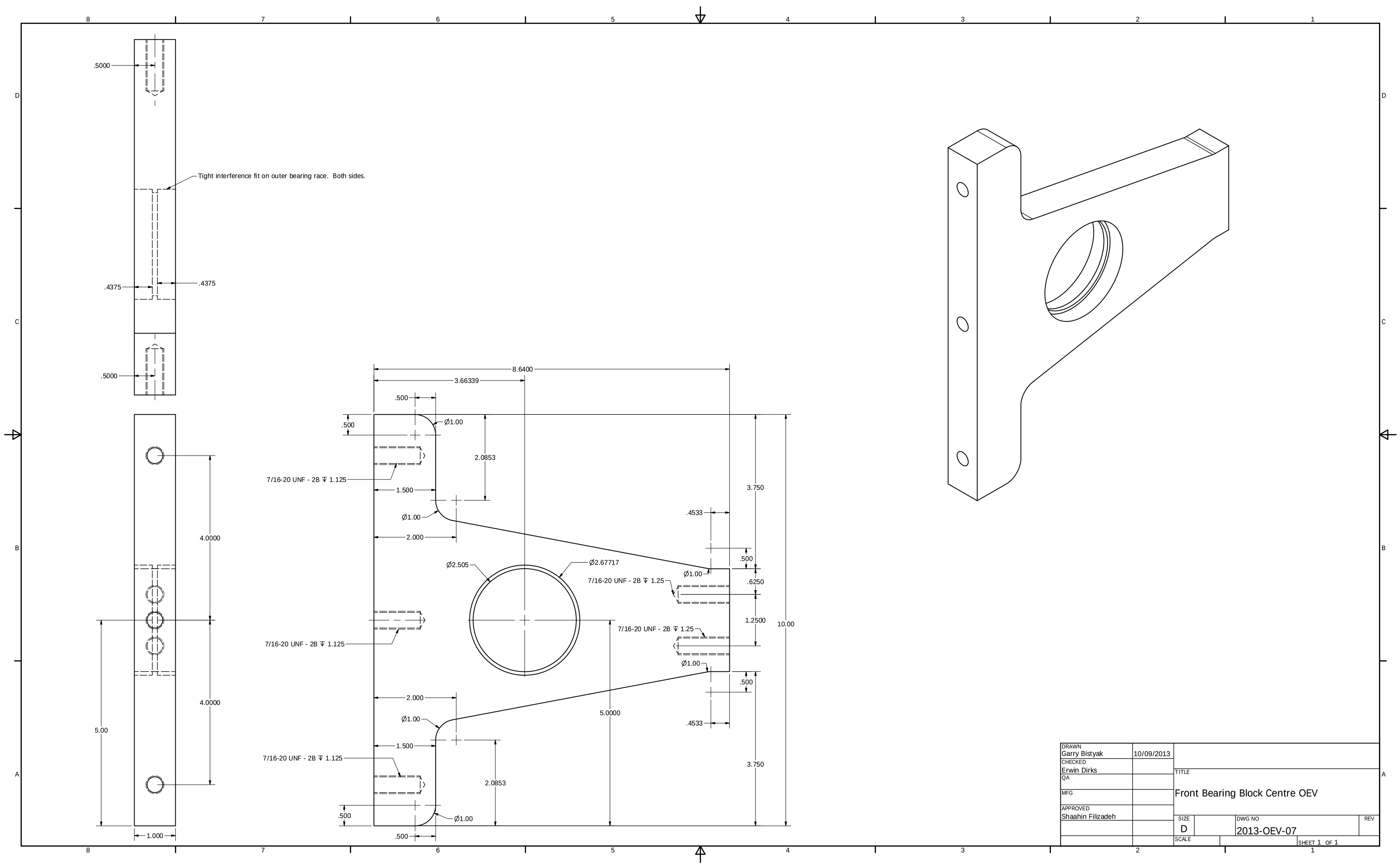

Figure H.3: Front jackshaft assembly bearing block (inner).

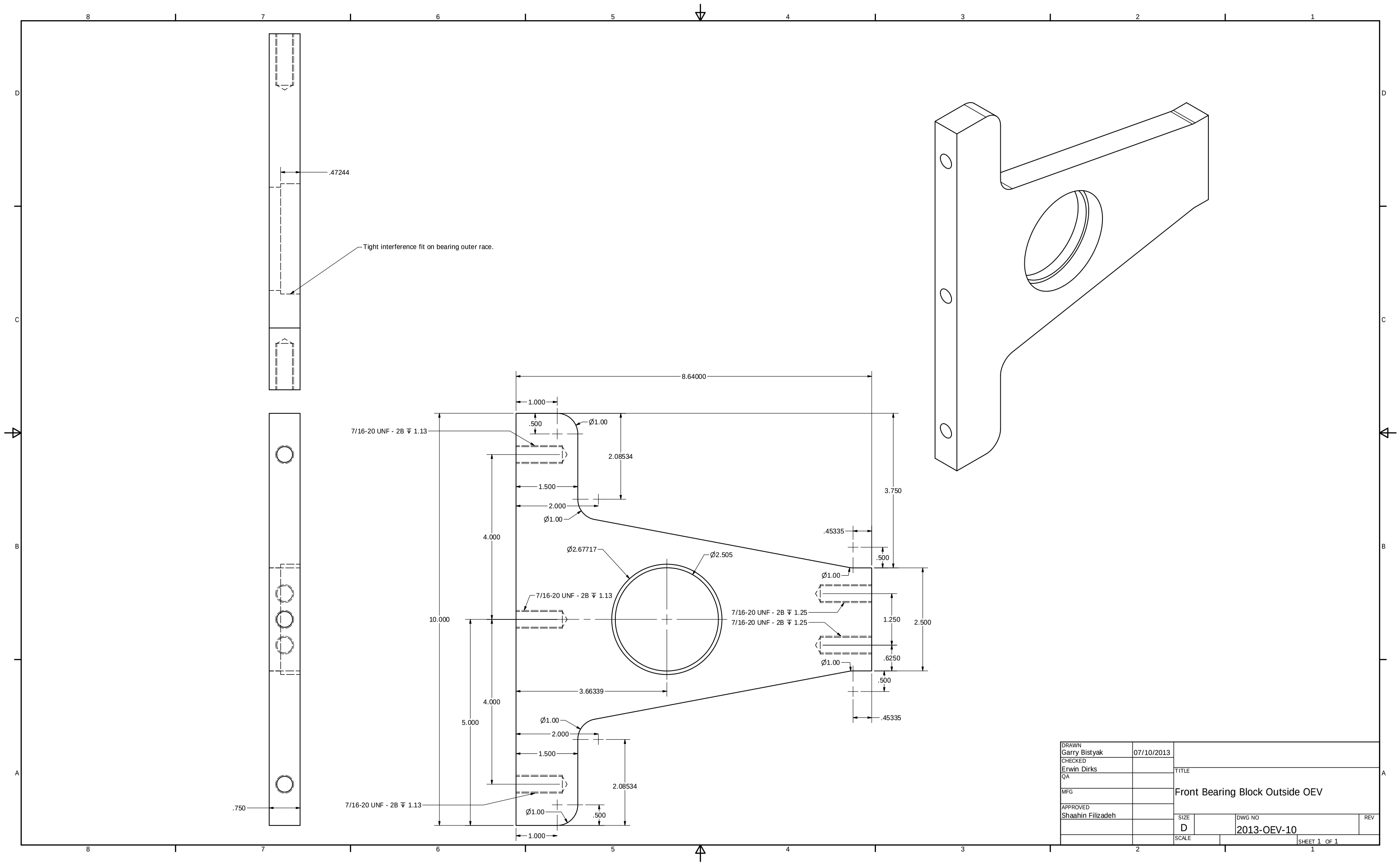

Figure H.4: Front jackshaft assembly bearing block (outer).

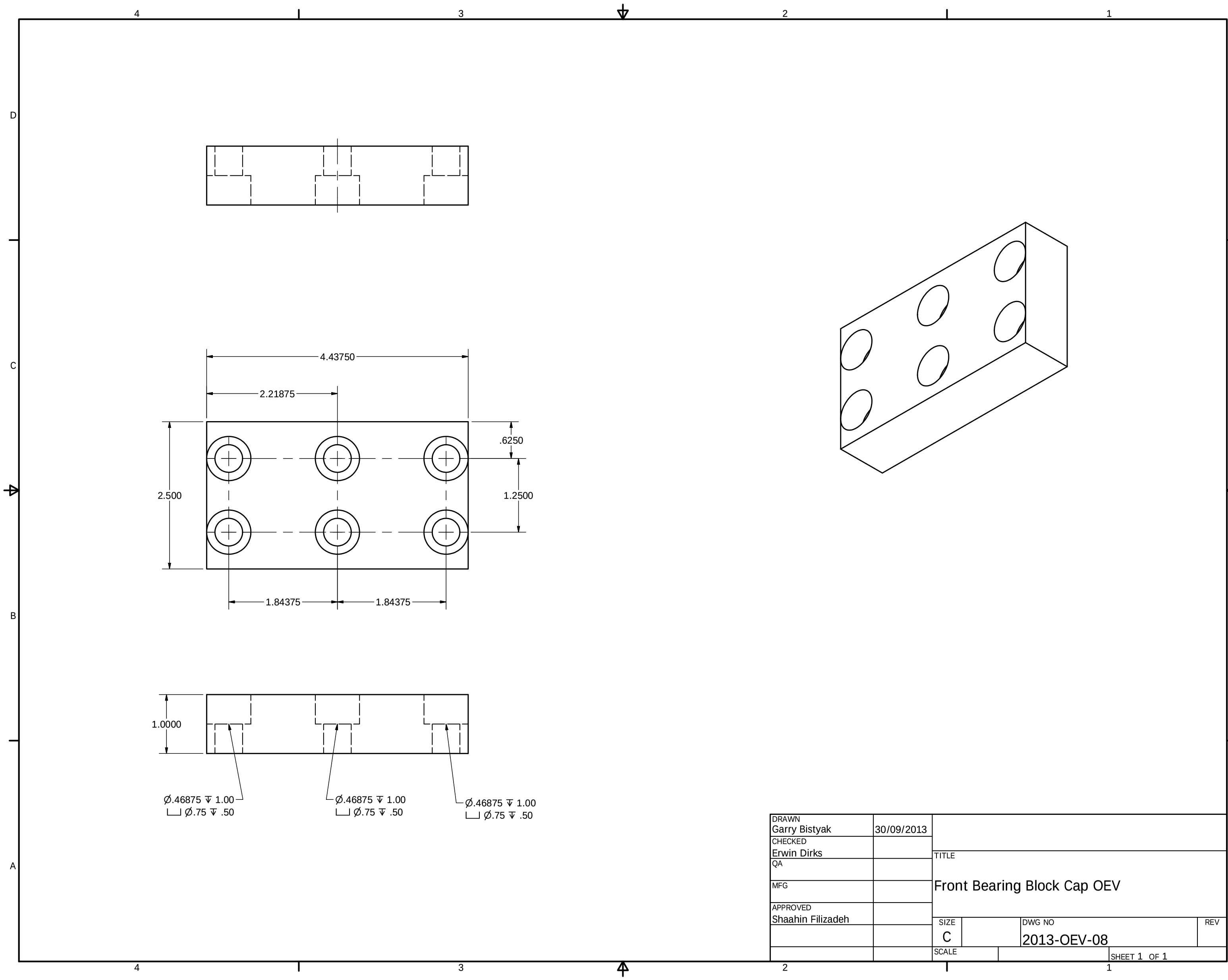

Figure H.5: Front jackshaft assembly cap.

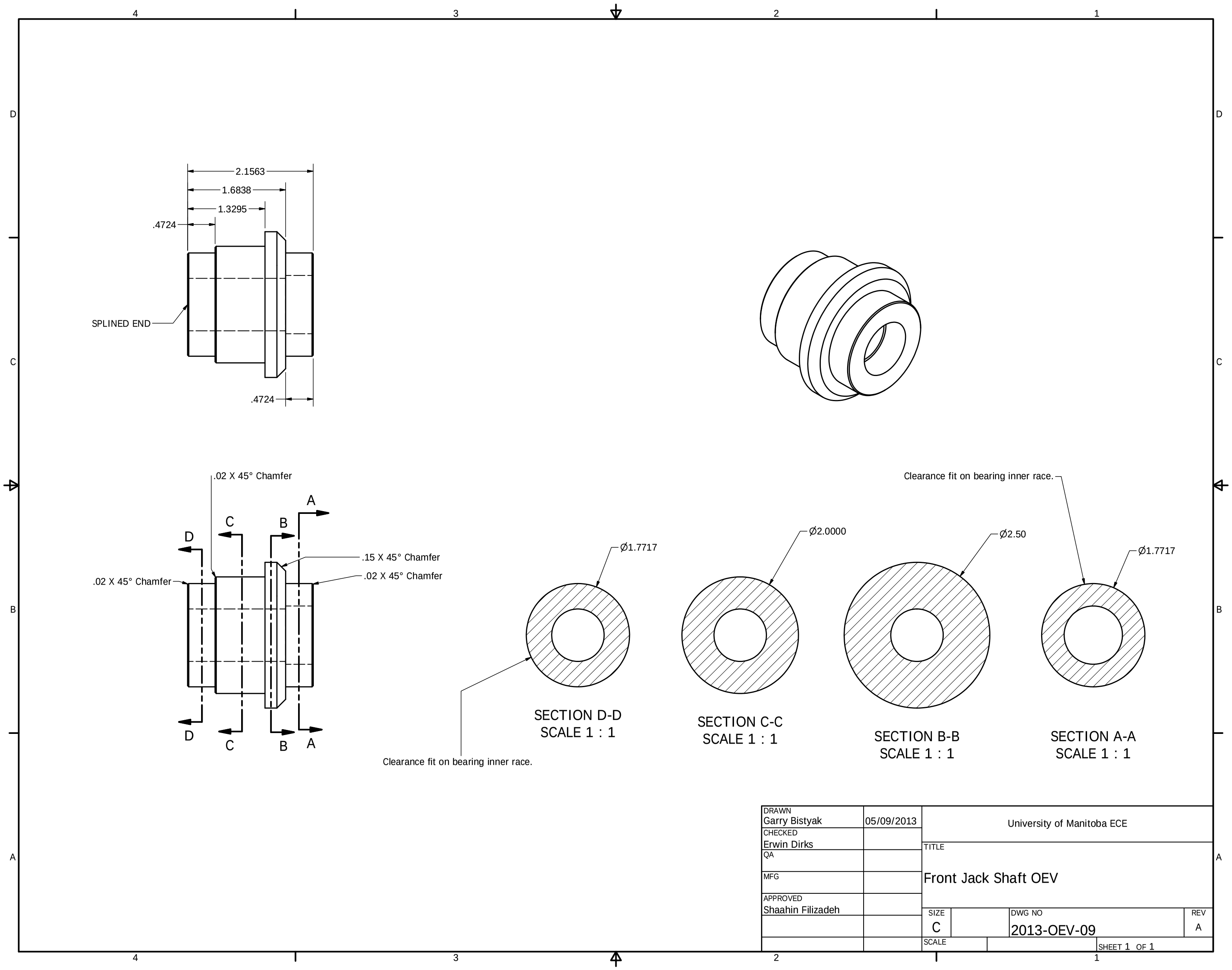

Figure H.6: Front jackshaft assembly jackshaft.

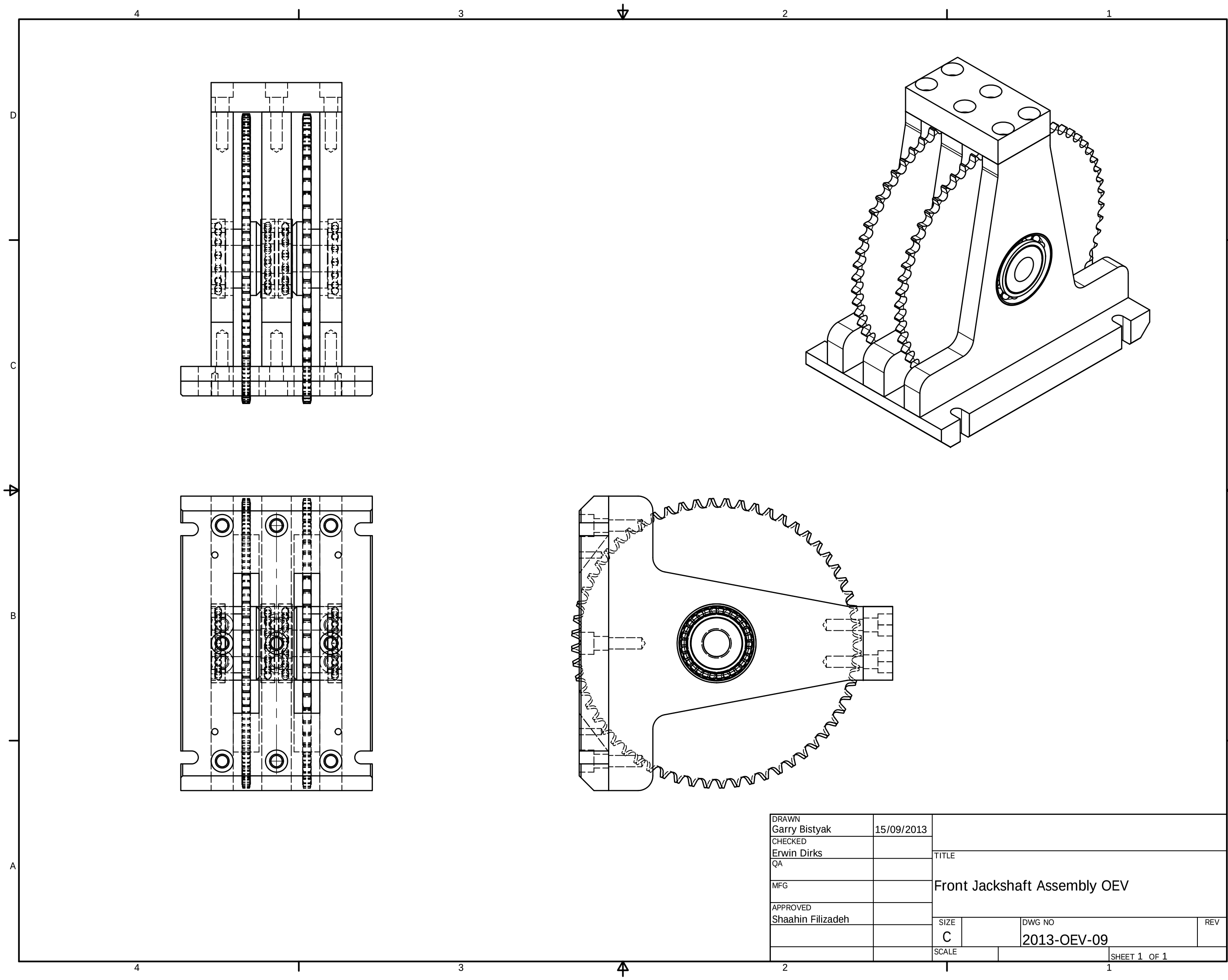

Figure H.7: Rear jackshaft assembly.

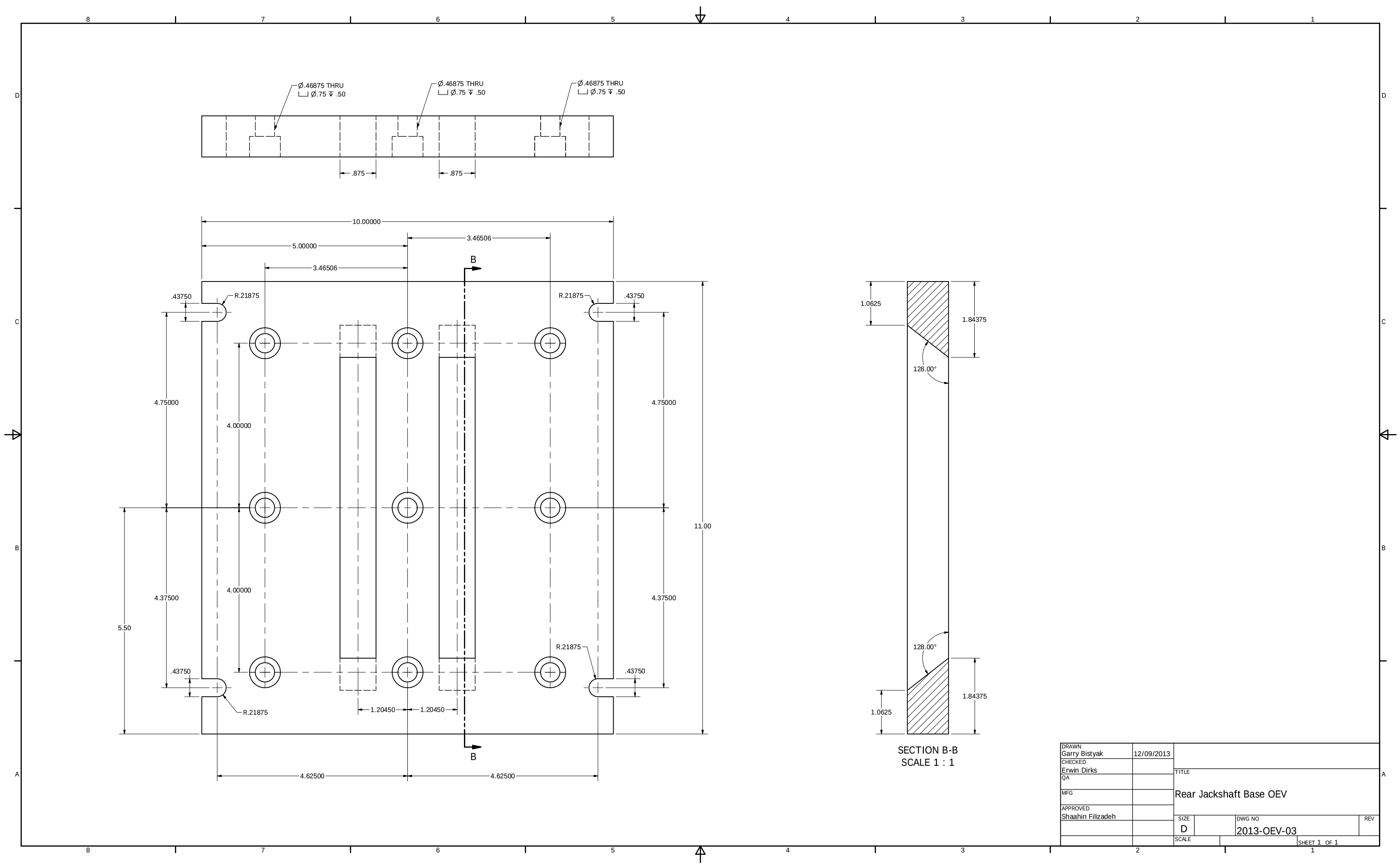

Figure H.8: Rear jackshaft assembly base.

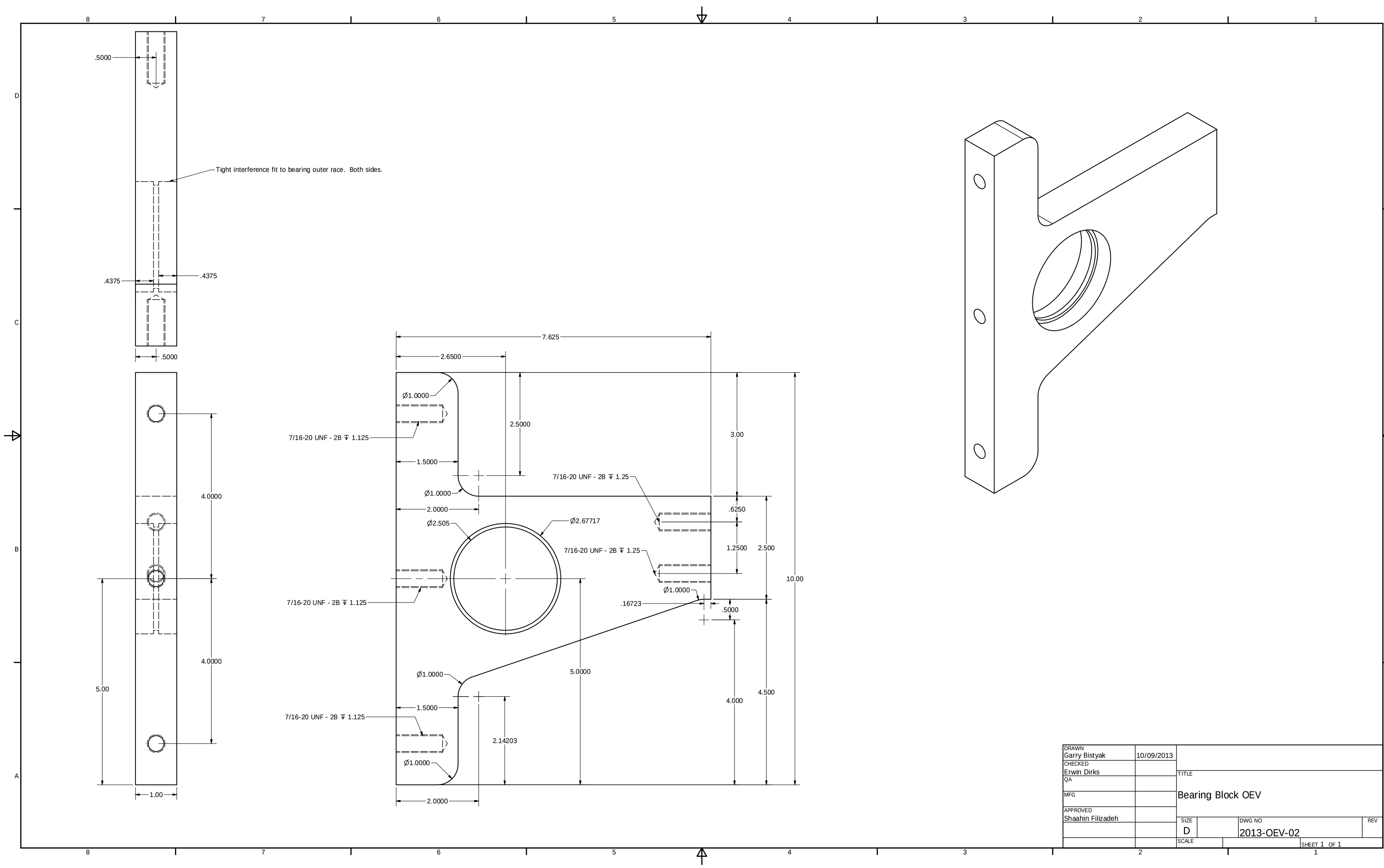

Figure H.9: Rear jackshaft assembly bearing block.

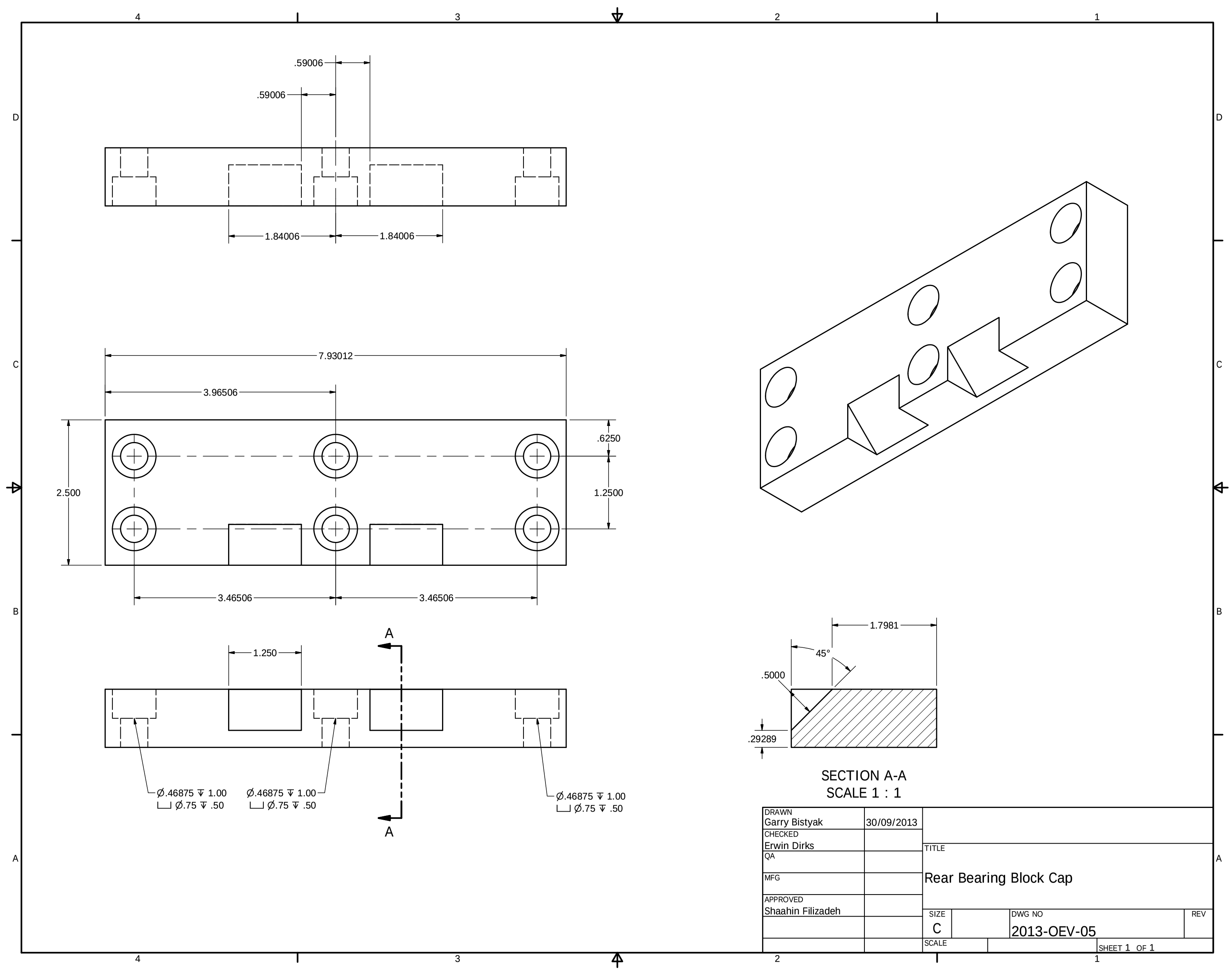

Figure H.10: Rear jackshaft assembly cap.

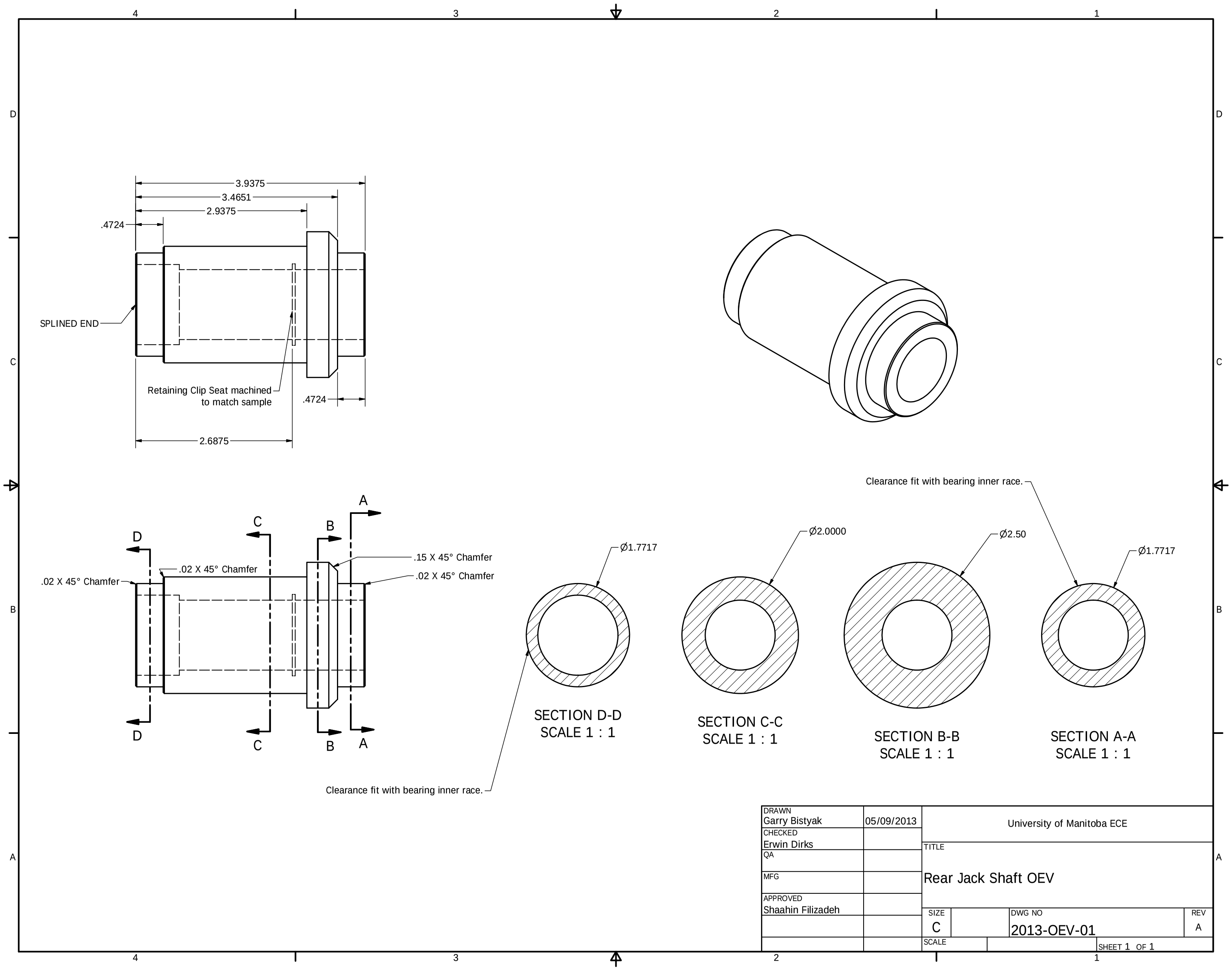

Figure H.11: Rear jackshaft assembly jackshaft.